NASA/CR—2013-215450

Experimental and Analytical Characterization of the Macromechanical Response for Triaxial Braided Composite Materials

Justin D. Littell
University of Akron, Akron, Ohio

December 2013

NASA STI Program . . . in Profile

Since its founding, NASA has been dedicated to the advancement of aeronautics and space science. The NASA Scientific and Technical Information (STI) program plays a key part in helping NASA maintain this important role.

The NASA STI Program operates under the auspices of the Agency Chief Information Officer. It collects, organizes, provides for archiving, and disseminates NASA's STI. The NASA STI program provides access to the NASA Aeronautics and Space Database and its public interface, the NASA Technical Reports Server, thus providing one of the largest collections of aeronautical and space science STI in the world. Results are published in both non-NASA channels and by NASA in the NASA STI Report Series, which includes the following report types:

- TECHNICAL PUBLICATION. Reports of completed research or a major significant phase of research that present the results of NASA programs and include extensive data or theoretical analysis. Includes compilations of significant scientific and technical data and information deemed to be of continuing reference value. NASA counterpart of peer-reviewed formal professional papers but has less stringent limitations on manuscript length and extent of graphic presentations.

- TECHNICAL MEMORANDUM. Scientific and technical findings that are preliminary or of specialized interest, e.g., quick release reports, working papers, and bibliographies that contain minimal annotation. Does not contain extensive analysis.

- CONTRACTOR REPORT. Scientific and technical findings by NASA-sponsored contractors and grantees.

- CONFERENCE PUBLICATION. Collected papers from scientific and technical conferences, symposia, seminars, or other meetings sponsored or cosponsored by NASA.

- SPECIAL PUBLICATION. Scientific, technical, or historical information from NASA programs, projects, and missions, often concerned with subjects having substantial public interest.

- TECHNICAL TRANSLATION. English-language translations of foreign scientific and technical material pertinent to NASA's mission.

Specialized services also include creating custom thesauri, building customized databases, organizing and publishing research results.

For more information about the NASA STI program, see the following:

- Access the NASA STI program home page at *http://www.sti.nasa.gov*

- E-mail your question to *help@sti.nasa.gov*

- Fax your question to the NASA STI Information Desk at 443–757–5803

- Phone the NASA STI Information Desk at 443–757–5802

- Write to:
  STI Information Desk
  NASA Center for AeroSpace Information
  7115 Standard Drive
  Hanover, MD 21076–1320

NASA/CR—2013-215450

Experimental and Analytical Characterization of the Macromechanical Response for Triaxial Braided Composite Materials

Justin D. Littell
University of Akron, Akron, Ohio

Prepared under Grant NNX07AK57H

National Aeronautics and
Space Administration

Glenn Research Center
Cleveland, Ohio 44135

December 2013

This report contains preliminary findings, subject to revision as analysis proceeds.

Trade names and trademarks are used in this report for identification only. Their usage does not constitute an official endorsement, either expressed or implied, by the National Aeronautics and Space Administration.

Level of Review: This material has been technically reviewed by expert reviewer(s).

Available from

NASA Center for Aerospace Information
7115 Standard Drive
Hanover, MD 21076–1320

National Technical Information Service
5301 Shawnee Road
Alexandria, VA 22312

Available electronically at http://www.sti.nasa.gov

Contents

Summary 1
1.0 Introduction 1
2.0 Literature Review 3
2.1 Polymer Matrix Material Testing 4
2.2 Composite Material Testing 5
2.2.1 Composite Material Static Testing 5
2.2.2 Composite Material Interface Testing 6
2.3 Composite Modeling Overview 7
2.3.1 Macroscale Composite Modeling Approaches 8
2.3.2 Microscale Constitutive Modeling Approaches 8
2.4 Material Property Selection 9
2.5 Current Research 10
3.0 Investigations Into Composite Constituent Material Response 10
3.1 Experimental Setup 11
3.2 Optical Measurement Use for Data Collection 11
3.3 Specimen Designs 13
3.4 Test Procedure 14
3.5 Results 14
3.5.1 Tensile Results 14
3.5.2 Compression Results 18
3.5.3 Shear Results 21
3.5.4 Cyclic Load-Unload Results 24
3.5.5 Examination of Results 31
3.6 Constituent Testing Summary 33
4.0 Investigations of Triaxial Braided Composite Material Response 33
4.1 Material Background 33
4.2 Specimen Geometries 35
4.3 Test Equipment 37
4.4 Experimental Results 37
4.4.1 Examination of Global Stress-Strain Data 37
4.4.2 Examination of Local Deformations and Failure 47
4.5 Composite Testing Summary 72
5.0 Development of Macromechanical Triaxial Braided Composite Computer Model 72
5.1 Material Background 73
5.2 Composite Microstructure 73
5.3 Triaxial Braided Composite Model Development 75
5.3.1 Development of Braid Geometry 75
5.3.2 Composite Material Property Implementation 76
5.3.3 Development of Material Failure Parameters 81
5.4 Finite-Element Model Implementation for Prediction of Static Tests 86
5.4.1 T700/PR520 Fiber/Resin Material Response 87
5.4.2 T700/E862 Fiber/Resin Material Response 90
5.5 Conclusions 92
6.0 Triaxial Braided Composite Impact Simulations 92
6.1 Background 92
6.1.1 Material Testing 92
6.1.2 LS–DYNA Introduction 92
6.2 Finite-Element Model Development 93

6.3 Simulation Results 94
6.4 Conclusions 98
7.0 Concluding Remarks 99
7.1 Summary of Results 99
7.2 Future Work 100
7.2.1 Constituent Testing 100
7.2.2 Composite Testing 101
7.2.3 Composite Modeling 101
References 102

Experimental and Analytical Characterization of the Macromechanical Response for Triaxial Braided Composite Materials

Justin D. Littell
University of Akron
Akron, Ohio 44304

Summary

Increasingly, carbon composite structures are being used in aerospace applications. Their high-strength, high-stiffness, and low-weight properties make them good candidates for replacing many aerospace structures currently made of aluminum or steel. Recently, many of the aircraft engine manufacturers have developed new commercial jet engines that will use composite fan cases. Instead of using traditional composite layup techniques, these new fan cases will use a triaxially braided pattern, which improves case performance. The impact characteristics of composite materials for jet engine fan case applications have been an important research topic because Federal regulations require that an engine case be able to contain a blade and blade fragments during an engine blade-out event. Once the impact characteristics of these triaxial braided materials become known, computer models can be developed to simulate a jet engine blade-out event, thus reducing cost and time in the development of these composite jet engine cases. The two main problems that have arisen in this area of research are that the properties for these materials have not been fully determined and computationally efficient computer models, which incorporate much of the microscale deformation and failure mechanisms, are not available.

The research reported herein addresses some of the deficiencies present in previous research regarding these triaxial braided composite materials. The current research develops new techniques to accurately quantify the material properties of the triaxial braided composite materials. New test methods are developed for the polymer resin composite constituent and representative composite coupons. These methods expand previous research by using novel specimen designs along with using a noncontact measuring system that is also capable of identifying and quantifying many of the microscale failure mechanisms present in the materials. Finally, using the data gathered, a new hybrid micro-macromechanical computer model is created to simulate the behavior of these composite material systems under static and ballistic impact loading using the test data acquired. The model also quantifies the way in which the fiber/matrix interface affects material response under static and impact loading.

The results show that the test methods are capable of accurately quantifying the polymer resin under a variety of strain rates and temperature for three loading conditions. The resin strength and stiffness data show a clear rate and temperature dependence. The data also show the hydrostatic stress effects and hysteresis, all of which can be used by researchers developing composite constitutive models for the resins. The results for the composite data reveal noticeable differences in strength, failure strain, and stiffness in the different material systems presented. The investigations into the microscale failure mechanisms provide information about the nature of the different material system behaviors. Finally, the developed computer model predicts composite static strength and stiffness to within 10 percent of the gathered test data and also agrees with composite impact data, where available.

1.0 Introduction

Increasingly, carbon composite structures are being used in aerospace applications. Their high-strength, high-stiffness, and low-weight properties make them good candidates for replacing many aerospace structures currently made of aluminum or steel. As reported by Boeing, 50 percent of the new 787 “Dreamliner” commercial wide-body passenger jet consists of composite materials (Ref. 1).

The new 787 is also using General Electric's (GE's) new GENx turbofan engine. Both the blade and the engine case in this new GENx turbofan engine are made of composite materials. Similarly, other jet engine manufacturers such as Williams International, Honeywell Aerospace, and Rolls-Royce, are developing their own composite engine cases. GE's new GENx is a case already in production whereas Williams International's FJ44–3 and Honeywell's HTF7000 are demonstration cases currently in the design and testing stages. However, instead of being made with traditional unidirectional composite layups, these new fan cases are using a two-dimensional, triaxial braided composite architecture.

A major concern for these companies is that the design of a jet engine case has to have the ability to contain a fan blade in the event that an engine blade-out event occurs. Federal Aviation Administration (FAA) Regulation, FAR Part 33 Section 94–Blade Containment and Rotor Unbalance Tests, requires that the engine case contain a fan blade released at full engine operating speed (Ref. 2). In an engine blade-out event, a fan blade becomes dislodged from the engine center hub and strikes the side of the engine case at a high velocity while the engine is at full operating speed. For composite engine cases, there are two main types of designs for containing engine blades, and these cases fall into either the hardwall or softwall category. An engine case with a hardwall design has sufficient wall thickness around the impact areas to allow the structure itself to resist the penetration and absorb the energy from a released blade. An engine case with a softwall design has an outer layer of Kevlar (DuPont) or Zylon (Toyobo Co., Ltd.) wrapped around the engine case in the most critical area of penetration. For softwall containment, the engine case is designed to allow the blade to penetrate the inner structure, which absorbs the majority of the blade energy, but the ultimate containment is accomplished by the outer wrap (Ref. 3). In both designs, engine case materials must provide sufficient impact resistance to prevent penetration by a titanium or composite fan blade operating at speeds in the range of 600 to 1000 ft/s (183 to 305 m/s).

To pass these requirements, engine manufacturers must conduct destructive blade-out tests on operating engines. Because full-scale and subscale testing of aircraft engines during blade-out conditions is expensive and time consuming and because data are difficult to obtain, alternative methods for evaluating case designs are needed. Accurate computer models that simulate an engine blade-out test offer one attractive alternative for examining the dynamics of the system and diagnosing potential failure mechanisms that occur in a full-scale test. For these reasons, computer models can be used as analysis tools to complement testing where necessary. Once accurate models are developed, system parameters, such as blade speed and trajectory, material systems, and engine case geometry, can be changed with relative ease without having to rerun a full-scale test. Although computer models cannot replace full-scale testing, they can serve as tools to identify and mitigate potential problems before they arise in a full-scale test. However, developing accurate computer models for simulation requires understanding the details of the composite material systems in question.

Carbon-fiber-reinforced composites offer weight savings in aircraft design while still maintaining a high strength-to-weight ratio. Material systems currently being examined for use in composite engine cases are two-dimensional triaxial braided carbon-fiber composites, which offer higher impact resistance than traditional unidirectional composite laminates. Because of these characteristics, the triaxial braided carbon-fiber materials are ideal for the hardwall engine case design.

Traditional composite structures have stacked layers of unidirectional fiber lamina s to form the composite laminate. However, in two-dimensional triaxial braided carbon-fiber-composite material systems, each lamina layer consists of two sets of fiber bundles braided at $\pm\Theta°$ angles, which undulate over and under a 0° axial fiber. This alternating pattern of $+\Theta°$, 0°, and $-\Theta°$ fibers provides the distinct braid pattern, and because each lamina layer has all three orientations of fiber bundles, material characteristics such as impact strength and delamination resistance are improved.

In carbon-fiber polymer matrix composites, the carbon-fiber tows provide the stiffness and strength when the composite is loaded longitudinally to the fiber direction, whereas the polymer matrix binds the fibers together and provides much of the strength transverse to the fiber direction. The properties of the polymer matrix material also play a significant role in an impact situation, where the material is mainly loaded out of plane to the direction of the fibers. The mechanical properties of the polymer matrix are also

of interest because the polymer is the major contributor to the strain rate dependency of the composite material.

Furthermore, even for situations in which the different polymers may behave similarly when tested as constituents, the as-fabricated composite materials having different fiber-polymer combinations can still behave differently when under identical static or impact loading conditions. It is because of this discrepancy that the interaction, or interface, between the fibers and polymer matrix is of great significance and interest and must therefore be examined.

Finally, although the testing of the composite constituents is of great interest, computer models accurately simulating the material response under a variety of loading conditions are also needed. As these computer models will ultimately serve as tools to simulate composite material response, they must not only be accurate enough to simulate the as-measured test conditions but must also be robust enough to be predictive in a variety of loading conditions.

Because of the background just presented, the goal of this research is twofold:

(1) To gain a fundamental understanding of the material response and failure mechanisms involved in composite materials commonly used in jet engine cases by developing test methods that can identify the initiation and propagation of factors, such as delaminations and fiber bundle splitting and/or matrix cracking under static loading conditions.
(2) To use the measured two-dimensional, triaxial braided composite properties obtained from testing to create a macromechanical composite computer model capable of accurately simulating composite material response under static loading conditions.

These goals will be accomplished by first developing test techniques to fully define and characterize the polymer resins used as the matrix materials by finding a complete set of material properties for various temperatures and various strain rates needed in polymer constitutive modeling. Then testing will be done to examine the modes of failures, such as delaminations and transverse fiber bundle failures that occur in the composite materials under static loading conditions. These static test techniques will incorporate optical measurement techniques as the main instrument for obtaining material response data. By measuring the factors involved with the initiation and propagation of failure, discussions will be included about the fiber-matrix interface and how it affects the overall composite material response.

Next, a macromechanical finite-element model will be developed to simulate the composite material response. The stiffness, strength, and failure data gathered from the static testing in conjunction with classical composite analytical techniques will be used to create the material model, and the braid geometry will be simulated using a novel through-thickness integration point method. The model will then be implemented in a finite-element code (LS–DYNA) for use in simulations of the static testing.

Finally, preliminary results will be presented to show differences in the impact responses for different material systems. Preliminary results from the impact simulations will confirm that the developed model will predict different impact responses from different material systems. Since very limited composite impact data are available at the time of this writing, material response comparisons between impact tests and simulations will be qualitative in nature.

2.0 Literature Review

This section presents an overview of relevant, current research on the topics proposed in this study. This literature review is intended to give a background to some of the methods currently in use and to present comparisons and extensions as to the applicability of this research. Specifically, test methodologies and some applicable results for the polymer matrix materials will be presented first. Then previous research into the static testing of composite materials will be presented. Afterwards, an overview of the current modeling techniques for composites both from the micromechanical and macromechanical sides will be explored. Finally, a brief discussion on the material property selection commonly used in composite material model implementation will be presented.

2.1 Polymer Matrix Material Testing

In polymer matrix carbon-fiber composites, the carbon fibers are the main mechanisms that give the composite stiffness and strength in the fiber direction. The primary function of the polymer matrix is to give the composite strength in the transverse and shear directions by binding the fibers together when loaded off-axis. Polymers are rate-dependent, nonlinear, viscoelastic materials that respond differently when tested under different loading rates and temperatures (Ref. 4). Since polymers are rate-dependent materials, they account for the main differences in the responses of composite materials when loaded at different rates. Traditional viscoelasticity theories model the material as combinations of springs and dashpots in series, as with the Maxwell model, or in parallel, as with the Kelvin model, or in combinations thereof (Ref. 5). However, because of limitations in the prediction of material response under a variety of different conditions, there has been great interest in adapting closed-form analytical solutions from plasticity theories originally developed to predict metallic material response to accurately predict the response of the polymer under a variety of loading rates and temperatures. Many researchers have attempted to develop closed-form analytical constitutive models that can predict polymer material response. Examples of some of the analytical solutions can be found in Bordonaro (Ref. 6), Goldberg (Ref. 7), and Karim and Hoo Fatt (Ref. 8). These constitutive models use data from tensile, compressive, and shear tests at different strain rates to quantify various internal state variables based on the individual constitutive law being used. As the composite materials will be used in environments where both low and high strain rates along with elevated temperatures (simulating jet engine operation) are present, polymer material properties acquired from strain rates ranging from 10^{-5} to 10^{2} s^{-1} and temperatures ranging from room temperature to 93 °C (200 °F) are needed. Therefore, it is necessary to obtain a complete set of tensile, compressive, and shear properties in a wide range of strain rates and temperatures to fully characterize the material. Thus, it is of great interest when determining material properties of composites to first determine the material properties of the polymer. To do so, a complete set of material response test data is needed.

There are many techniques to test for the material properties of polymers, and standard guidelines exist to give properties needed for modeling or design. For low-strain-rate testing, the American Society for Testing of Materials (ASTM) Standard D638 (Ref. 9) suggests that long dog-bone specimen geometries serve as the basis for finding tensile properties, and ASTM Standard E2207 (Ref. 10) suggests that long thin-walled tubes be used for conducting shear testing on polymers. In both ASTM cases, the specimen deformation is measured by a strain gauge, and the reaction load is obtained from the test machine. With these data, a full stress-strain curve can be obtained. For testing polymer resins at high strain rates (greater than 10^{2} s^{-1}), a split Hopkinson bar (SHB) is commonly used. Details on the SHB technique can be found in Frantz (Ref. 11).

In numerous cases because of material availability, manufacturing ability, or test constraints, many researchers have proposed novel specimen designs to obtain material properties of polymer resins. Gilat, Goldberg, and Roberts (Ref. 12) used very small dog-bone-shaped specimens for tensile tests and short hollow cylinders for shear tests. Specimens were glued onto tabs to permit their insertion into the test machine. However, many of the shear specimens failed prematurely because of imperfect bonding of the specimen to the tabs or at strain gauge bonding locations, whereas many of the tensile specimens failed as a result of stress concentrations arising from the edges in the square gauge section. Bordonaro (Ref. 6) examined Nylon 66 (Alliance Polymers, Inc.), VICTREX PEEK (Victrex), and Ultem PolyEtherImide (PEI) (Boedeker Plastics) and tried to categorize these polymers and develop constitutive equations using the viscoplasticity theory based on overstress. There, novel specimen designs were proposed, and tension, compression, and torsional tests were conducted using MTS biaxial extensometers (MTS Systems Corporation). However, no elevated temperature effects were considered. Liang and Liechti (Ref. 13) proposed rectangular dog-bone specimens for tension and flat plates for compression; however, strain rate and temperature effects were not considered. Behzadi and Jones (Ref. 14) conducted compression tests on small resin cylinders under a variety of strain rates and temperatures, but tensile and shear tests were not done. Kontou (Ref. 15) examined the effects of temperature on tensile properties of epoxy resins using a

laser extensometer. Buckley et al. (Ref. 16) conducted static and high-strain-rate SHB tests for epoxy resins in compression.

Many techniques for testing polymers have been proposed; however, none is fully robust and able to give a complete set of tensile, compressive, and shear properties at different temperatures and at various strain rates ranging from very low (10^{-5} s^{-1}) to very high (10^{2} s^{-1}). The deficiencies that arise from the lack of a complete set of test data must be remedied so that advanced constitutive models (such as the one discussed in Goldberg (Ref. 7)) can be accurate enough for all of the conditions considered.

2.2 Composite Material Testing

The next step in understanding the nature of composite material behavior is to find the properties of the carbon fiber. Having both the properties of the carbon-fiber fabric and polymer matrix, micromechanics-based equations and techniques such as classical laminated plate theory (CLPT) can be used to find the effective properties of the composite structure. However, it is impractical and many times impossible to measure all of the needed properties of the carbon fibers directly, so material properties of the as-made composite are measured instead. Also, by testing composite coupons, insight above and beyond what is observed just by knowing the constituent behavior can be gathered about the response of the constituent materials in an as-fabricated condition. The knowledge gained from testing can provide valuable information about the fiber-matrix interface and the ways in which the interactions between the fiber and matrix affect material response.

2.2.1 Composite Material Static Testing

Generally, when material properties of a full composite material need to be known, standardized tests can be used. ASTM D3039 (Ref. 17) gives specific guidelines on testing unidirectional or balanced composite laminates in tension; ASTM D3410 (Ref. 18) and D6484 (Ref. 19) provide guidelines on conducting compression tests; and ASTM D5379 (Ref. 20) and ASTM D3518 (Ref. 21) give guidelines on measuring shear properties in a composite laminate. ASTM suggests using either bonded strain gauges or extensometers to measure strain and load cells on the test machine to measure force. These standards call for rectangular-shaped specimen geometries and were originally designed and used for unidirectional composites; however, they also include basic specimen geometries for balanced and symmetric laminates. These test methods are primarily designed to give basic material properties, such as overall tensile or compressive strength and an effective Young's modulus, and are widely used in industry (Ref. 22). Since there is a wide variety of composite material systems and a wide range of uses for these composites, there are standardized databases that provide specific guidelines for testing as well as properties for some of the more common carbon-fiber composite material combinations. These databases include Composite Materials Handbook 17 (Ref. 23), NASA's Advanced General Aviation Transport Experiments (AGATE) (Ref. 24), and the FAA's Material Qualification Guidelines (Ref. 25). In these databases, most of the test data have been obtained by ASTM guidelines, or specimen designs similar to ASTM guidelines have been used.

Others have also attempted to further quantify composite material behavior by developing their own test methods or by testing materials not currently in the above-mentioned databases. At NASA Langley Research Center, Masters and others did extensive investigations specific to two-dimensional, triaxial braided composite materials (Refs. 26 to 30). In Reference 29, notched and unnotched tests for two-dimensional braided composites in tension and compression were conducted to obtain basic material properties. In further research, Masters's (Ref. 28) recommendations for standard strain gauge sizes and overall criteria for testing woven composite materials were developed to account for the heterogeneity exhibited in the composite. Also, Moiré interferometry was used to demonstrate that heterogeneity exists in the displacements of the axial and transverse specimen directions (Ref. 28), but no further discussions on this heterogeneity are presented. Instead, it was concluded that the heterogeneity of the composite specimen demands that strain gauges be at least the length of a unit cell in order to neglect the local

effects of fibers or resin pockets. It was also concluded that specimen width makes little difference in material properties as long as the coupon specimen is wider than the unit cell width.

Others have investigated using noncontact measurement techniques as opposed to strain gauges or extensometers to measure the mechanical properties of composite materials. Grediac (Ref. 31) gives an overview of some of the most popular, which include speckle photography, image correlation, geometric Moiré, Moiré interferometry, and electronic speckle pattern interferometry. Of these methods, few have been used to measure the material properties of composite materials. Gliesche (Ref. 32) used image correlation to measure the strength and in-plane shear properties of ±45° woven cloth. Axial and transverse strains were not measured from the full-field strains but rather were averaged over an arbitrary section to smooth out the heterogeneities from the material. However, Gliesche did prove that the averaged strain values agree well with strain gauge measurements. Although stress-strain curves are presented, the authors offered no discussion of the amount of heterogeneity in the composite. Hale (Ref. 33) used Moiré interferometry to examine strains on woven laminate edges and concluded that Moiré interferometry was extremely sensitive to the heterogeneity on the free edge and to fiber misalignment between the layers of lamina. He does mention, though, that Moiré interferometry is a valuable tool for measuring surface strains on the faces of laminates. Fergusson et al. (Ref. 34) used optical measurement techniques to determine strain fields on composite sandwich structures under four-point flexure. Although he determined that these techniques could provide meaningful full-field strain measurements under test, the techniques provided data that gave way to problems with their four-point flexure test of composite sandwich structures. Fergusson's conclusions are important because they demonstrate that optical measurement techniques provide unique data and illustrate potential flaws in test methods that may otherwise go unnoticed.

Because of the unique nature of the braided composite material systems, many of the techniques originally developed for unidirectional composite laminates may not be sufficient for data collection. Thus, a discussion of the merits of these test methods is needed. Also, many previous researchers have used full-field measurement techniques such as optical measurements and Moiré interferometry to examine braided and woven composites; however, no discussions were presented that gave insight into the causes of localized specimen deformations and failures. Furthermore, previous research has not elaborated on potential failure mechanisms that occur in triaxial braided composite materials that lead to heterogeneities in the material response. It is in this area that the results of current research will be presented in an attempt to explain the complex nature of the triaxial braid and the way it affects the material response.

2.2.2 Composite Material Interface Testing

One potential characteristic that may account for differences in the material properties of fabricated composite structures and the material properties of similar constituents is the fiber-matrix interface. An interface in a composite material is a defined area where the fibers and matrix material meet, and its properties depend greatly on the bonding characteristics between the fiber and matrix material. The physical characteristics of the fiber fabrication, fiber surface treatments, matrix fabrication, composite cure time and temperature, and other variables will affect the interface properties. Whereas the goal of this research is not to identify, characterize, or assign a value to a specific interface parameter for a composite material, it is to address the need for an understanding of the way in which the interface affects material response. Since the interface plays an important role in the composite material response, a review of the current techniques to attempt to characterize an interface is presented.

Researchers agree that a fiber-matrix interface is of great importance in composite material response. A great deal of research has been done to define the material properties of the fiber-matrix interface. Test methods have been developed to try to characterize the fiber-matrix interface on a micromechanical level by looking at a single fiber or single tows of fibers. Some of these methods are discussed in detail in Drzal, Herrera-Franco, and Ho (Ref. 35) and include some methods such as fiber pullout, single fiber fragmentation, and microdebond or microindentation techniques. Sometimes a material parameter called interfacial shear strength (ISS) is sought. Although these are novel approaches to quantify an interface

property, they are largely used in either micromechanical composite modeling confined to a single unit cell or ply or in developing composite constitutive equations. Researchers (Refs. 36 and 37) have also sought to correlate the value of ISS determined from these micromechanical tests to failure types in macromechanical coupon testing. For compression testing, it was determined that a low value of the ISS (representing a weak fiber-matrix interface) caused a delamination failure in the composite; medium values of the ISS caused fiber microbuckling; and high values of ISS caused fiber compressive failure. In axial composite coupon testing, the ISS did not affect the composite strength or stiffness dramatically, but rather affected the mode of composite failure. Composites with a weak ISS demonstrated a progressive failure mode; those with an intermediate ISS demonstrated fiber "brushing" or "brooming"; and those with a strong ISS demonstrated a brittle or abrupt failure. In transverse coupon testing, the stiffness of the composite was largely unaffected by the value of the ISS, but the strength and strain at failure changed with the approximate ratio of the ISS.

Others have taken a different approach to quantify the fiber-matrix interface. Unlike micromechanical interface testing or simulations, macromechanical interface testing attempts to find and quantify an average interface property based on data from coupons or structural subsections. These tests are done on a macromechanical scale with composite coupons; however, the value of ISS must be obtained by indirect methods. Haselbach and Lauke (Ref. 38) attempted to use acoustic emission to identify fiber breaks, matrix cracking, and fiber-matrix debonding, and Todoroki and Tanaka (Ref. 39) used an electric resistance charge method to identify fiber-matrix debonding. Some researchers (Ref. 40) have also attempted to determine a macromechanical ISS with some micromechanical methods: The microdroplet pullout technique was used to quantify an "interface relevance" parameter, and it was shown that the strength of the interface affects the failure modes of the composite. However, a value gained from the microdroplet test could not be directly used as a parameter in material modeling.

Macromechanical interface testing has not been done largely because common measurement sensors (strain gauges, acoustic emission, and ultrasonic vibration) cannot accurately measure or predict the behavior of a macromechanically heterogeneous composite interface. The results obtained from these methods can sometimes be hard to obtain because interpretation of the data comes from indirect techniques to measure a physical property of the material.

Although there have been numerous novel approaches to micromechanically and macromechanically characterize the fiber-matrix interface, the complete characteristics are still unknown, and the fiber-matrix interface property is a subject in which further research is being conducted. Even though it is not the goal of the current research to quantify an interface parameter in the composite materials tests, discussions are presented regarding the different degrees of interface strength and the way they affect composite material response.

2.3 Composite Modeling Overview

This section discusses the current modeling techniques for composites. The discussion comprises two categories. The first focuses on the constitutive modeling and other macroscale approaches that have been developed to categorize and predict overall composite material response but to neglect (to varying degrees) the microstructural behavior of the composite. These methods use various forms of CLPT as their basis; their approaches tend to account for the composite material response in an overall manner and neglect many of the fine details that are found in the microscale approaches.

The second approach contrasts the first approach because it examines composites in a microscale modeling approach. In this approach, usually a small representative volume element (RVE) or repeating unit cell (RUC) of the composite is typically examined. In this approach, all of the finer details are considered and investigated. In many cases, the individual fibers, matrix, fiber undulation angles, and fiber-matrix interface are all explicitly modeled and examined. The goals of this approach are generally not to predict the overall composite material response but to investigate the micromechanical mechanisms influencing items such as overall composite strength and stiffness in a single RUC in addition to failure mechanisms, such as matrix cracking, fiber failure, and fiber-matrix debonding.

2.3.1 Macroscale Composite Modeling Approaches

Traditional constitutive modeling approaches for composite laminates use as their basis analytical micromechanics equations to obtain ply effective properties and CLPT. Discussions of traditional composite micromechanics methods and CLPT can be found in Christensen (Ref. 41). Many macroscale composite material models included in commercial finite-element codes (ABAQUS, NASTRAN, and LS–DYNA) rely on CLPT.

The composite material models built into these codes use CLPT calculations to build the composite laminate based on entered values for material moduli, Poisson's ratios, and lamina directions and stackup sequence. These material models are then implemented into two-dimensional shell or three-dimensional brick elements.

Although CLPT works well when defining laminate material properties based on stacked layers of unidirectional composite lamina, it cannot be directly used with braided or woven composites because a clear distinction cannot be made for each individual layer. Research has attempted to refine traditional CLPT methods specifically to woven or braided composites, and an overview is given in Tan, Tong, and Steven (Ref. 42). Examples include Raju and Wang (Ref. 43) and Byun (Ref. 44), who have developed CLPT equations specifically for woven composites by including fiber undulation. Others have developed their own methods for predicting elastic constants for the braided composite by including specific aspects of composite geometry. Tanov and Tabiei (Ref. 45) developed a four-cell model for woven composites. They divided the unit cell into a number of subcells and modified CLPT equations for each of the subcells by including the fiber undulations. Byun (Ref. 44) developed an approach to modeling triaxial braided composites by using the braid geometry and rule-of-mixtures approaches to calculate the material properties of the composite. Donadon et al. (Ref. 46) developed a three-dimensional constitutive model based on CLPT for woven laminates, and Huang (Ref. 47) developed a "bridging model" for woven composites based on undulations and composite geometry. Another model developed by Ishikawa and Chou (Ref. 48) called the "mosaic model" simplified woven composites by breaking up a unit cell into squares of unidirectional lamina. In this model, laminate properties were found by assembling the unidirectional lamina by rules developed from CLPT. Others created computer models having the fiber tows modeled as beams. Dano, Gendron, and Picard (Ref. 49) modeled two-dimensional, triaxial braided composite static tensile coupons using beam elements for the carbon fiber and shell elements for the polymer matrix material. Similarly, while conducting many tests on triaxial braided composites, Masters et al. (Ref. 27) developed two finite-element models for composite stiffness. The first of these models was called the "diagonal brick model," which used a brick of resin as the outlining element with bar elements representing the carbon-fiber braid. Pastore and Gowayed (Ref. 50) developed what they called a "fabric geometry model," which also modeled the triaxial braid as rods. There, they simulated the triaxial braided fiber architecture using local transformation matrices to simulate the undulation angles and a "stiffness-averaging" micromechanics approach to develop global material constants from constitutive fiber and resin properties.

In macroscopic modeling approaches, the developed models predicted the overall material response to varying degrees of success. However, most models have been developed to correlate one particular test condition and are usually not extended to predict results under a variety of different test conditions. These macromechanical models also failed to predict the behavior of one single fiber tow or resin pocket or the response of the fiber-matrix interface. This is the area in which microscale composite material modeling plays an important role.

2.3.2 Microscale Constitutive Modeling Approaches

Although the macroscale composite models were good at predicting overall composite behavior, they were deficient in predicting material response from a single fiber tow or resin pocket. The micromechanical finite-element models account for this deficiency.

One main concern for researchers is that traditional CLPT and macromechanical approaches neglect the fiber-matrix interface. With these micromechanical models, many researchers have included a fiber-

matrix interface to more accurately define the composite material response because the interface typically has a strong effect on strength and failure modes in the composite specimen. Subramanian, Reifsnider, and Stinchcomb (Ref. 51) developed a micromechanical model that included an "efficiency" parameter developed from a concentric cylinders model. Using this efficiency parameter showed good correlation between predicted tensile strengths and analysis. However, this model was used for unidirectional composites only. Sun and Pan (Ref. 52) introduced a "bonding layer," which was inserted between layers of fiber and matrix. Both these methods had up to 25 percent error in the transverse direction. Xie et al. (Ref. 53) developed a cohesive zone model to simulate the mode 1 fracture in two-dimensional, triaxial braided composite materials. The cohesive zone model used one-dimensional nonlinear spring elements connected between the fiber and matrix and simulated crack initiation and propagation of cracks under static mode 1 fracture. However, a dense mesh and a large number of elements were needed for the simulation to correlate to test data. Tsai, Patra, and Wetherhold (Ref. 54) modeled a fiber pullout test using contact parameters for cohesive debonding and frictional sliding as the interface.

As the examples in the previous paragraph illustrated, attempts to micromechanically define an interface parameter normally led to a computer model having a large number of elements and were therefore inadequate for use in a macroscopic modeling approach. This discrepancy is where the main problem in simulations lie: many of the microscale models include parameters such as braid geometry and a fiber-matrix interface parameter that tend to improve the material response; however, these models are sufficiently large that they cannot be used on the macroscale level, which includes subcomponents or large structures. In contrast, the macromechanical braided composite models that exist can predict overall structural composite material response, but they cannot produce detailed results because they fail to include the micromechanical details. A macromechanical modeling approach needs a model that will account for the features found in the microscale approaches and also be able to predict macroscale behavior of the triaxial braided composite material response and failure for many composite material systems. The approach must at the same time minimize mesh sizes and computational time.

2.4 Material Property Selection

This section discusses the various ways of incorporating the composite material properties into model development. Even though all of the above-described approaches have merit in modeling braided composite materials, the overall laminate material properties used in these models must be found. Many of these approaches that explicitly model the fiber and matrix also implement the constituent properties directly into the model development. Thus, the constituent properties for the fiber and matrix must be known. This type of material implementation can be categorized as a "bottom-up" approach, where the fiber and matrix material properties are the basic, or bottom, parameters and serve as the building blocks for laminate equation development.

As opposed to the bottom-up approach, researchers have used some of the theories described above and developed different methods for material property incorporation by using as-tested composite material properties. This group of theories can be thought of as a "top-down" approach, which uses full composite laminate material parameters obtained from material testing and develops equations that try to back out, or identify, the material properties for either the basic fiber and matrix constituents or a single ply of lamina. Chen and Kam (Ref. 55) developed a novel way to identify the material properties of angle-ply laminates by first measuring the axial and transverse strains during testing and then using error functions to minimize error when comparing these values with theoretical values. Ng (Ref. 56) also uses the top-down approach to back out unidirectional lamina properties from a stacked laminate.

Both approaches have merits and limitations. When using constituent (fiber and matrix) properties, if a particular material parameter is unavailable, many times the value is assumed or gathered from literature. Although the results of these approaches match experimental data well, they can lead to adjusting an assumed material value to make the results match test data. This method is in contrast to using optimization approaches. Many times, certain types of overall composite material properties cannot be measured, which is the whole justification for using optimization. Usually, there are more variables

than equations, and optimization schemes choose the unknown variables so that the total error from all of the equations is minimized. Even though this approach has a good basis in that it uses actual material test data, the final numbers developed are a combination of the equation development presented and solutions from a numerical solver, which have inherent errors associated with them. They do not find a closed-form solution to the problem.

The next section discusses a model development approach that will use conventional composite analysis methods formulation of the material properties in a macroscale model. This model will be capable of predicting an overall material response that will implement test data without using optimization schemes or assumed values for properties.

2.5 Current Research

Previous research has not identified a solution for the testing of the composite constituent, the polymer resin, under a variety of strain rates and temperatures. Previous research has also not accurately characterized triaxial braided composite material response or offered information about the nature of local deformation and failure mechanisms that affect the composite material response. Test methods developed in this study are capable of capturing the resin matrix constituent properties at a variety of strain rates and temperatures for use in constitutive models. They are also capable of capturing the composite material response and identifying some of the local deformation and failure mechanisms. In addition, unlike previous research, these test methods captured the needed information through direct measurements.

Both the developed test methods for the polymer resin and fabricated composite materials utilized a noncontact digital image correlation technique. The noncontact measurement techniques offered advantages over conventional techniques in that they were able to explore micromechanical failure mechanisms such as transverse fiber failure and delaminations. It will be shown that the developed measurement techniques provide all of the data needed for inclusion into material models used in computer simulations.

The material parameters needed in macromechanical finite-element models were obtained via CLPT and traditional composite micromechanics techniques as the data reduction scheme. Although numerous braided composite micromechanical and macromechanical computer models have been developed, none uses measured full-field braided composite test data as a basis for material property inclusion. The model developed in this research has diminished the gap between micromechanical and macromechanical computer models through a micro-macromechanical hybrid approach. The computer models were used to predict triaxial braided composites under static loading.

Finally, the qualitative results that will be presented show predictions of different impact responses based on different material systems.

3.0 Investigations Into Composite Constituent Material Response

As discussed in Section 2.0, the first step in understanding the nature of the composite material response is to examine the behavior of the polymer resin. Because the rate dependence in a composite material comes mainly from the rate dependence in the polymer resin, the resin data cannot be overlooked when trying to analytically characterize and observe the composite material response. Furthermore, one way of characterizing the polymer material response is by developing polymer resin constitutive models in which the resin response can be quantified in closed-form equations using various internal state variables. However, characterizing this material requires a complete set of tensile, compressive, and shear test data so that effects from the hydrostatic stress are accounted for, and internal parameters in the constitutive models can be identified and quantified. The previous methods described in Section 2.0 were deficient in producing appropriate data needed for the analytical models. Therefore, this issue is addressed by developing a test method to fully characterize a polymer in tension, compression, and shear for strain rates ranging from 10^{-5} to 10^{-1} s^{-1} and temperatures ranging from room temperature to 80 °C (176 °F) for a selected resin, Epon Resin 862 (Momentive Specialty Chemicals, Inc.).

3.1 Experimental Setup

Epon 862 (E862 (Momentive Specialty Chemicals, Inc.)) is a thermoset resin with low viscosity. It recently has been examined as a potential candidate for producing composite fan cases. Also, because of its wide availability, it was an ideal candidate for the development of the test method and data collection techniques.

To characterize the strain rate dependence of the E862 resin, displacement rates of 19×10^{-5} cm/min (7.5×10^{-5} in./min), 19×10^{-3} cm/min (7.5×10^{-3} in./min), and 1.9 cm/min (0.75 in./min)—corresponding to strain rates of 10^{-5}, 10^{-3}, and 10^{-1} s^{-1}, respectively—were used for tension and compression tests, whereas 6.875×10^{-2} deg/min, 6.875 deg/min, and 11.458 deg/s twist rates (corresponding to strain rates of 1.6×10^{-5}, 1.6×10^{-3}, 1.6×10^{-1} s^{-1}) were used for torsion tests. All three tests (tension, compression, and shear) were conducted so that the effects of hydrostatic stresses could be quantified and examined as the strain rate was changed. Engineering stress versus strain was measured for all tests to preserve consistency between the tensile, compressive, and shear results. Stress-strain curves were determined at room temperature (~20), 50, and 80 °C (~68, 122, and 176 °F).

The constitutive modeling approach will also attempt to simulate polymers undergoing unloading. To investigate damage accumulation at various loading stages, load-unload tests also were conducted under tension, compression, and torsion for three strain rates and three temperatures. It was noticed that polymers produce a nonlinear unloading curve, caused by a combination of reversible and irreversible deformation mechanisms (Ref. 57). To account for the differences in nonlinearities in the unloading portion of the material response curve, the specimens were unloaded at three specified points: (1) maximum, or saturation, stress, (2) halfway between the elastic region and the saturation stress, and if there was specimen availability (3) approximately 2 percent strain to confirm an elastic unload. The specified load set points were determined from the previously conducted load-to-failure tests.

Testing was conducted in an MTS 858 tabletop test machine with an MTS computer controller and an MTS 622.20C−01 axial-torsional load cell. All tests were conducted in displacement (stroke) control.

3.2 Optical Measurement Use for Data Collection

For previous studies and data presented in literature, strain data were primarily collected by placing strain gauges on the polymer specimen. The strain gauge, in many cases, caused premature specimen failure, as demonstrated in Reference 12. Therefore, a different approach was used for the data collection. Instead of placing strain gauges on the specimens, a noncontact optical measurement technique was used.

The optical measurement system has advantages over conventional strain gauges in that it does not require the sensor to be physically attached on the surface of the specimen, thus eliminating potential stress or strain concentrations, which typically lead to premature specimen failure. Another advantage is that it can be used on all shapes and sizes of specimen geometries, eliminating constraints usually needed with strain gauges. Finally, unlike conventional strain gauges, the noncontact measurement technique delivers displacements in all three coordinate directions (specimen transverse, x; specimen longitudinal, y; and specimen out-of-plane, z), allowing calculations of components of field strains: axial, transverse, and shear. Also, by directly measuring the axial and transverse strains, a Poisson's ratio was directly measured.

The optical measurement system is a commercially available system produced by GOM (Ref. 58) and consists of two digital cameras connected to a computer having specialized software capable of pattern recognition. The entire procedure for using the system is documented in the users manual (Ref. 59) and is summarized in this section for completeness.

After determining the size of the test object in question, appropriate lenses are chosen and fitted on the cameras. The cameras are then calibrated using the software by taking pictures of specialized calibration blocks in various orientations. The calibration procedure allows the software to correct for minor height and angle differences between the cameras and also corrects any distortions present in the camera lenses. When the calibration procedure is completed, the software displays information about the size of the calibrated volume of space that is available to the user. Figure 3.1 is a schematic of the calibrated volume using the stereocamera setup.

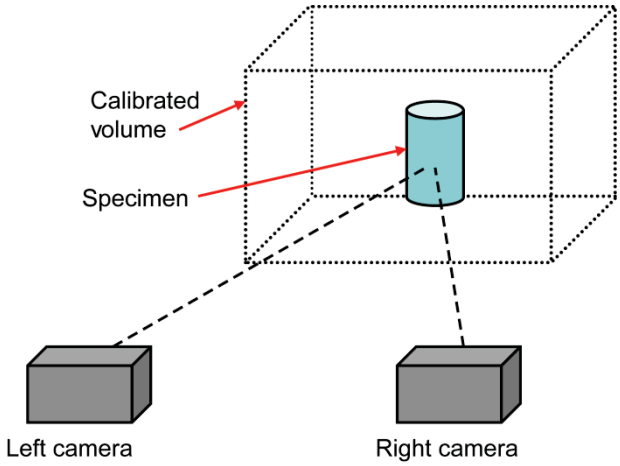

Figure 3.1.—Optical measurement system camera setup.

The user then applies a random black and white stochastic speckle pattern to the test specimen and positions it in the calibrated volume identified by the cameras (noted by the dotted box in Fig. 3.1). The specimen is then loaded and imaged specified intervals during the loading process. Once the test is completed, the user has a time history of stereo-images. These images are used to measure displacements and calculate strains.

During postprocessing, the computer calculates the change in the pattern on the specimen relative to a painted but unloaded reference picture. It then determines the displacements and rotations in the pattern based on the unloaded picture. Strain can then be computed using calculated displacements and reference distances.

When testing specimens at higher temperatures, a specially designed transparent temperature chamber was used. This chamber served as a closed isothermal environment capable of heating specimens up to 176 °C (350 °F) but still allowed the use of the noncontact optical measurement technique. The temperature chamber outer walls were made of a borosilicate glass with a low thermal expansion coefficient. The chamber was heated by connecting it to a laboratory compressed air line containing an inline heater that heated the air before it reached the chamber.

To account for heat losses around the ends of the chamber and near the grips, special resistance heaters were placed near the top and bottom grips. The temperature chamber was calibrated by first setting temperature set points on the chamber controller and placing five thermocouples inside the chamber at various locations. As the temperature chamber ramped to reach the target set points, readings from the thermocouples were plotted and the time for the chamber to reach equilibrium temperature was recorded. When testing specimens in the chamber at high temperatures, the test was started only after the chamber had reached an equilibration temperature.

To account for minor differences in light reflection through the clear thermal chamber glass, the cameras were calibrated through the glass. Calibrating through the glass removed the distortions in the measurements caused by the heating and defects in the glass.

The setup used in the polymer testing consisted of Vosskühler CCD–1330 cameras with 50-mm Schneider C-mount lenses. The calibrated volume for the cameras was approximately 10 by 8 by 8 mm, and the optical measurement system could resolve displacements on the specimen down to approximately 10^{-4} to 10^{-3} mm. The optical measurement system was also capable of capturing the value of the loading from the test machine through an external analog input channel. Thus, by using the synchronized computed strain value and the input load value, stress-strain curves were generated.

3.3 Specimen Designs

Specimens were cut from stock sheets of E862 resin plates that were manufactured and molded to be 0.6096 m (2 ft) tall by 0.6096 m (2 ft) wide by 0.638 cm (0.25 in.) thick using a resin transfer molding (RTM) process. The catalyst used was Epikure W (Hexion Specialty Chemicals) with a cure cycle of 2.5 h at a temperature of 176 °C (350 °F) under 1.03 MPa (150 psi) of pressure. In machining, rectangular bars were cut from the stock panels that were approximately the specimen length. These bars were then machined down to the required 6.0325-cm (2.3750-in.) length and were turned down to a 0.584-cm (0.230-in.) diameter using a CNC (computer numerical controlled) lathe. The gauge section was then cut out on a lathe and finished. The result was a tightly controlled specimen geometry with a very smooth surface finish. This precise machining method allowed for minimal variation between specimens. Tolerances for all specimen dimensions were $\pm 1.3\times10^{-4}$ cm (5.0×10^{-5} in.). The small specimen geometry allowed many specimens to be made from one stock sheet of resin, thereby reducing plate-to-plate variability.

ASTM standard D638 Section 6.3 Rigid Rods (Ref. 9) was consulted for specimen geometry, and the specimens ultimately used in this study kept the similar length-to-width ratios as given in ASTM D638. However, smaller specimen geometries were chosen because it was difficult to make the large resin specimens needed for ASTM D–638 out of the E862 resin because of cracking, bubbling, and warping in the stock plates. These cylindrical specimens had a gauge section 0.3175 cm (0.1250 in.) in length by 0.3175 cm (0.1250 in.) in diameter, a large transition radii, and long 2.54-cm (1-in.) ends used in gripping. These specimens were ideal because they were small enough to manufacture many from the same resin plate, and they could also be used for high-rate SHB testing. ASTM D638 suggests a specimen gauge-length-to-gauge-diameter ratio of 2 or greater to achieve a uniaxial state of stress within the gauge. Although the specimens did not achieve these ratios, the geometry suggested does allow for a uniform state of stress within the gauge, which has been verified by finite-element analysis. A schematic of a tensile specimen is shown in Figure 3.2. Note that the compressive specimens used had the same dimensions as those of the tensile specimens, minimizing machining costs.

For compressive tests, by using the optical measurement system to capture a time history of the loading, the onset of buckling was identified. This information was used to identify the region of stable and usable data.

Shear specimens were designed similarly to the tensile specimens with modifications needed to meet shear specimen requirements. The transition radii were reduced to 0.3175 mm (0.0125 in.) and the gauge section outside diameter was enlarged to 0.5207 cm (0.2050 in.). A hole was drilled in the specimen leaving an inside diameter of 0.3619 cm (0.1425 in.), which gave a wall thickness of 0.762 mm (0.0300 in.). These dimensions ensured that a thin-walled tube assumption could be used during the data reduction. A schematic of the specimen are shown in Figure 3.3(a), and a digital microscopic image of the gage cross section is shown in part (b),which shows a highly uniform thin wall that was achieved by the precise specimen fabrication, an advantage of using CNC machining to create specimens.

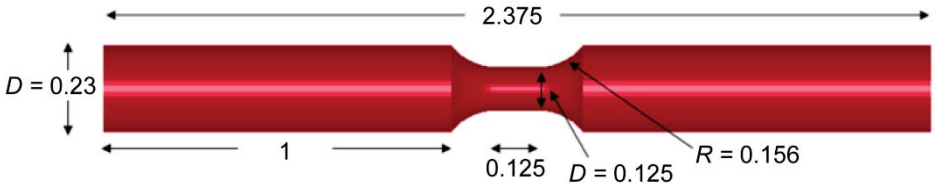

Figure 3.2.—Tensile and compression specimen design, where diameter *D* and radius *R* dimensions are in inches.

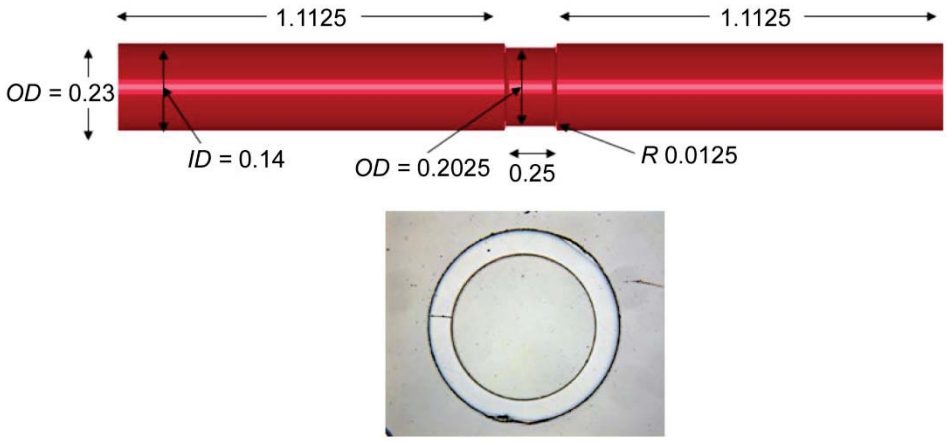

Figure 3.3.—Shear test specimen, where *OD* is outside diameter, *ID* is inside diameter, and *R* is radius. (a) Dimensions are in inches. (b) Gage-section cross section.

3.4 Test Procedure

The specimens were painted with the stochastic pattern and then placed in the test machine and tested by pulling or twisting at the specified rates described in Section 3.1. The optical measurement system collected the test data by taking pictures at specified intervals during the test. Typically, the testing at 10^{-1} s^{-1} lasted approximately 10 s, and the acquisition rate was 10 Hz. The testing at 10^{-3} s^{-1} lasted approximately 20 min, and the acquisition rate was approximately 0.1 Hz. The lowest strain rate testing at 10^{-5} s^{-1} lasted up to 18 h, so data collection was much slower. For these tests, data were taken every 6 to 10 min. The above-described procedure usually gave about 100 to 150 discrete data collections for each of the rates tested. A final postfailure picture was also taken for completeness.

3.5 Results

Sections 3.5.1 to 3.5.4 present the results obtained using the techniques described in Section 3.4. Section 3.5.1 describes the tensile test results; Section 3.5.2, the compression results; Section 3.5.3, the shear results; and Section 3.5.4, the load-unload results.

3.5.1 Tensile Results

Typical tensile results obtained from the optical strain measurement technique are shown in Figures 3.4 and 3.5. Figure 3.4 shows axial strain results from a specimen shortly before specimen failure. One can see the strain uniformity around the perimeter of the specimen and gradual variation of the strain along its length, with the highest strain in the middle of the gauge section, which ensured failure at the midpoint.

Figure 3.4 shows a gauge section midpoint strain of 25 percent, whereas the outer portions of the gauge section had a strain between 15 and 16 percent. Also, Figure 3.4 shows bands of uniform strain wrapping along the perimeter of the specimen. With the knowledge that the bands of strain within the camera field of view extended around the perimeter of the entire specimen, the strain was assumed to be uniform along the entire specimen perimeter based on the uniformity of the data.

Figure 3.5 shows the failure of a tensile specimen with axial strain computed on the bottom portion of the specimen. The failure occurred in the middle of the gauge section, which was desired since the specimens were fabricated to achieve this result. Also note that the optical measurement system computed a permanent plastic deformation of 6.17 percent in the specimen after the failure. Although these data have not been used in constitutive model development, knowing the permanent plastic strain after specimen failure is an advantage of using an optical measurement system.

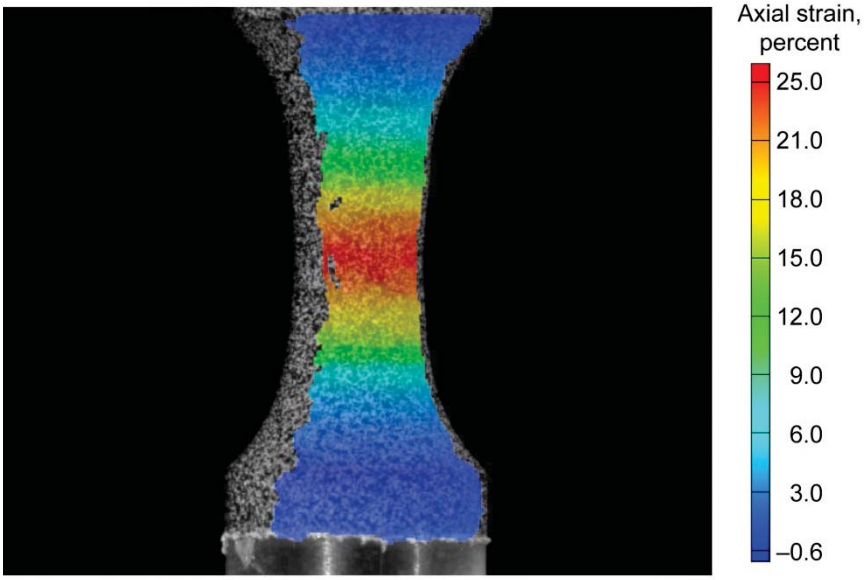

Figure 3.4.—Typical tensile test axial strain results for Epon 862 resin.

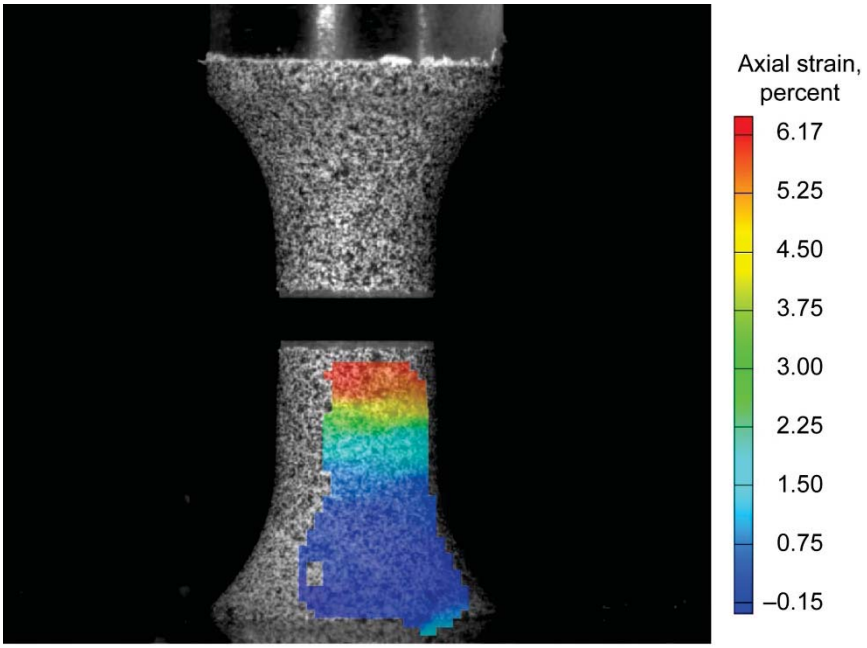

Figure 3.5.—Failure in typical tensile specimen (axial strain shown) for Epon 862 resin.

To plot the stress-strain curves, between seven and nine points were picked in the areas of highest strain in the middle of the specimen gauge section. The strain was averaged for these points. Figure 3.6 shows the points that were averaged for an example tensile test.

In Figure 3.6, note that the nine points averaged for the final stress-strain material response curve for the specimen come from the area of highest strain located in the middle of the gauge section. This method of averaging was used to eradicate any erroneous results due to distortions for a particular location in the dot pattern. Use of the average point data from the areas of highest strain was consistent throughout all conducted tests.

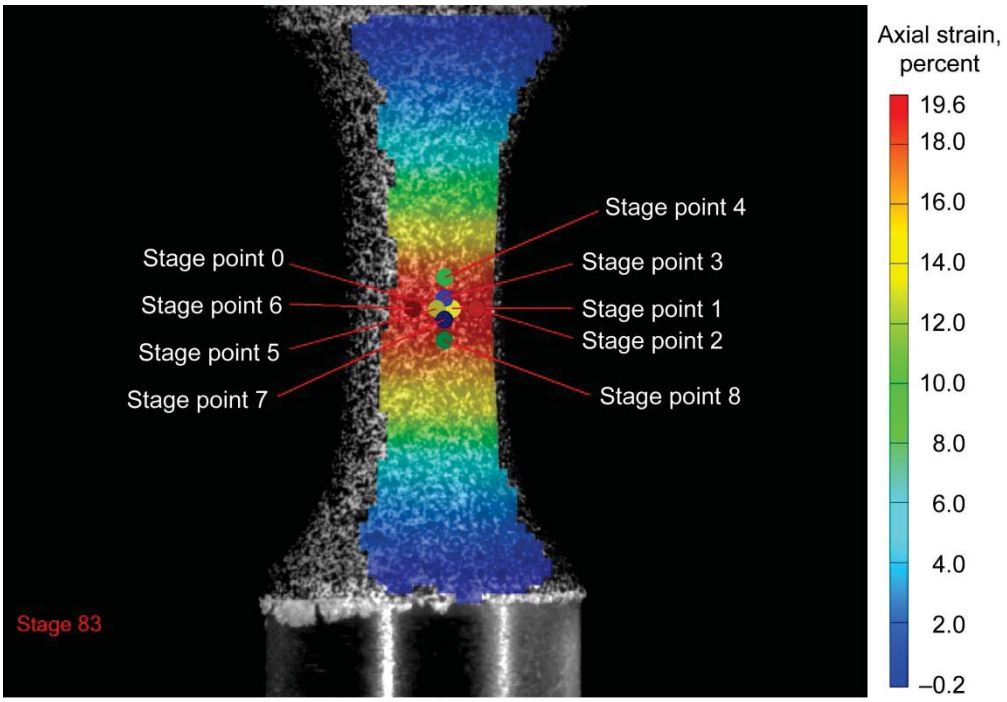

Figure 3.6.—Point map for data averaging for Epon 862 resin. Axial strain is shown.

This same method of point averaging was used for tensile, compressive, and shear testing. Stress was found for the tensile and compressive tests by using the value of the load and dividing it by the original undeformed cross-sectional area, giving the final material response curves in engineering stress. Figures 3.7 to 3.9 show tensile data obtained at the various test conditions. Each curve represents the averaged material response for a single test in each of the figures.

The polymer clearly displayed rate effects, as evidenced by the material response curves for three rates at room temperature shown in Figure 3.7. The highest strain rate tested (10^{-1} s^{-1}) showed an ultimate stress increase of 16 percent over the medium rate (10^{-3} s^{-1}), whereas the difference between the ultimate stresses for the middle strain rate and the lowest strain rate (10^{-5} s^{-1}) tested was 17 percent.

Figure 3.8 shows the temperature dependence of the material at the medium strain rate tested. The polymer exhibited softening at higher temperatures. The lowest temperature tested, room temperature (~20 °C, 68 °F), showed an ultimate stress increase of 28.7 percent over the 50 °C (122 °F) data, and the 50 °C data showed an ultimate stress increase of 26.8 percent over the 80 °C (176 °F) data. Also, the ultimate failure strain showed dependence on temperature. The average ultimate failure strains for room temperature, 50 °C, and 80 °C were 0.3, 0.38, and 0.46, respectively. These results correspond to increases of 26 percent going from room temperature to 50 °C and 21 percent going from 50 to 80 °C.

Figure 3.9 shows the polymer temperature dependence at the highest strain rate (10^{-1} s^{-1}). Again, the polymer exhibited a softening phenomenon at the higher temperatures. The room temperature data showed an 18-percent increase over the 50 °C data, and the 50 °C data showed a 29-percent increase over the 80 °C data. As with the medium-rate temperature-dependence data, the high-rate temperature data showed clear failure strain dependence on temperature. The average failure strains for the room temperature, 50 °C, and 80 °C data were 0.23, 0.36, and 0.47, respectively. These results correspond to changes of 55 percent going from room temperature to 50 °C and 36 percent going from 50 to 80 °C.

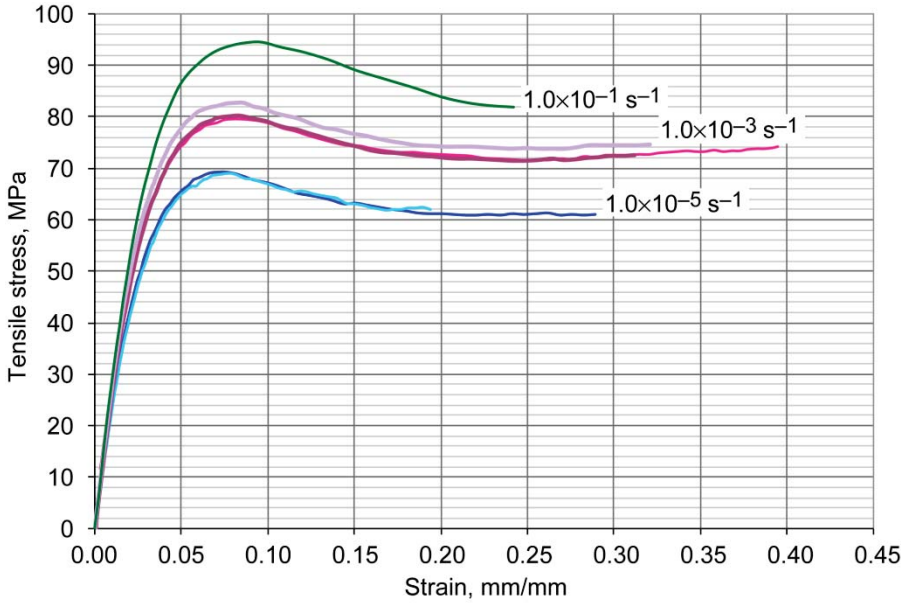

Figure 3.7.—Tensile stress-strain response for E862 resin at room temperature and three strain rates.

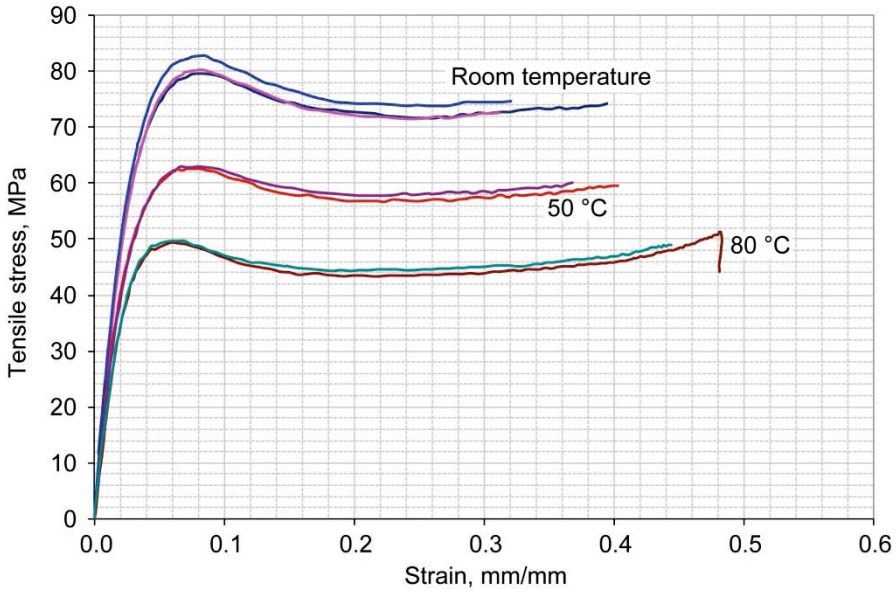

Figure 3.8.—Tensile stress-strain response for E862 resin at 10^{-3} s^{-1} strain rate and three temperatures.

Figures 3.8 and 3.9 show that the temperature played a greater role in the polymer material response than did the strain rate. The data showed the differences in the ultimate stress to be 28.7 percent when going from room temperature to 50 °C (a 150-percent increase in temperature) and 26.8 percent when going from 50 to 80 °C (a 60-percent increase in temperature). In comparison, the data in Figure 3.7 showed that the stress differences were only 16 percent when the strain rate was increased 10 000 percent from the middle to the highest strain rate and were 17 percent when the strain rate was increased another 10 000 percent from the lowest to the middle strain rate.

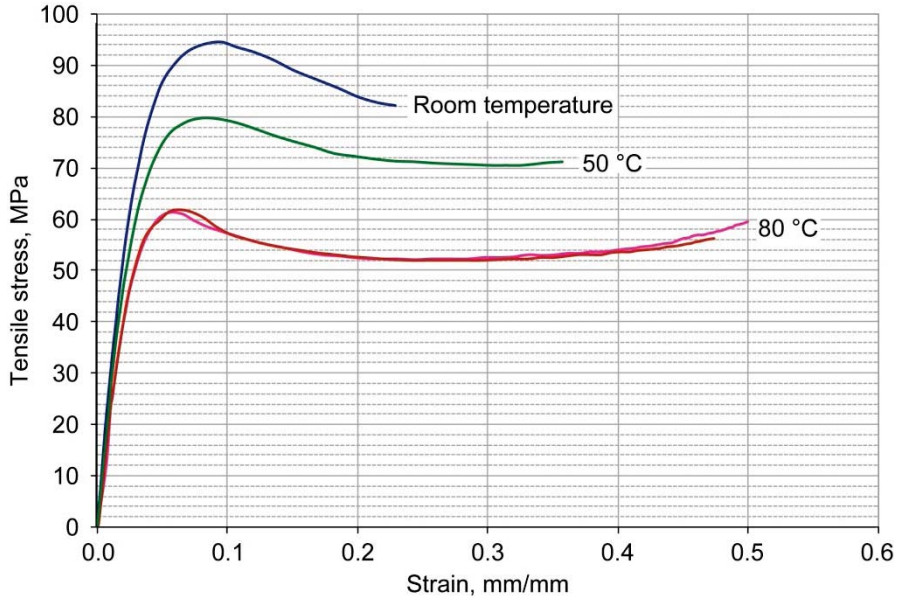

Figure 3.9.—Tensile stress-strain response for E862 resin at 10^{-3} s^{-1} strain rate and three temperatures.

All the curves exhibited the same trends in the material response, whether it was under high-rate, high-temperature loading or low-rate, low-temperature loading. The curves ramped up linearly until an upper yield point was reached. Next, there was a drop in load that caused the material response curves to decrease to a certain saturation stress. During this drop in load, there was localized necking in the gauge section of the specimen. While in the perfectly plastic region, the localized neck propagation spread throughout the gauge section. The material response behaved in the perfectly plastic manner until it started to rise again at the end of the loading, right before failure. The hardening that occurs near the ends of the curves presented in this section corresponds to a sufficient amount of localized polymer molecules aligning in their chain direction, which causes a rise in loading (Ref. 60). The trends in these data also agree with trends found in Reference 6.

Finally, note that multiple overlapping curves in Figures 3.7 to 3.9 show the repeatability of test data attributed to the specimen design and strain measurement system.

3.5.2 Compression Results

The compression specimen geometries used were identical to the tensile specimens. However, material behavior in compression differs from that in tension because the specimens exhibited buckling in compression. Nevertheless, having the optical measurement system allowed the user to capture a test history and observe the strain in the specimen before and during buckling. Typical compression results showed that buckling in the compression specimens began to occur at around 20 percent strain. Although the curves for full stress versus strain until failure are presented in this section, when developing constitutive models, normally the data are only used until the saturation stress. Therefore, the data after buckling were not used in the constitutive models but are presented herein for completeness. Before the onset of buckling, the gauge section of the specimen “fattened” or barreled until approximately 20 percent strain was reached; then, as a result of either geometric eccentricities or slight grip misalignment, the specimen buckled. Figure 3.10 exemplifies a specimen exhibiting a postbuckling response.

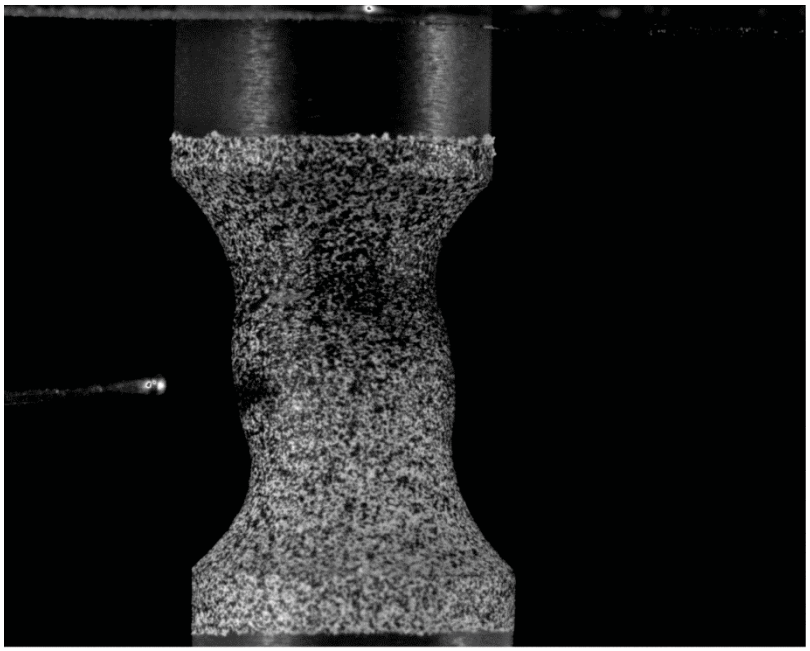

Figure 3.10.—Buckling in typical compression specimen.

However, looking at the stress-strain curves in Figures 3.11 to 3.13, one can see that buckling occurs after the stress plateau is reached, which means that the specimen geometries allow the stress to reach saturation before the onset of buckling. Since engineering stress versus strain is plotted in these figures, the compressive curves tend to rise after the buckling point because the deformed area increases, whereas the original undeformed area of the calculated stress remains constant.

Figure 3.11 shows the rate dependence of the resin under compression loading. Neglecting the rise in the stress-strain curves at strains above 15 percent due to barreling and buckling, the ultimate stresses in the material responses are 93, 106.8, and 126 MPa (13 485, 15 486, and 18 270 psi) for the 10^{-5}, 10^{-3}, and 10^{-1} s^{-1} strain rates, respectively. This result corresponds to a 15-percent increase when going from 10^{-5} to 10^{-3} s^{-1} and to an 18-percent increase when going from 10^{-3} to 10^{-1} s^{-1}. These curves are also 35, 32, and 34 percent higher than the ultimate tensile stress (shown in Fig. 3.7) for the 10^{-5}, 10^{-3}, and 10^{-1} s^{-1} strain rates, respectively. The consistency of the greater ultimate stress in compression with that in tension for the three rates signifies that the hydrostatic stress effects play a role in the specimen response.

Figure 3.12 shows the temperature dependence in the material response in compression for the 10^{-3} s^{-1} strain rate. Again, as with the tensile testing, as the temperature became higher, the ultimate stress for the resin became lower. The ultimate stresses for room temperature, 50 °C, and 80 °C are 106.8, 83, and 60 MPa (15 486, 12 035, and 8700 psi), respectively, corresponding to a decrease of 29 percent when going from room temperature to 50 °C and 34 percent when going from 50 to 80 °C. The values of ultimate strain could not be found because of the buckling phenomena that occurred in the material response; however, the figure shows that the onset of buckling began much earlier in the room temperature specimen than in the higher temperature specimens.

Figure 3.13 shows the temperature dependence in the material response in compression for the 10^{-1} s^{-1} strain rate. The data at the highest strain rate confirmed what was found for the temperature dependence at the lower strain rate (10^{-3} s^{-1}) tested. The ultimate stresses for room temperature, 50 °C, and 80 °C (122 and 176 °F) are 126, 102, and 76 MPa (18 270, 14 790, and 11 020 psi), respectively. The changes in ultimate stress correspond to the changes in ultimate stress in the lower rate tested. The ultimate stress decreases by 24 percent when going from room temperature to 50 °C and decreases by 35 percent when going from 50 to 80 °C. These values are similar to those seen in the lower rate testing: in the lower rate testing, the decrease

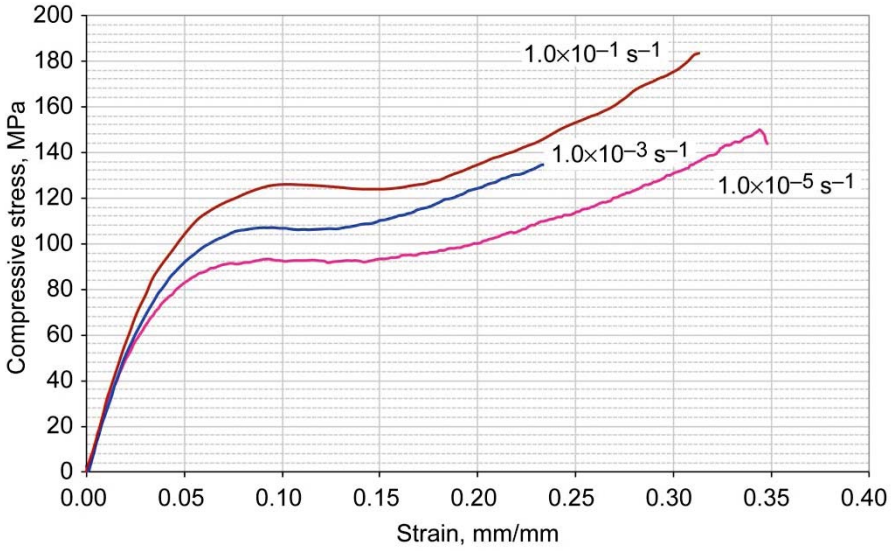

Figure 3.11.—Compressive stress-strain response for E862 resin at room temperature and three strain rates.

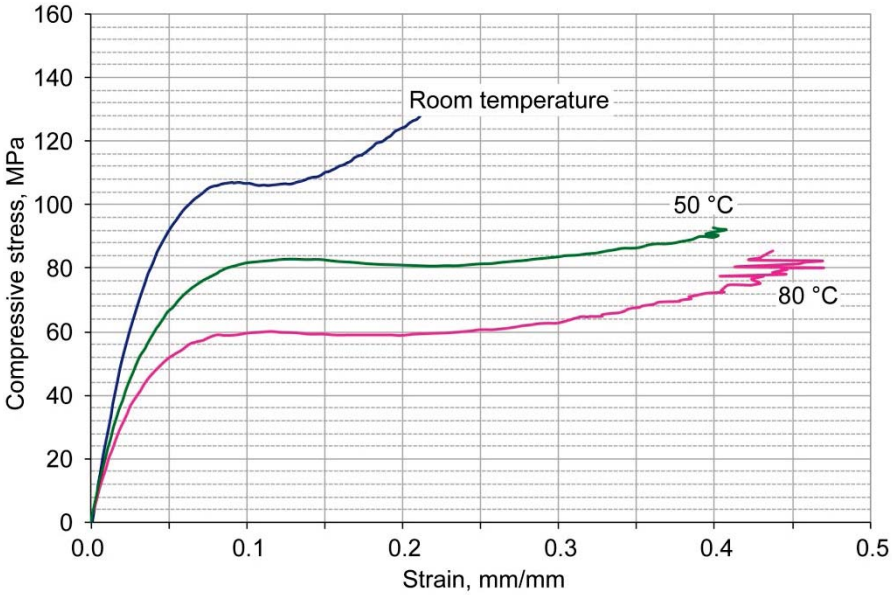

Figure 3.12.—Compressive stress-strain response for E862 resin at 10^{-3} s^{-1} strain rate and three temperatures.

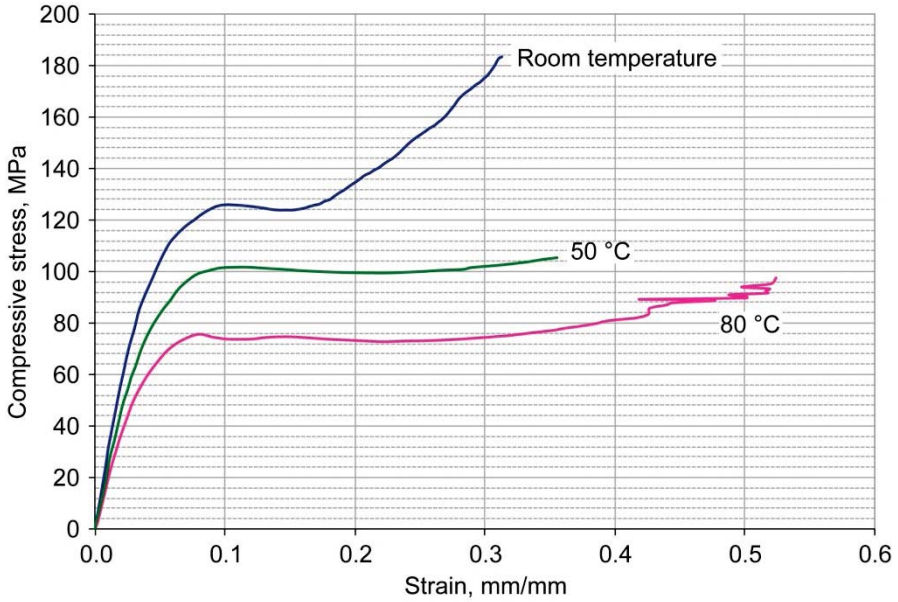

Figure 3.13.—Compressive stress-strain response for E862 resin at 10^{-3} s^{-1} strain rate and three temperatures.

in stress is 29 percent between room temperature and 50 °C and is 34 percent between 50 and 80 °C. This result shows that the temperature dependency of the material is not dependent on the strain rate.

The specimen compressive material response curves are different from the response under tensile conditions. Instead of reaching an upper and a lower yielding point, the specimens reached yielding at a plateau point before rising at the onset of buckling.

3.5.3 Shear Results

Engineering stress was plotted against torsional shear strain. Engineering stress was used to keep consistency in the data gathered. As with the tensile and compressive tests, points were picked in the middle of the gauge section and averaged to obtain a final stress-strain curve. Figure 3.14 shows the full-field shear strain calculations at approximately 50 percent strain.

As Figure 3.14 shows, there was a region of uniform shear strain along the perimeter of the specimen throughout the gauge section, and it is assumed to be uniform around the entire specimen. Because the optical measurement system only computed and displayed shear strain values as engineering shear strain, these values were multiplied by 2 to achieve the correct tensorial shear strain.

In many cases, the shear specimen broke catastrophically once it reached 70 percent strain as a result of the extreme angle of twist on the specimen. Figure 3.15 shows a shear specimen failure.

Again note that in Figure 3.15, postfailure strains that represent a permanent plastic deformation were able to be measured on the failed specimen. As with the tensile and compressive tests, plots of engineering shear stress τ versus tensorial shear strain curves are presented in Figures 3.16 to 3.18. Engineering shear stress was found by

$$\tau = \frac{Tc}{J} \tag{3.1}$$

where the variable T represents the torque exerted on the specimen, the variable c is the outer radius of the gauge section, and J is the polar moment of inertia. To plot the shear stress-strain curves, the assumption that the torque and corresponding shear stress are uniform throughout the entire wall had to be made.

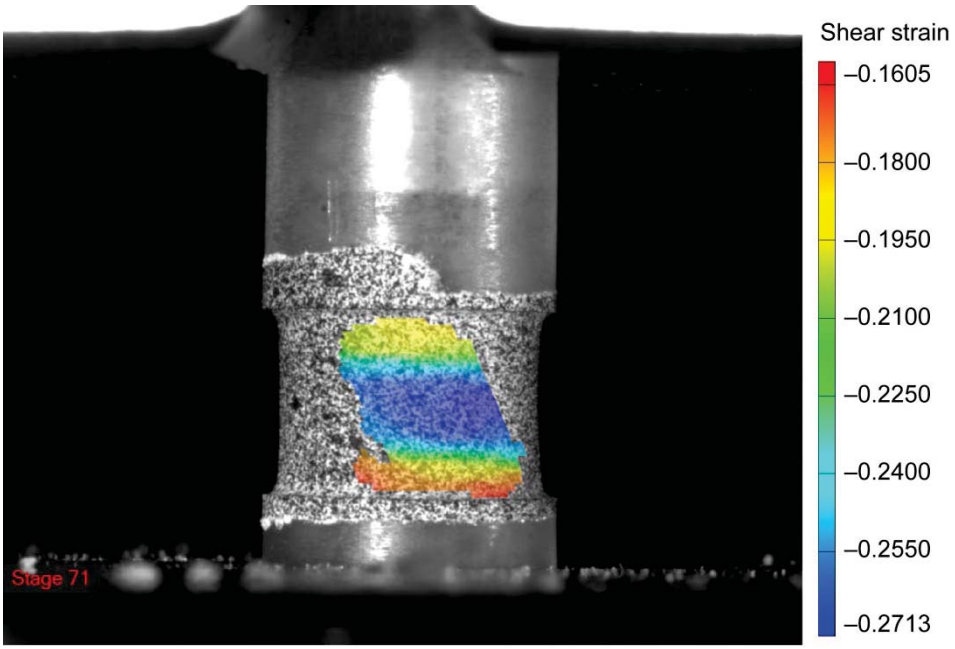

Figure 3.14.—Typical shear strain distribution in E862 resin shear specimen.

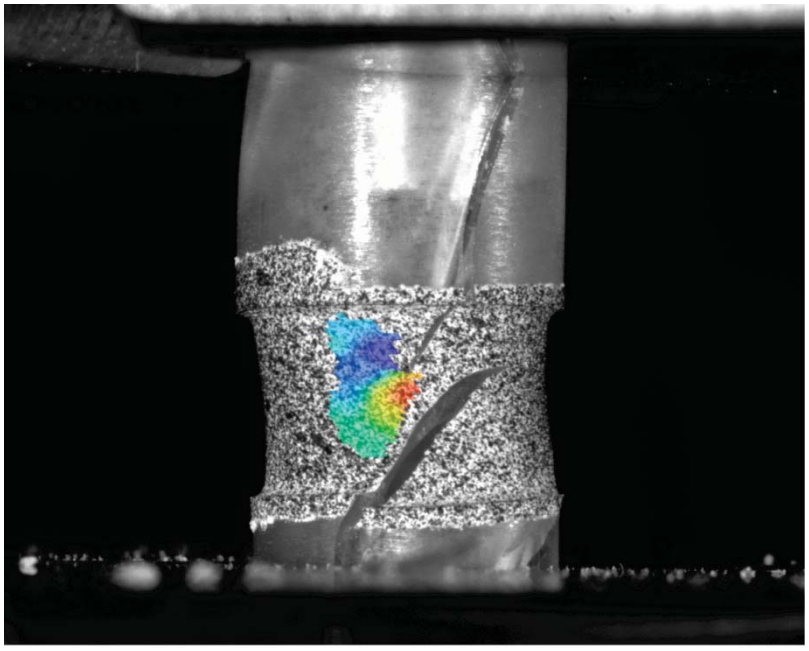

Figure 3.15.—Failure in typical E862 resin shear specimen.

The shear stress-strain curves in Figure 3.16 exhibit the same trends as the tensile and compressive material response curves, with the highest ultimate stress occurring at the highest strain rate tested (1.6×10^{-1} s^{-1}). Going from the lowest rate (1.6×10^{-5} s^{-1}) to the medium rate (1.6×10^{-3} s^{-1}) show an increase of 19 percent in the ultimate stress, and going from the medium rate to the highest rate show an increase of 16 percent. These increases are consistent between both the tensile and compressive results. When going from the lowest to the medium rate tested, the tensile results show a 17-percent increase, and the compressive results show a 15-percent increase. When going from the medium to the highest strain rates,

the tensile results show a 16-percent increase, and the compression results show an 18-percent increase. The data prove that effects of strain rate are equal between tension, compression, and torsional testing.

Figure 3.17 shows the effects of temperature at the medium strain rate (1.6×10^{-3} s^{-1}) tested. Again, trends agree between both the tensile and compressive results. When going from room temperature to 50 °C (122 °F), the ultimate stress decreases by 17 percent, and when going from 50 to 80 °C (176 °F), the ultimate stress decreases by 38 percent. However, no conclusions can be drawn about the ultimate strain, as all three temperatures show that the specimens failed at approximately 0.7 ultimate strain.

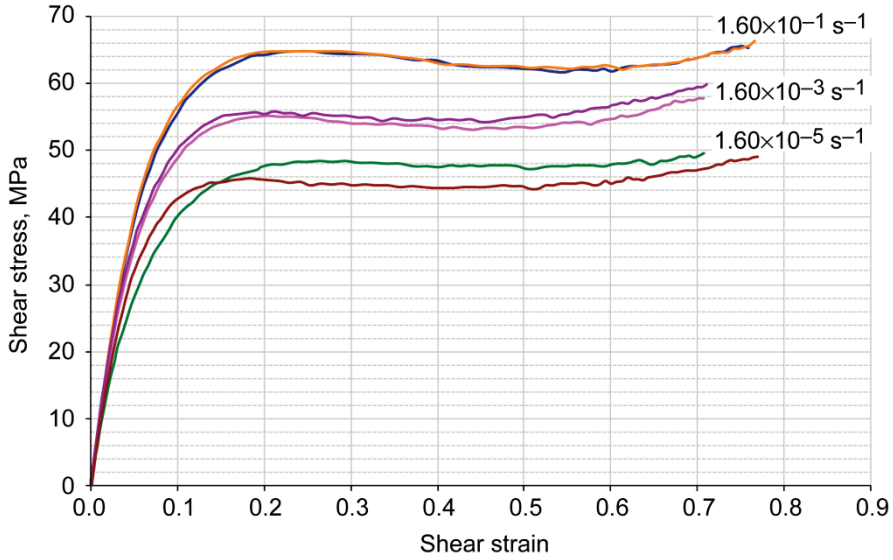

Figure 3.16.—Shear stress-strain response for E862 resin at room temperature.

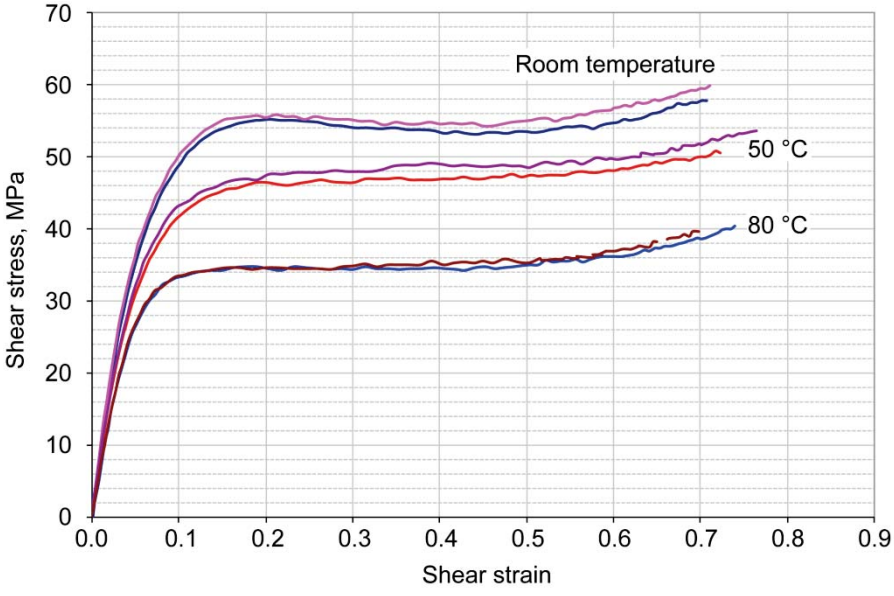

Figure 3.17.—Shear stress-strain response for E862 resin at 1.6×10^{-3} s^{-1} strain rate and three temperatures.

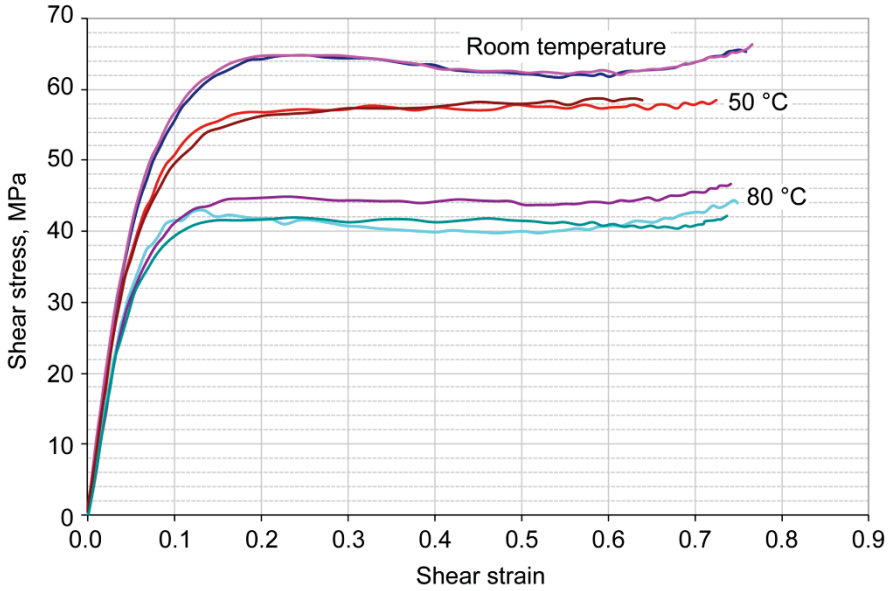

Figure 3.18.—Shear stress-strain response for E862 resin at 1.6×10^{-1} s^{-1} strain rate and three temperatures.

Figure 3.18 shows the effects of temperature at the highest strain rate (1.6×10^{-1} s^{-1}) tested. The ultimate stress decreases by 13 percent when going from room temperature to 50 °C and decreases by 33 percent when going from 50 to 80 °C. As with the medium-rate temperature results, ultimate strain comparisons could not be made because, again, all specimens fail catastrophically once 0.7 strain was reached. Comparing these results with the medium-rate results shows that the strain rate did not have an effect on the temperature results in that the percent decreases between the temperatures were similar for the two strain rates.

3.5.4 Cyclic Load-Unload Results

Load-unload tests in tension, compression, and shear were also conducted at strain rates of 1×10^{-3} s^{-1} and 1×10^{-1} s^{-1} under room temperature and elevated temperature conditions—to show the inelastic unloading and hysteresis of the resin. The unloading modulus decreased as the specimen was unloaded at higher strains because of the accumulation of plastic strain and damage in the specimens. Also, the slope of the unloading curve can be compared with the slope in the elastic region. The difference in these values can help to categorize damage parameters, which are also used in constitutive modeling.

Figures 3.19 to 3.32 each contain multiple curves that represent different tests in which the specimens were unloaded at different points while in their plastic regime. Although a full data analysis is provided by Goldberg et al. (Ref. 57), it is summarized herein for completeness.

Tensile load-unload-reload curves are shown at a strain rate of 10^{-3} s^{-1} in Figure 3.19 and at a strain rate of 10^{-1} s^{-1} in Figure 3.20. The unload points for both figures were 2, 5, 10, and 12 percent. Both figures show the nonlinearities in the unload portion of the curves, which grows more pronounced at the higher unloading points. Also note that in the 2- and 5-percent unloading curves, all the strain is recovered, signified by showing the curve returning to zero strain. However, in the 10- and 12-percent unloading points, most—but not all—of the strain is recovered. Finally, note that the average slope of the unloading curve decreases as the point of unloading increases.

Upon reloading, the curves have their same original loading modulus and reach the original saturation stress.

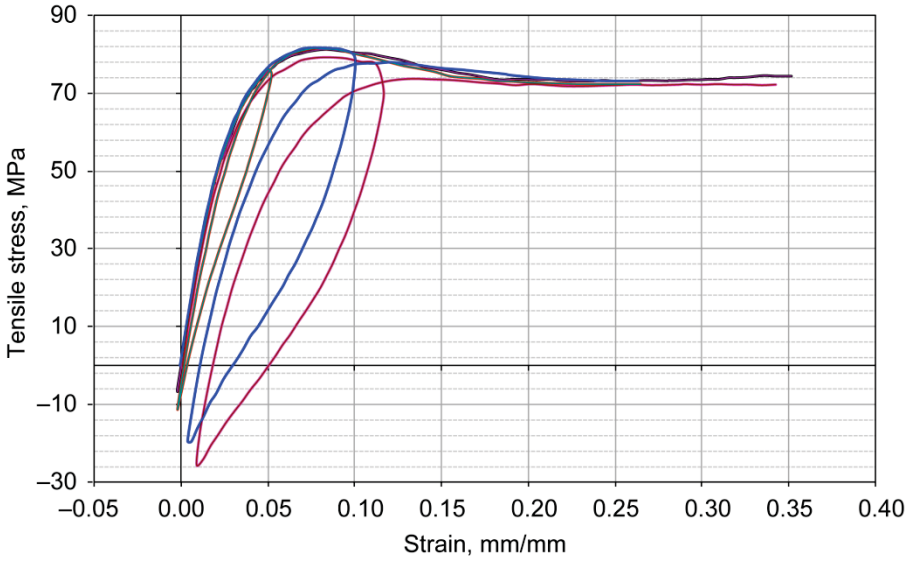

Figure 3.19.—Tensile load-unload stress-strain response for E862 resin at 1×10^{-3} s^{-1} strain rate and three temperatures.

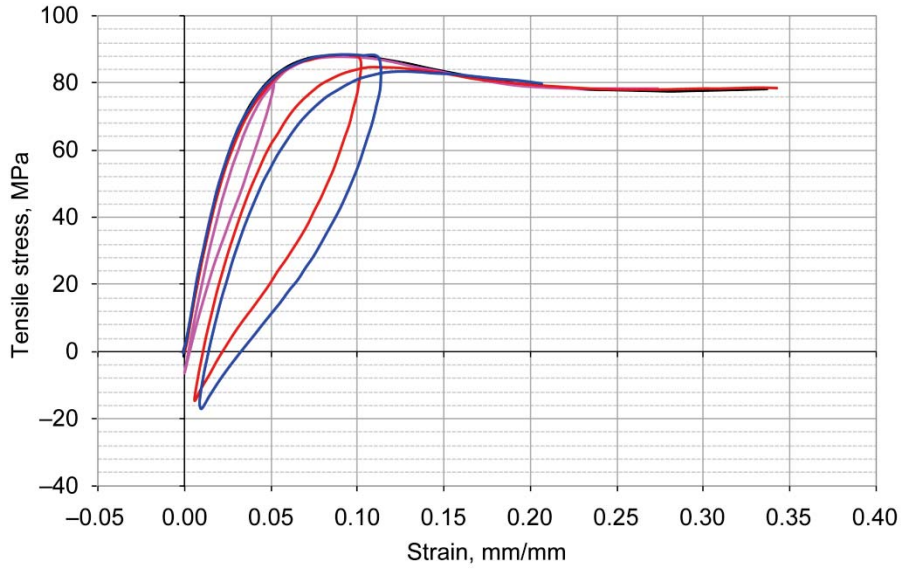

Figure 3.20.—Tensile load-unload stress-strain response for E862 resin at 1×10^{-1} s^{-1} strain rate and room temperature.

Figure 3.21 shows compression load-unload-reload curves at the 10^{-3} s^{-1} strain rate, and Figure 3.22 shows load-unload-reload curves at the 10^{-1} s^{-1} strain rate. Unloading points were set at 2, 5, 8, and 10 percent. These curves show results similar to those for the tensile curves. At 2 and 5 percent, nearly all the strain was recovered, whereas the 8- and 10-percent unloading curves show permanent plastic strain upon unload. Also, as the unloading point was increased, the value of the average unloading modulus was decreased. Upon reload, the slope of the curve follows the original loading modulus and returns to the original unloading point, following the original loading curve. The effects of hydrostatic stress on the material response are evident in the compression stress-strain curves. Also note that there is a significant amount of hysteresis present in the specimens unloaded at larger strains, which can be seen by comparing the loading and unloading portions of the curves. This hysteresis represents energy lost while loading and unloading the specimen.

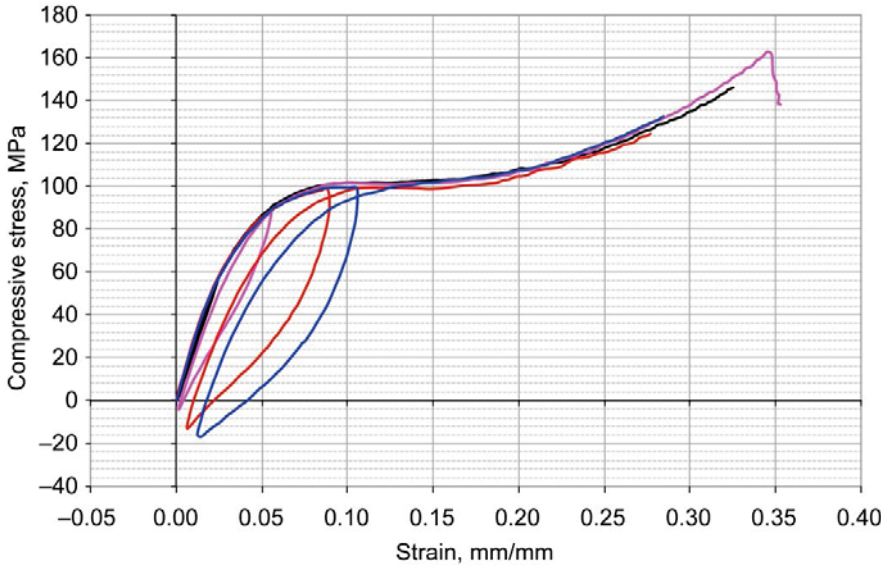

Figure 3.21.—Compressive load-unload stress-strain response for E862 resin at 1×10^{-3} s^{-1} strain rate and room temperature.

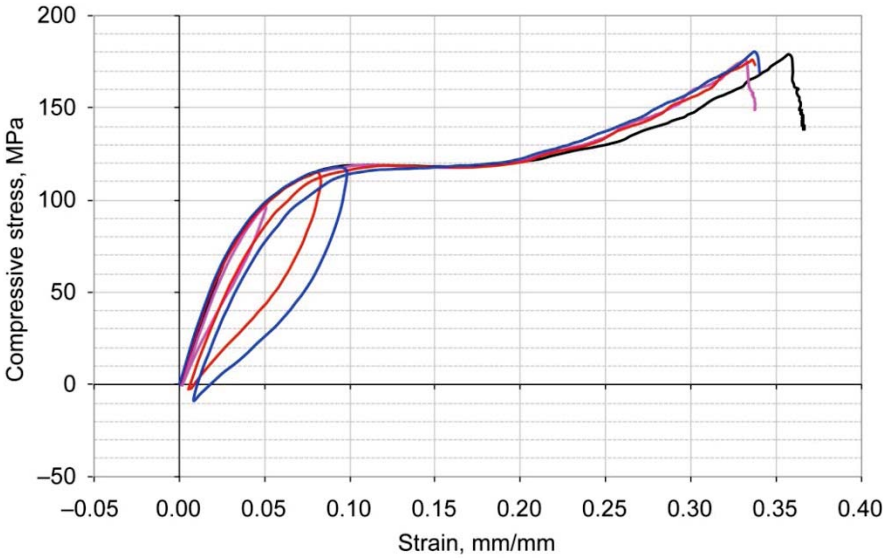

Figure 3.22.—Compressive load-unload stress-strain response for E862 resin at 1×10^{-1} s^{-1} strain rate and room temperature.

Comparing tensile and compressive load-unload-reload curves at a similar strain rate reveals the effects of the hydrostatic stresses. Using as examples Figure 3.20 (tensile load-unload-reload response at the 1×10^{-1} s^{-1} strain rate) and Figure 3.22 (compressive load-unload-reload response at the 1×10^{-1} s^{-1} strain rate) reveals the differences. The compressive ultimate stress levels reach a higher value than the tensile stress levels, and the slope of the unloading curve was less in compression than what it was in tension. As a result of this reduction in slope, the compressive unloading curve crosses the zero stress axis at a lower strain than do the tensile curves. The compressive stresses also reach a lower value at the point of maximum unloading than do the tensile curves. It was these differences that signified that hydrostatic stress plays an important role in the material response and was one of the reasons why both tensile, compressive, and shear testing was done. For completeness, the full set of load-unload-reload data are included in Figures 3.23 to 3.32.

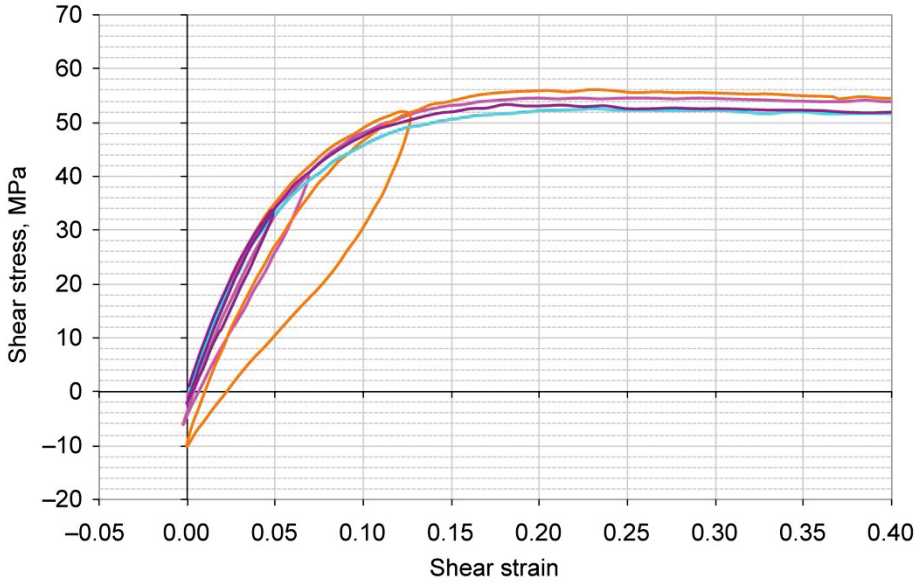

Figure 3.23.—Shear load-unload stress-strain response for E862 resin at 1.6×10^{-3} s^{-1} strain rate and room temperature.

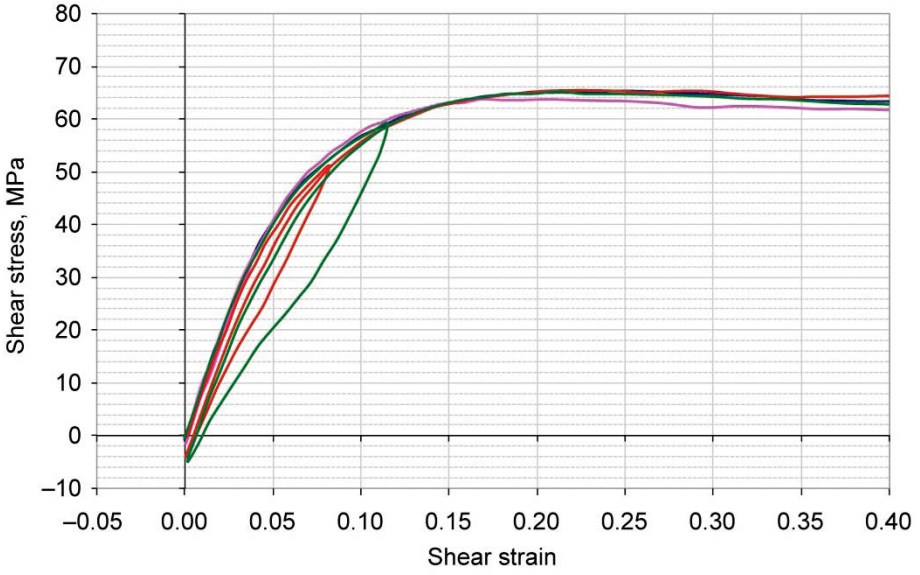

Figure 3.24.—Shear load-unload stress-strain response for E862 resin at 1.6×10^{-1} s^{-1} strain rate and room temperature.

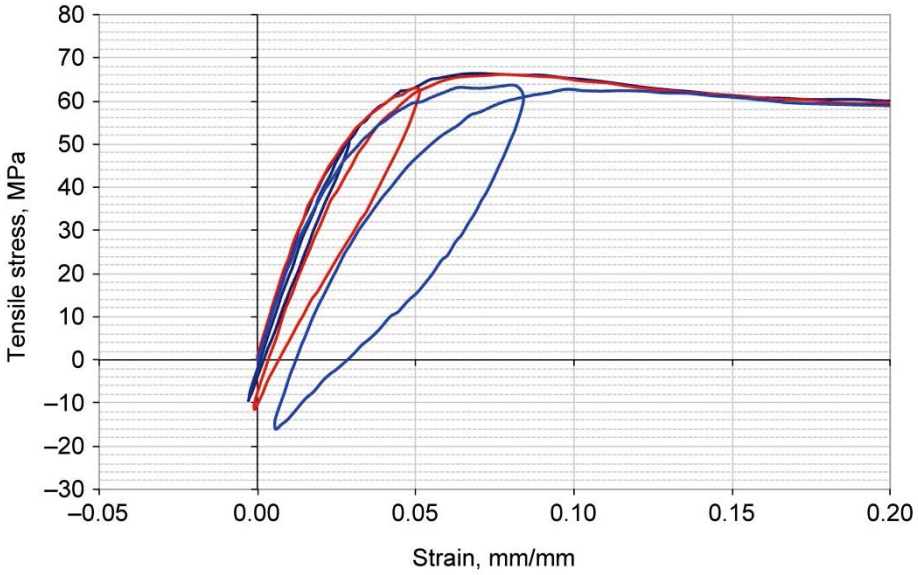

Figure 3.25.—Tensile load-unload stress-strain response for E862 resin at 1×10^{-3} s^{-1} strain rate and 50 °C.

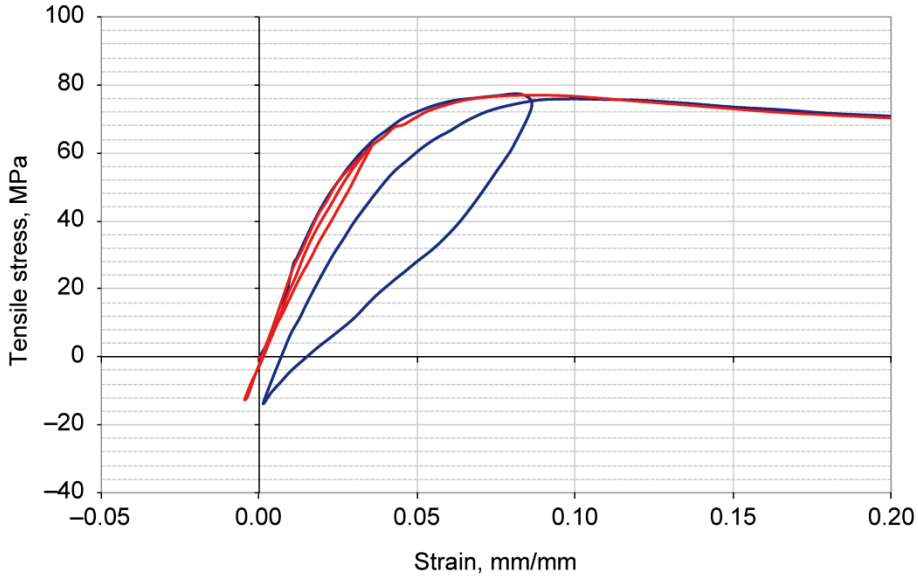

Figure 3.26.—Tensile load-unload stress-strain response for E862 resin at 1×10^{-1} s^{-1} strain rate and 50 °C.

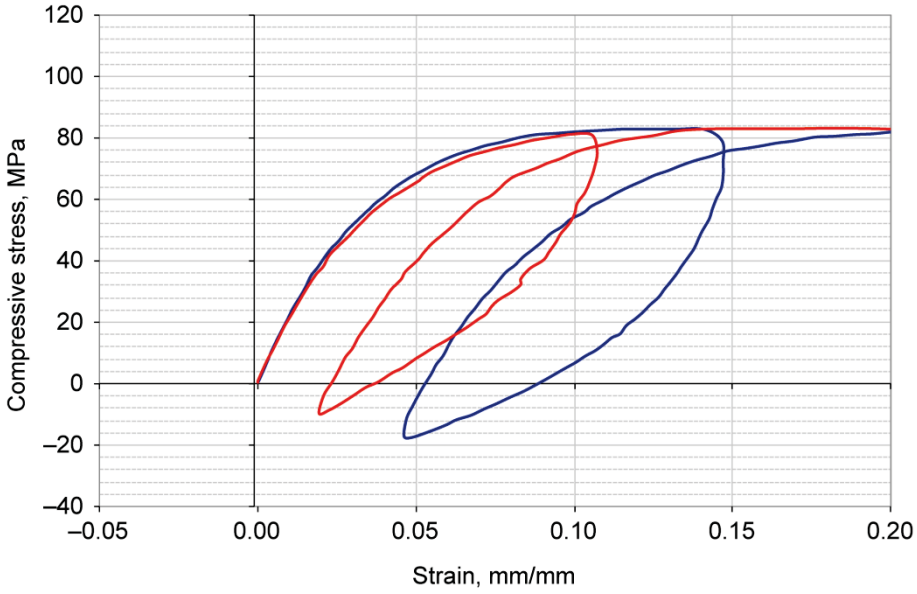

Figure 3.27.—Compressive load-unload stress-strain response for E862 resin at 1×10^{-3} s^{-1} strain rate and 50 °C.

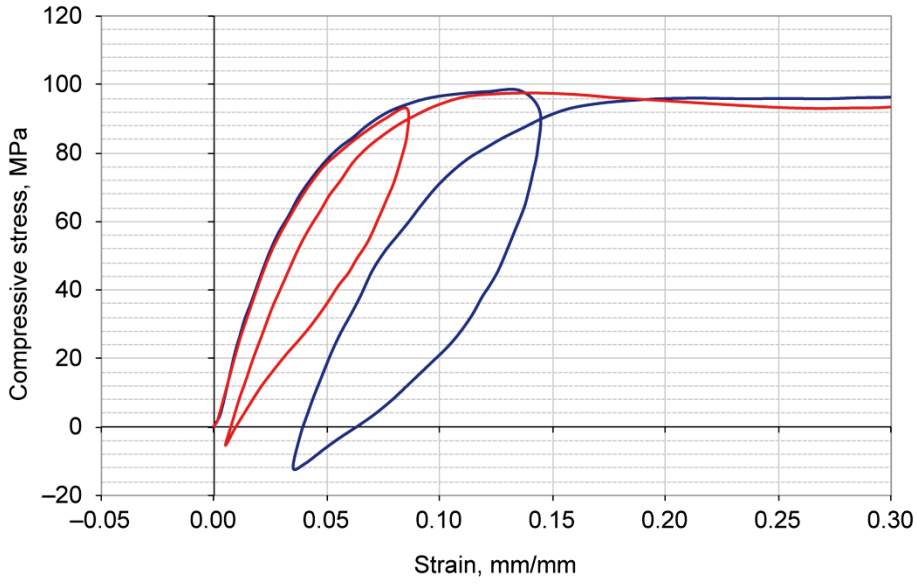

Figure 3.28.—Compressive load-unload stress-strain response for E862 resin at 1×10^{-1} s^{-1} strain rate and 50 °C.

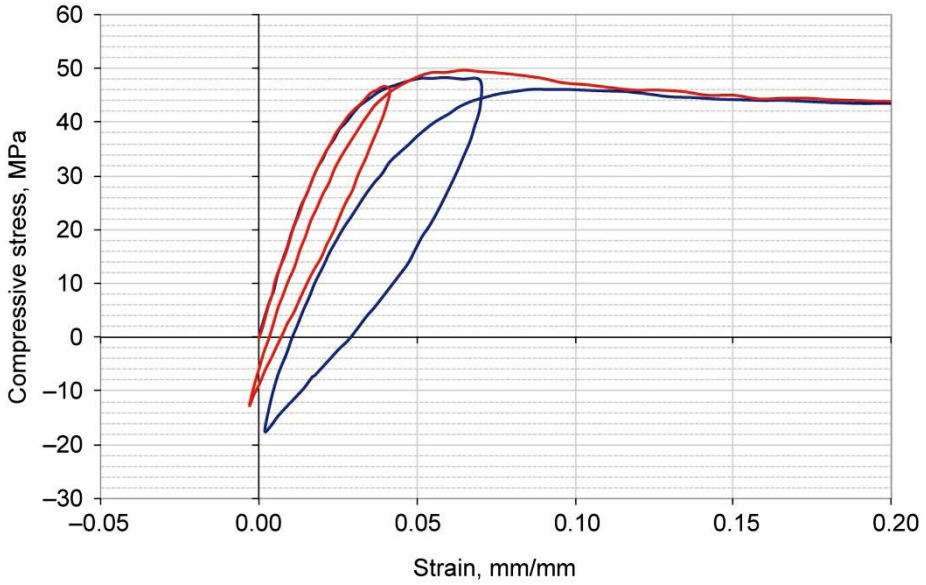

Figure 3.29.—Tensile load-unload stress-strain response for E862 resin at 1×10^{-3} s^{-1} strain rate and 80 °C.

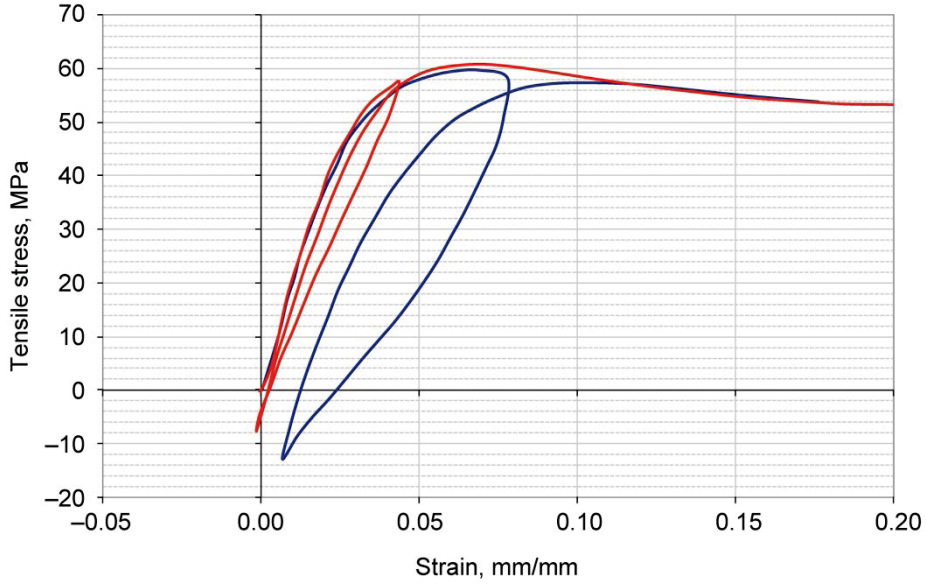

Figure 3.30.—Tensile load-unload stress-strain response for E862 resin at 1×10^{-1} s^{-1} strain rate and 80 °C.

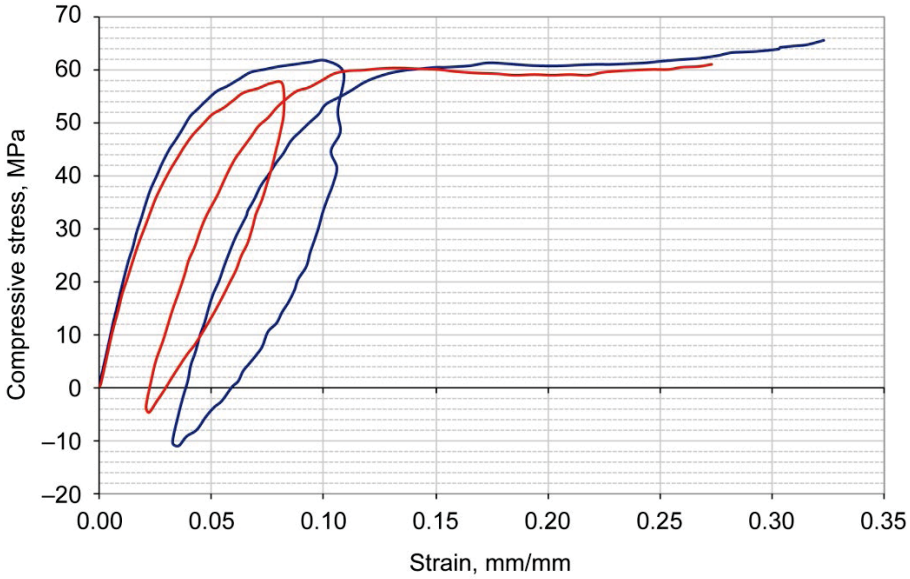

Figure 3.31.—Compressive load-unload stress-strain response for E862 resin at 1×10^{-3} s^{-1} strain rate and 80 °C.

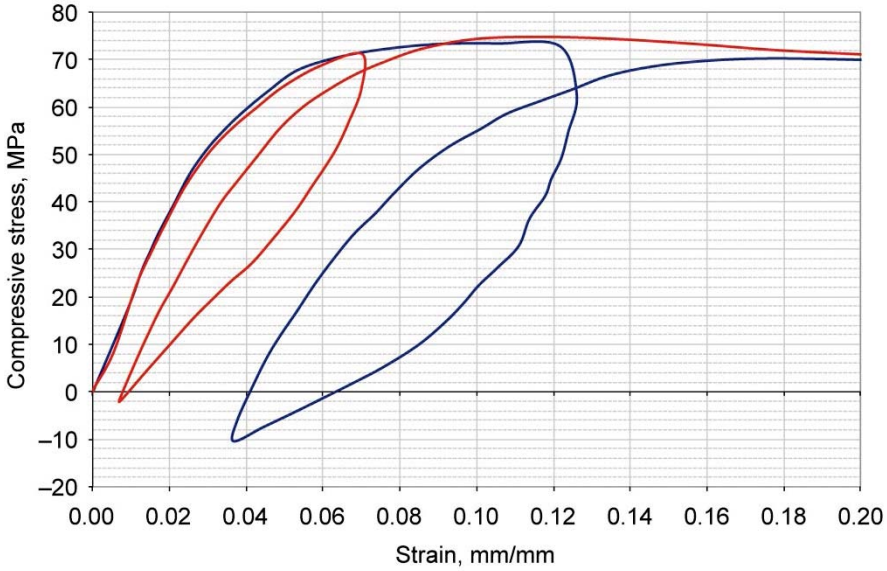

Figure 3.32.—Compressive load-unload stress-strain response for E862 resin at 1×10^{-1} s^{-1} strain rate and 80 °C.

3.5.5 Examination of Results

Examining the data in the stress-strain plots in the previous sections reveals that the stresses increase significantly with strain rate, particularly in the nonlinear range. All these curves show an initial linear response to approximately 2 percent strain and then go nonlinear after this initial region. These figures also show the consistency in the data gathered.

Although not used in the constitutive modeling development as described in Goldberg, Roberts, and Gilat (Ref. 4), the Young's modulus, Poisson's ratio, and shear modulus determined from the experimental results are listed in Table 3.1 as a check to confirm that the test method developed produced acceptable results. The Young's modulus was determined from the tensile and compressive tests, and the shear modulus was determined from the torsion tests. These values were measured for all the strain rates

and temperatures examined. Linear regression lines were used to compute the Young's modulus, shear modulus, and Poisson's ratio. The Young's and shear moduli were measured as the slope of the stress-strain curve between 0 and 1 percent strain, and the Poisson's ratio was measured as the ratio of average negative transverse strain to the average axial strain between 0 and 1 percent strain. Averaged values were used when multiple tests were conducted. Table 3.1 summarizes the results.

The data in Table 3.1 show that the Young's modulus increases as the strain rate increases, and decreases as the temperature increases for both tension and compression tests. The shear modulus also increases as the strain rate increases and decreases as the temperature increases. The Poisson's ratio stayed at a constant value of approximately 0.4±0.03 for all the tension tests, whereas in some compression tests it was measured to be as low as 0.35. Shear modulus values measured from the torsion tests were compared with the theoretical computed values from the tension and compression data using

$$G = \frac{E}{2 \times (1 + \nu)} \quad G = \frac{E}{2(1 + \nu)} \tag{3.2}$$

where G is the calculated shear modulus, E is the measured axial modulus, and ν is the measured Poisson's ratio. Comparing rows 1 to 3 (tensile data at strain rates of 10^{-5}, 10^{-3}, and 10^{-1} s^{-1} at room temperature) with rows 15 to 17 (shear data at strain rates of 1.6×10^{-5}, 1.6×10^{-3}, and 1.6×10^{-1} s^{-1} at room temperature) show this agreement. Rows 1 to 3 give calculated shear modulus values of 881, 957, and 1032 MPa (127 745, 138 765, and 149 640 psi), respectively; rows 15 to 17 give measured shear modulus values of 801, 977, and 1002 MPa (116 145, 141 665, and 149 640 psi), respectively. The differences between these values were 9, 2, and 2 percent, respectively.

TABLE 3.1.—E862 RESIN MATERIAL PROPERTIES

	Test condition			Young's modulus, GPa	Poisson's ratio	Shear modulus (measured), MPa	Shear modulus (calculated), MPa
	Temperature,[a] °C	Strain rate	Load				
1	RT	10^{-5}	Tension	2.52	0.43	–	881
2	RT	10^{-3}	Tension	2.77	0.41	–	957
3	RT	10^{-1}	Tension	2.89	0.40	–	1032
4	50	10^{-3}	Tension	2.28	0.40	–	814
5	50	10^{-1}	Tension	2.57	0.40	–	917
6	80	10^{-3}	Tension	1.95	0.40	–	696
7	80	10^{-1}	Tension	2.58	0.38	–	934
8	RT	10^{-5}	Compression	2.71	0.39	–	974
9	RT	10^{-3}	Compression	2.72	0.35	–	1007
10	RT	10^{-1}	Compression	2.96	0.40	–	1057
11	50	10^{-3}	Compression	2.09	0.35	–	774
12	50	10^{-1}	Compression	2.29	0.35	–	848
13	80	10^{-3}	Compression	1.66	0.37	–	615
14	80	10^{-1}	Compression	1.90	0.35	–	703
15	RT	1.6×10^{-5}	Shear	–	–	801	–
16	RT	1.6×10^{-3}	Shear	–	–	977	–
17	RT	1.6×10^{-1}	Shear	–	–	1002	–
18	50	1.6×10^{-3}	Shear	–	–	768	–
19	50	1.6×10^{-1}	Shear	–	–	823	–
20	80	1.6×10^{-3}	Shear	–	–	692	–
21	80	1.6×10^{-1}	Shear	–	–	718	–

[a]RT is room temperature.

Rows 8 to 10 in Table 3.1 give compression data at room temperature at the three strain rates. Comparing these calculated shear modulus values from the compression tests with measured shear modulus values in rows 15 to 17 also show good agreement: The calculated shear modulus values of 974, 1007, and 1057 MPa (141 230, 146 015, and 153 265 psi) differ by 21, 3, and 5 percent from values of 801, 977, and 1002 MPa (116 145, 141 665, and 149 640 psi), respectively.

When comparing the tensile and shear data at higher temperatures, the differences at 50 °C (122 °F) are 11 and 6 percent at 10^{-1} and 10^{-3} s^{-1} strain rates, respectively, and the differences at 80 °C (176 °F) are 30 and 1 percent at 10^{-1} and 10^{-3} s^{-1} strain rates, respectively. The 30-percent difference in the high-rate data represents an anomaly in the data. The averaged tensile modulus values for the 10^{-1} s^{-1} strain rate at 80 °C represents an average of 2.9 and 2.2 GPa (420 607.3 and 319 081 psi). By neglecting the 2.9-GPa (420 607.3-psi) test and only using the 2.2-GPa (319 081-psi) value for data comparison, the difference between the tensile calculated and the shear measured modulus is only 12 percent.

3.6 Constituent Testing Summary

The test method developed and the low-rate test data presented can provide an understanding of the mechanical behavior of this material and guidance for the development and characterization of constitutive models. Once formulated, these material models can be implemented in micromechanical computer models as user materials. Conversely, for quick approximations of material response, data can also be easily implemented in tabular form into computer model material models.

Section 4.0 will discuss test methods that were developed for composite coupons as well as the results that provided information about the material response and the interactions between the carbon fibers and the resin matrix.

4.0 Investigations of Triaxial Braided Composite Material Response

Triaxial braided carbon-fiber preforms, as opposed to traditional laminated composite layups, have enabled composite structures with complex shapes to be designed and fabricated with a fiber architecture optimized locally for overall performance. One potential mechanism that may account for the difference in performance between braided composites and traditional composites is the load transfer between fiber bundles within the braid in triaxial braided composites. Hence, a more detailed investigation of the deformation and failure processes in triaxial braid composites is presented in this section. The composite test methods developed not only examine overall material response by presenting a series of stress-strain curves, but also provide information about the nature of progressive composite failure by developing a methodology using optical measurements to directly measure the local failure mechanisms.

4.1 Material Background

Four fiber/resin material systems were examined for this research. The four material systems all had the same fiber but were infused with a different resin. Toray's T700 carbon fibers (Toray Industries, Inc.) were infused with four different resin systems—CYCOM PR 520 (Cytec Industries, Inc.), 5208 (Cytec), Epon 862 (Momentive Specialty Chemicals, Inc.), and Hercules 3502 (Hexcel Corporation)—that were used to fabricate the finished composite panels. The Toray fiber was a high-strength, standard modulus fiber used in applications where tensile strength was needed. The fibers are known to behave as linear elastic material exhibiting an abrupt or brittle failure when the maximum failure strain and stress are reached. Table 4.1 gives the properties of the T700 fiber as reported by Toray.

The Cytec CYCOM PR520 resin is a one-part toughened thermoset resin with a cure temperature of 179 °C specifically designed for resin transfer molding (RTM) processes. The Cytec 5208 resin is an untoughened thermoset resin with a cure temperature of 177 °C (350 °F). The Epon 862 resin, which is discussed in the previous section, is a low-viscosity, high-flow thermoset resin ideal for RTM. The Hexcel 3502 resin is a general purpose thermoset resin with a cure temperature of 177 °C. The resins were chosen because they could withstand elevated temperature applications and were usable up to

104 °C (220 °F) temperature environments. Table 4.2 lists the mechanical properties of each resin as reported by the manufacturer (unless noted).

The triaxial braid fiber geometry was formed at A&P Technology, Inc., in Cincinnati, Ohio. Triaxial braided performs in the shape of 38.79-cm- (15.27-in.-) diameter tubes were used to create the 0°, ±60° architecture for these panels. There were 24 000 individual axial carbon fibers in the axial (0°) fiber bundles (representing a designation of 24k wide), and there were 12 000 individual carbon fibers in the bias (±60°) fiber bundles (12k wide). The finished composite panels were quasi-isotropic in their overall material response properties. An RTM process was used to produce flat composite panels 61 cm (2 ft) long by 61 cm (2 ft) wide by 0.318 cm (0.125 in.) thick. Three layers of the flattened braided tube were placed in the RTM mold with 0° (axial) fibers aligned, and resin was injected and cured at North Coast Composites in Cleveland, Ohio, under conditions specified by each resin manufacturer. The cured composite panels had six layers of braid (two layers per flattened tube) and had a total thickness of 0.318 cm.

Figure 4.1 shows an example of the standard 0°, ±60° fiber braid architecture not infused with resin—a triaxial braid with the axial fibers aligned vertically (only partially visible, noted by the arrows). A single unit cell is highlighted; the entire composite material can be recreated by aligning repeating patterns of this single unit cell. The unit cell in the triaxial braid geometry contains two axial fiber tows underneath a –60° and +60° layer with areas between the axial tows where the bias fibers cross.

TABLE 4.1.—COMPOSITE FIBER PROPERTIES

	Tensile strength, MPa	Young's modulus, GPa	Failure strain, percent	Density, g/cm^3
Toray T700 fiber	4900	230	2.1	1.80

TABLE 4.2.—COMPOSITE RESIN PROPERTIES

Resin	Tensile strength, MPa	Young's modulus, GPa	Density, g/cm^3
Cytec CYCOM PR520	82	4.0	1.256
Cytec 5208	50	3.8	1.263[a]
Hexcel 3502	33	3.6	1.266
Epon 862[b]	61	2.7	1.200[a]

[a]Measured value.

[b]Momentive Specialty Chemicals, Inc. Values reported at 2.5 h cure time.

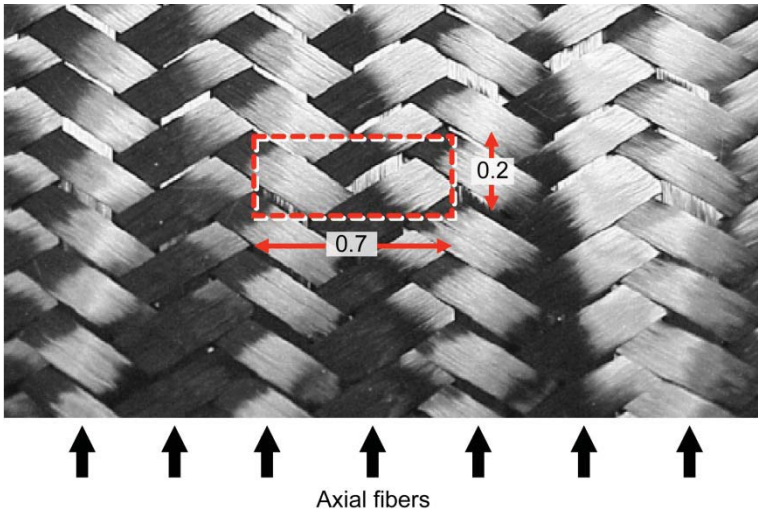

Figure 4.1.—Example two-dimensional triaxial composite braid. Dimensions are in inches.

TABLE 4.3.—FIBER VOLUME FRACTIONS
IN COMPOSITE MATERIAL SYSTEMS

Material system[a] (fiber/resin)	Fiber volume fraction, percent
T700/E862	55.6±2.42
T700/PR520	55.9±0.18
T700/3502	59.9±4.64
T700/5208	53.0±3.30

[a] T700, Toray Industries, Inc.
Epon 862, Momentive Specialty Chemicals, Inc.
CYCOM PR 520, Cytec Industries, Inc.
3502, Hexcel Corporation.
5208, Cytec Industries, Inc.

The nominal fiber volume fraction for the fabricated panels was 56 percent. An acid digestion technique procedure was used in accordance to ASTM D3171 (Ref. 61) on representative composite samples from each of the material systems, and the results are shown as an average with ±1 standard deviation in Table 4.3.

4.2 Specimen Geometries

Test specimens were cut from the panels using an abrasive waterjet technique, which was used to minimize machining times. Straight-sided tensile test specimens were cut in accordance with ASTM D3039 (Ref. 17). Rectangular 30-cm- (12-in.-) long by 3.579-cm- (1.409-in.-) wide dimensions were chosen for tensile test specimens. These dimensions were chosen such that the width contained at least two unit cells and the length conformed to ASTM length to width ratios. Compression test specimens were also prepared in accordance to ASTM D3410 (Ref. 18), with specimen dimensions of 15 cm (6 in.) in length by 3.579 cm in width. The compression specimens allowed for a long gripped region with short (3-cm, or 1-in.) gage section as specified by ASTM.

Both ASTM 3039 tensile and ASTM 3410 compression specimens were cut in two ways for testing. For tests designated “Axial,” the specimens were cut such that the axial (0°) fibers were parallel to the axis of loading. For tests designated “Transverse,” the specimens were cut such that the axial (0°) fibers were oriented perpendicular to the direction of loading. Figure 4.2 illustrates the geometries of the axial and transverse tension specimens along with the fiber orientations for each test.

Shear specimens were prepared using a modified version of the ASTM D5379 standard (Ref. 20). The modified design extended the gripped region of the specimens such that bending resistance was improved while the specimen was under load. The ASTM standard specimen design was also modified by extending the gage section of the specimen to include one entire unit cell. Figure 4.3 shows a schematic and dimensions of the shear specimen geometry.

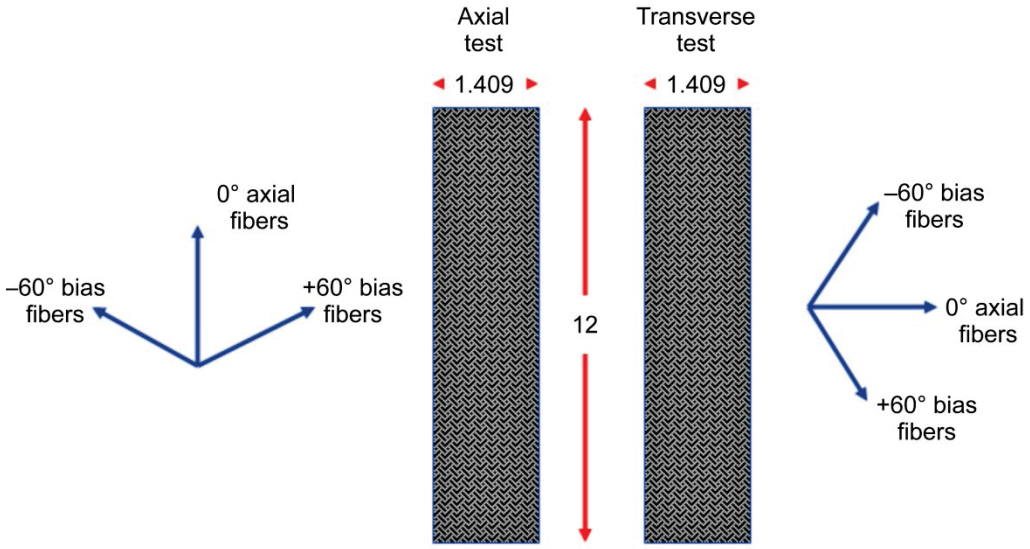

Figure 4.2.—Braided composite specimens used in tensile testing. Dimensions are in inches.

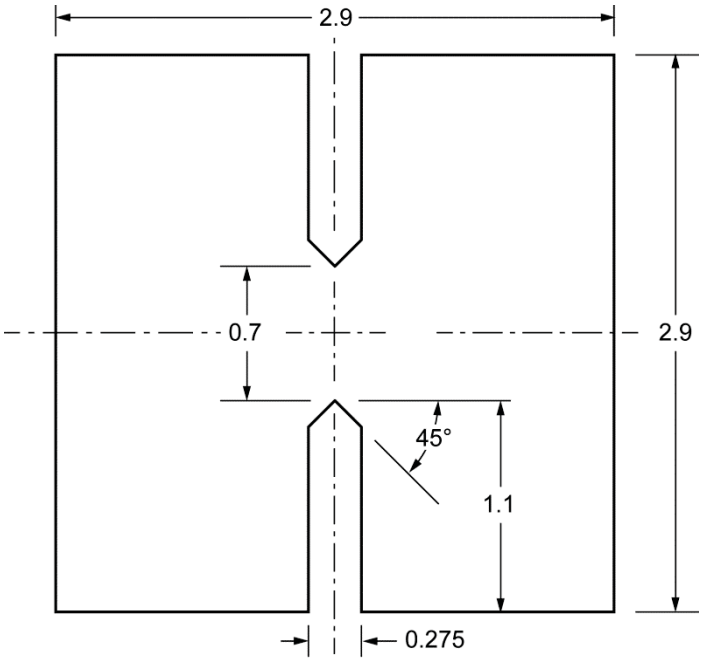

Figure 4.3.—Dimensions of shear test specimens, in inches.

4.3 Test Equipment

All specimens were tested in an MTS axial-torsional 858 test machine capable of loading to 22 680 kg (50 000 lb). All tests were conducted under displacement (stroke) control at rates of 0.635 mm/min (0.025 in./min). All strain measurements were taken using an optical measurement system. A V-Notched Rail Shear test fixture was used to facilitate the testing of the shear specimens. This fixture was manufactured by Wyoming Test Fixtures (SN WTF–NR–4). The optical measurement technique used for gathering the material property data was the same as the one described in Section 3.0. As with the previous testing, the synchronized load and strain curves were recorded by the optical measurement system. Stress-strain curves were calculated from the synchronized load and strain measurements.

4.4 Experimental Results

The next sections present the experimental results obtained from the material testing. Section 4.4.1 explains the procedure for collecting the material property data needed for the generation of the global material response curves and the results obtained, and Sections 4.4.2 to 4.4.5 will explain the local failure mechanisms that influenced the global material response.

4.4.1 Examination of Global Stress-Strain Data

Figure 4.4 shows an example of the full-field axial strain distribution acquired using the optical measurement system during an example axial tension test. The field of view captured the entire 3.579-cm specimen width and approximately 5 cm (2 in.) of the specimen height.

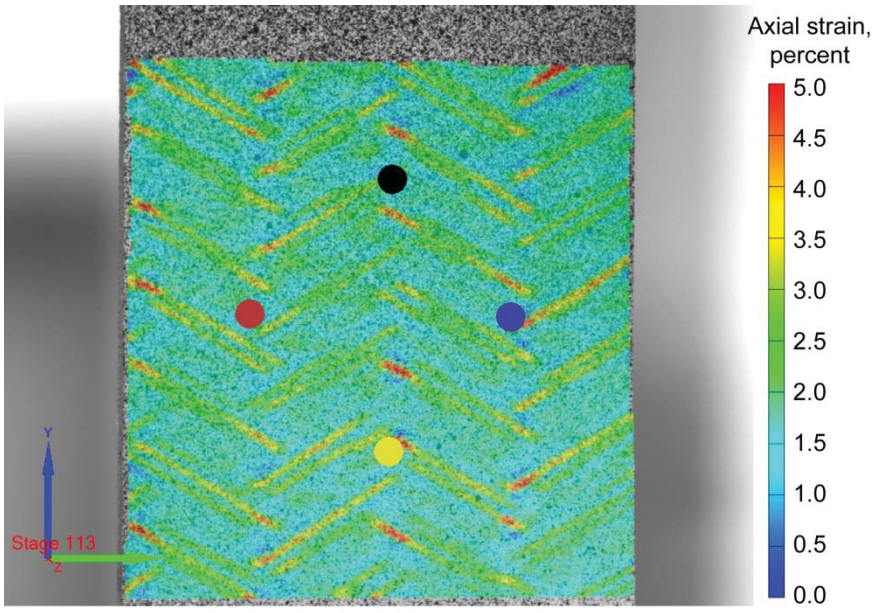

Figure 4.4.—Typical full-field strain distribution and point map used for global strain calculations during axial tension test.

By using the optical measurement system to obtain material response data, any individual point within the field of view could be picked and individual results (strains and/or displacements) could be examined. The global strains used in the specimen material response curves were found by creating a "digital strain gage" using individual data points from the full-field results on the specimen. The digital strain gage was created from four points on the surface of the specimen. The global axial strain was obtained by measuring the relative displacement between the black and yellow points (approximately 1.9 cm (0.75 in.) apart) in Figure 4.4 and dividing it by the original distance, which was measured at the beginning of the test. Similarly, transverse strain was obtained by measuring the relative displacement between the red and blue points (also approximately 1.9 cm apart) and dividing it by their original distance, also measured before the test. A distance of 1.9 cm between the points was chosen to average strain concentrations present in a particular area of the specimen, which was in agreement with guidelines proposed by Masters (Ref. 28). Global strains in the axial and transverse directions were also used to calculate a global Poisson's ratio.

Also note that in Figure 4.4 there are areas of yellow and red surrounded by areas of green. These areas of yellow and red represent regions of localized high strain concentrations. Factors contributing to these strain concentrations will be examined in Sections 4.4.2 to 4.4.5.

4.4.1.1 Tensile Testing Results

Representative global stress-strain curves for the four material systems were plotted using the method described above for both axial and transverse specimen tests. Representative global stress-strain curves are presented in Figures 4.5 to 4.8.

Material modulus values were extracted from each of the specimen's stress-strain curves by taking the slopes of the curves between 0 percent and the closest data point acquired at 0.2 percent strain. Also, failure strains and strengths were extracted from the global stress-strain curves. Table 4.4 shows the moduli, strengths, and failure strains for the material systems. A minimum of five tests were conducted to obtain the tensile results. In the cases of limited material availability, only four tests were conducted. For the T700/PR520 fiber/resin material system's transverse tests, only two tests were conducted. The results reported in Table 4.4 are a specimen average ±1 standard deviation.

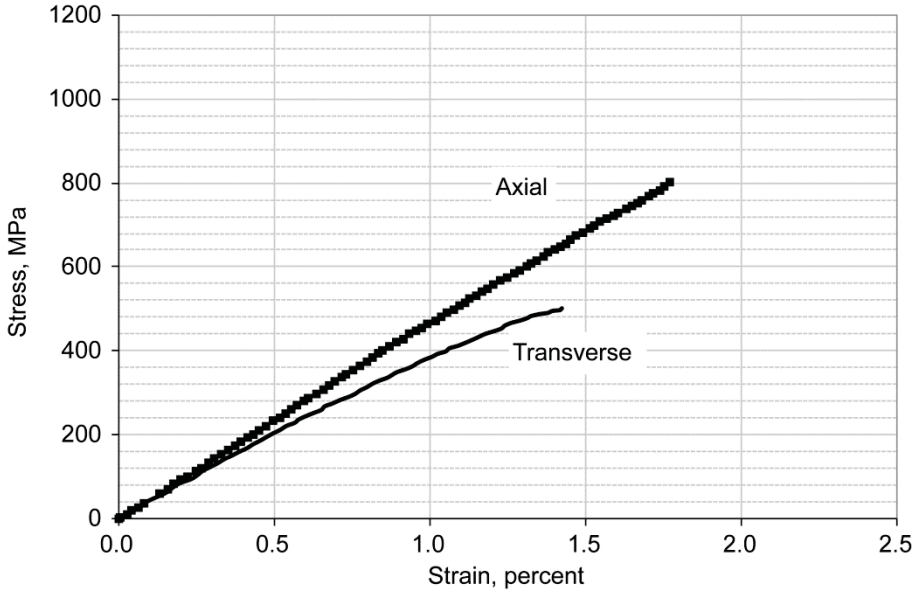

Figure 4.5.—Axial and transverse tensile stress-strain response curves for T700/E862 fiber/resin material system.

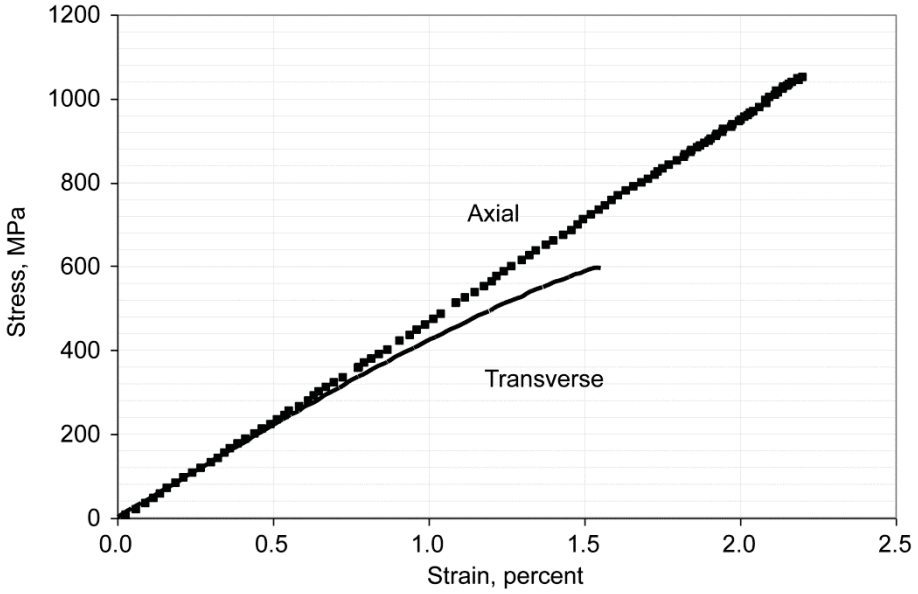

Figure 4.6.—Axial and transverse tensile stress-strain response curves for T700/PR520 fiber/resin material system.

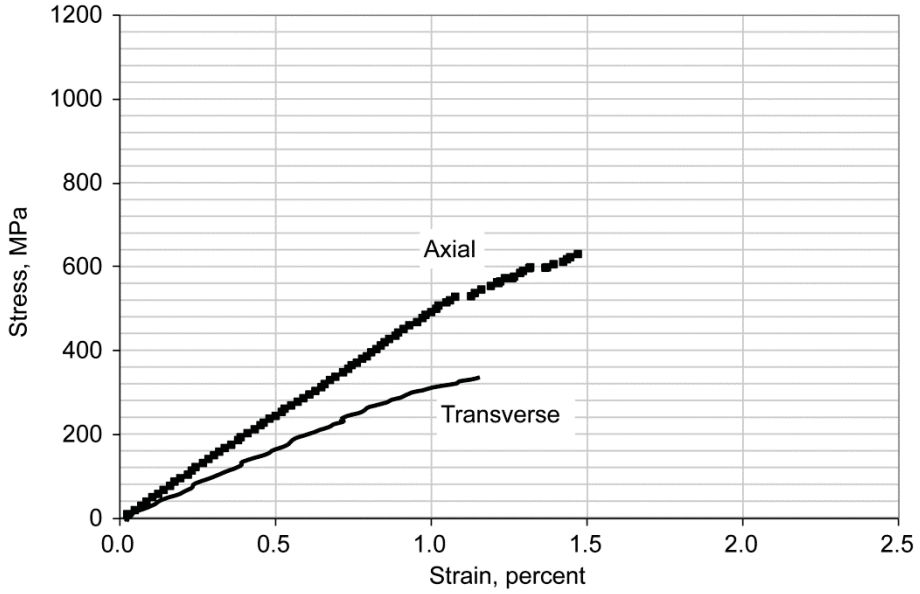

Figure 4.7.—Axial and transverse tensile stress-strain response curves for T700/3502 fiber/resin material system.

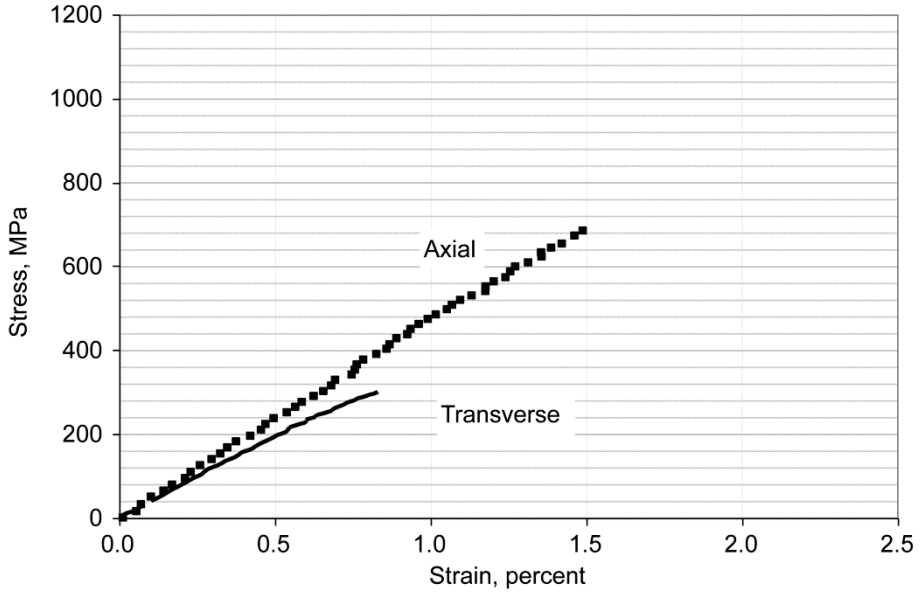

Figure 4.8.—Axial and transverse tensile stress-strain response curves for T700/5208 fiber/resin material system.

TABLE 4.4.—TENSILE RESULTS FOR FOUR COMPOSITE MATERIAL SYSTEMS

Material system[a] (fiber/resin)	Tensile property[b]					
	Axial			Transverse		
	Strength, MPa	Modulus, GPa	Failure strain, percent	Strength, MPa	Modulus, GPa	Failure strain, percent
T700/E862	800±6	46.9±1.6	1.78±0.08	462±36	41.6±1.3	1.44±0.09
T700/PR520	1046±34	47.6±1.0	2.16±0.09	599±3.3	42.0±2.3	1.69±0.19
T700/3502	608±56	47.2±2.0	1.51±0.14	336±11	40.6±4.1	1.00±0.15
T700/5208	693±46	47.5±1.0	1.51±0.10	310±15	41.3±4.5	0.85±0.05

[a]T700, Toray Industries, Inc.
Epon 862, Momentive Specialty Chemicals, Inc.
CYCOM PR 520, Cytec Industries, Inc.
3502, Hexcel Corporation.
5208, Cytec Industries, Inc.
[b]Values are shown as an average with ±1 standard deviation.

Table 4.4 shows that the T700/PR520 material system had the highest strength in both the axial and transverse directions, with the next highest being the T700/E862 system. The two lowest material systems were the T700/5208 and the T700/3502 systems. The T700/PR520 material system had an axial strength 30 percent higher than the T700/E862 system and 60 and 70 percent greater than the T700/5208 and T700/3502 systems, respectively. Likewise, the T700/PR520 material system had a transverse strength 30 percent greater than the T700/E862 system while having a transverse strength 80 and 90 percent greater than the T700/3502 and T700/5208 systems. The axial failure strain in the T700/PR520 material system was approximately 2.1 percent. This failure strain value corresponds to the ultimate failure strain in the carbon fibers reported by Toray, which are shown in Table 4.1, and indicate that in the T700/PR520 material system, the fibers dominated the composite axial failure strain, with little or no influence from the resin. However for the other three materials, the axial failure strain of the composite was less than the failure strain of the T700 fiber. The T700/E862 material system showed failure strains 25 percent less

than the ultimate fiber failure strain, while the T700/5208 and T700/3502 systems were 35 percent less than the ultimate fiber strain.

Also, the T700/PR520 material system's axial material response curve was perfectly linear until failure. The T700/E862 and T700s/5208 material systems' axial stress-strain curves started to show a nonlinear response starting at approximately 1.25 percent strain. For the lowest strength material, T700/3502, the material response curve starting showing nonlinear behavior at approximately 1.0 percent strain.

The explanation for the above observed and described material response in the axial direction was that in the three weaker material systems (T700/E862, T700/5208, and T700/3502) damage accumulation was occurring, which accounted for the nonlinear behavior in the axial material response curves. This was contrasted by the T700/PR520 material system, which showed classical fiber-dominated axial composite behavior until fiber failure. In the T700/PR520 material system, the composites' stiffness was linear elastic, and the composite exhibited brittle failure. The results from the tensile tests showed that the T700/PR520 material system had higher damage resistance, which implied that T700/PR520 had a stronger fiber-resin interface. With the other three material systems, however, the damage that occurred accumulated in the composite and played a role in the material response. In general, axial composite material response is a result of damage-causing factors such as matrix cracking, fiber breaking, and/or layer delaminations. Some or all of these classical damage mechanisms occurred in the three lower strength material systems, and it was these mechanisms that accounted for the nonlinearities encountered in the axial material response. Some of these damage-causing mechanisms will be examined in the following sections.

For composite material response in the transverse direction, the matrix material played a more important role in the material response. Unlike the axial direction, where there were continuous axial fibers that extended from the top grip to the bottom grip and throughout the entire length of the gage section and along the loading direction, the transverse composite coupon specimen geometries oriented the axial fibers transversely to the direction of loading. Because there were no continuous axial or bias fibers extending throughout the entire gage section, the primary load-carrying mechanisms in the composite were the matrix and fiber-matrix interface. The differences in transverse strengths as shown in Table 4.4 were attributed to differences in the matrix material and the fiber-matrix interface. For example, the PR520 resin had an ultimate tensile strength 64 percent greater than the 5208 resin, and accordingly, the data show that the T700/PR520 material system had a transverse tensile strength approximately 48 percent higher than the T700/5208 system. The other materials exhibited the same trends. The PR520 resin had a 34 percent greater strength than the E862 resin and 148 percent greater than the 3502 resin. The transverse tensile strength data show that the T700/PR520 material system had a strength 29 percent greater than the T700/E862 system and 93 percent greater than the T700/3502 system.

The global transverse stress-strain curves for T700/5208 showed that the slope of the curve became nonlinear early in the test at approximately 0.2 percent strain. This was opposed to the T700/PR520 material system, in which the transverse curve started to behave nonlinearly at about 0.6 percent strain. Again, the difference in the point in which these curves became nonlinear was attributed to damage occurring much earlier in the weakest T700/5208 material system than in the strongest T700/PR520 system. The other two material systems fell within this envelope.

The differences in the material moduli between the material systems in both the axial and transverse directions were negligible and fell within the experimental scatter. This was expected since all material systems used the same fiber, and the modulus values for the different resins were similar. Finally, a Poisson's ratio was found by taking the ratio of transverse to axial strain in both the axial and transverse test specimens' stress-strain curves to 0.2 percent. These data are presented in Table 4.5. For the data labeled Axial Poisson's ratio, the data was taken from the axial tests, and for data labeled Transverse Poisson's ratio, the data was taken from the transverse tests. An average ±1 standard deviation from each of the material systems is reported.

The Poisson's ratios of the material systems were also approximately the same in the axial direction and fell within the experimental scatter. In the transverse direction, with the exception of T700/5208, the Poisson's ratios also fell within experimental scatter of each other. Also, the Poisson's ratios in the

transverse directions matched those in the axial direction. These results validated that the material elastic properties are consistent with those of a quasi-isotropic material.

4.4.1.2 Compression Testing Results

Because of material availability, only two tests were run in each direction for the compression specimens of each material system. Figures 4.9 to 4.12 show the global stress-strain material responses for both the axial and transverse directions.

TABLE 4.5.—AXIAL AND TRANSVERSE POISSON'S RATIOS FOR FOUR MATERIAL SYSTEMS

Material system[a] (fiber/resin)	Poisson's ratio[b]	
	Axial, ν_{12}	Transverse, ν_{21}
T700/E862	0.30±0.03	0.29±0.02
T700/PR520	0.31±0.02	0.30±0.003
T700/3502	0.32±0.04	0.30±0.04
T700/5208	0.29±0.03	0.27±0.006

[a]T700, Toray Industries, Inc.
Epon 862, Momentive Specialty Chemicals, Inc.
CYCOM PR 520, Cytec Industries, Inc.
3502, Hexcel Corporation.
5208, Cytec Industries, Inc.

[b]Values are shown as an average with ±1 standard deviation.

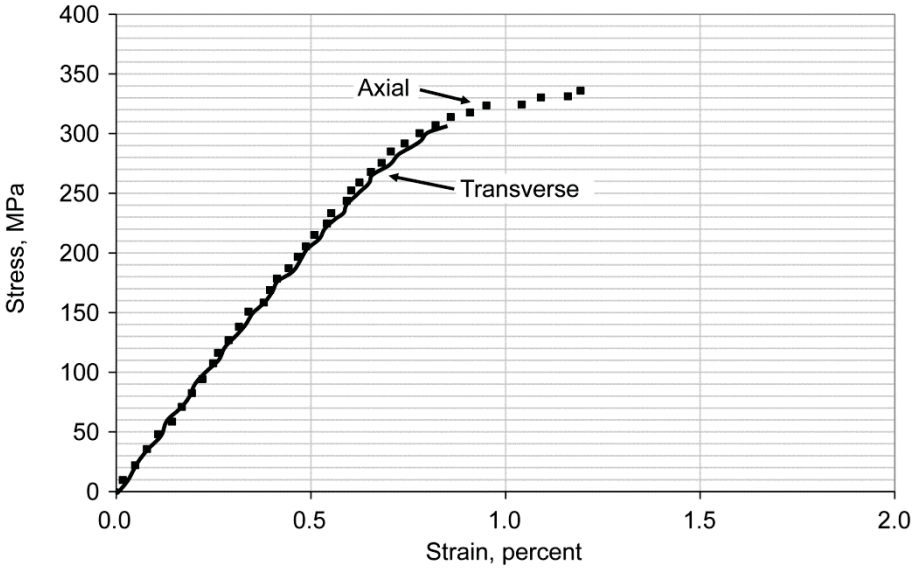

Figure 4.9.—Axial and transverse compressive stress-strain response curves for T700/E862 fiber/resin material system.

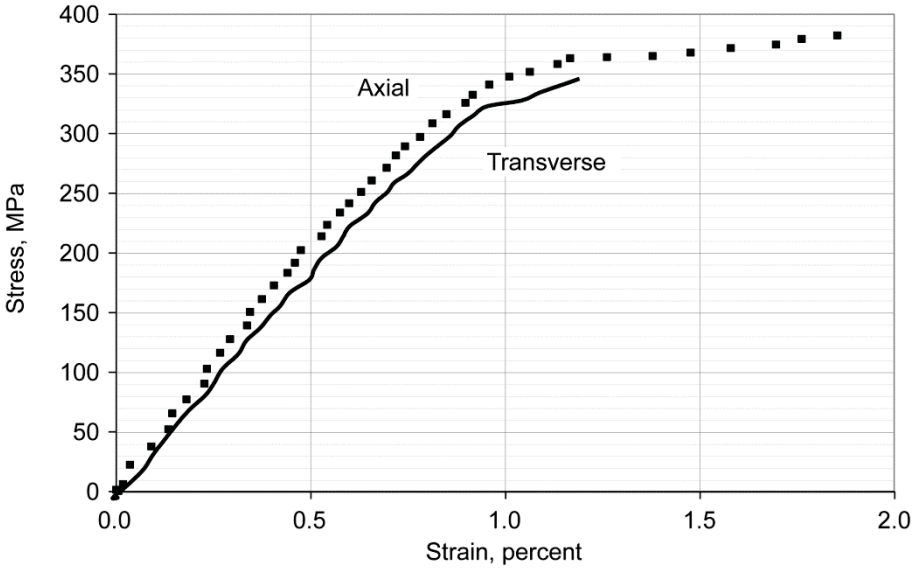

Figure 4.10.—Axial and transverse compressive stress-strain response curves for T700/PR520 fiber/resin material system.

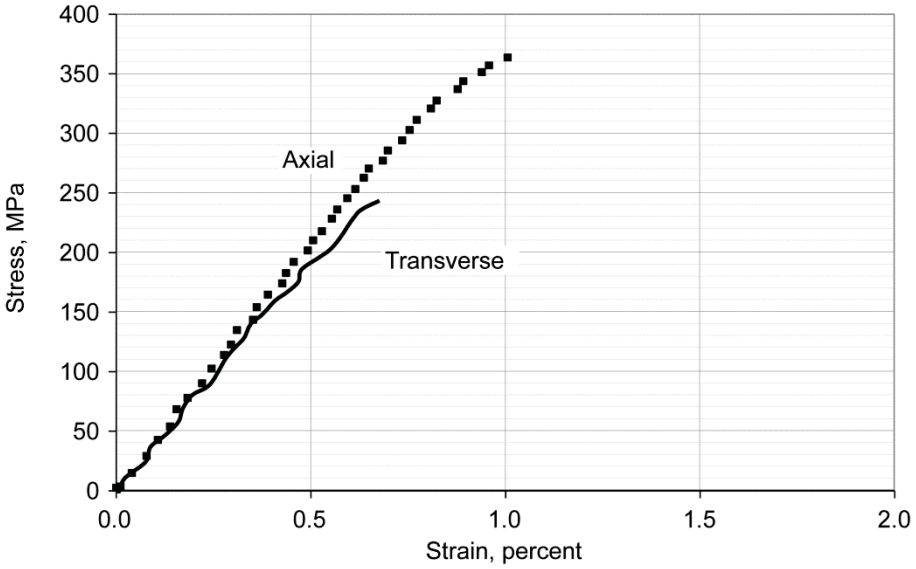

Figure 4.11.—Axial and transverse compressive stress-strain response curves for T700/3502 fiber/resin material system.

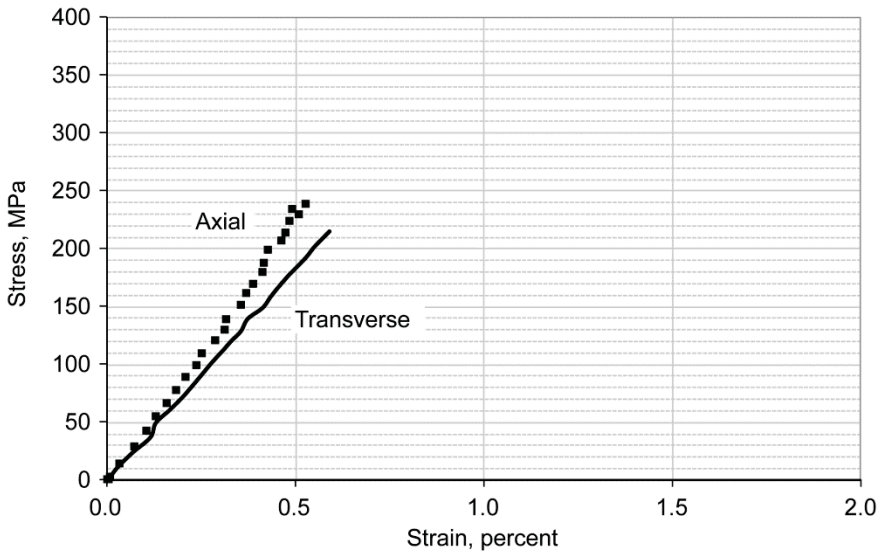

Figure 4.12.—Axial and transverse compressive stress-strain response curves for T700/5208 fiber/resin material system.

TABLE 4.6.—COMPRESSIVE RESULTS FOR FOUR COMPOSITE MATERIAL SYSTEMS

Material system[a] (fiber/resin)	Compressive property[b]					
	Axial			Transverse		
	Strength, MPa	Modulus, GPa	Failure strain, percent	Strength, MPa	Modulus, GPa	Failure strain, percent
T700/E862	327	41.4	1.01	303.5	42.7	0.87
T700/PR520	378	41.9	1.80	346	39.0	1.10
T700/3502	321	41.8	0.86	243	41.1	0.61
T700/5208	249	44.6	0.56	191	38.6	0.49

[a]T700, Toray Industries, Inc.
Epon 862, Momentive Specialty Chemicals, Inc.
CYCOM PR 520, Cytec Industries, Inc.
3502, Hexcel Corporation.
5208, Cytec Industries, Inc.

[b]Values are shown as an average with ±1 standard deviation.

Material modulus values were determined from the global stress-strain curves between 0 percent and the data point collected closest to 0.2 percent strain. Also, failure strength and strain values were obtained from the global stress-strain curves. The modulus, strength, and failure strain values were taken from the test's average.

The compression material response showed that the axial moduli are approximately the same for the four material systems. Also, the material response data showed that the transverse moduli are approximately the same between the four material systems. The material moduli are similar between the four systems because in compression, the main material carrying the load is the matrix material. The results in Table 4.6 reflect the similarities in the resin moduli. The axial strength data showed that the T700/PR520 material system is the strongest material with the T700/E862 system being the second strongest. The T700/PR520 system was approximately 18 percent stronger than T700/3502 and 52 percent stronger than T700/5208. Examining the transverse strength data, the T700/PR520 system was 14 percent stronger than T700/E862, 40 percent stronger than T700/3502, and 80 percent stronger than the T700/5208 material system. The trends in these results agreed with the tensile results, and showed that T700/PR520 is the strongest material, followed by T700/E862, T700/3502, and finally T700/5208.

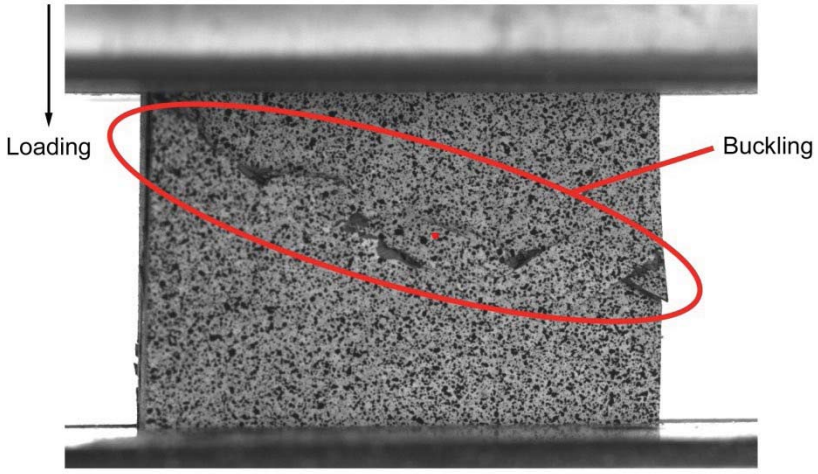

Figure 4.13.—Microbuckling in T700/3502 fiber/resin material system.

Examining the global stress-strain curves, the stronger T700/E862 and T700/PR520 material systems exhibited significant nonlinear behavior before failure in the axial direction. The inelastic regions occur because the interface strength between the fiber and resin is sufficiently high enough to allow for the resin to reach an inelastic region before the specimen failure occurs. The two weaker material systems did not display any significant nonlinear behavior, but rather failed before this regime was reached. This indicated that the interface between the fiber and resin is weak enough and allows for fiber microbuckling to occur before this inelastic regime in the resin is reached, which typically causes composite failure as shown in Reference 62.

Figure 4.13 shows the microbuckling phenomena on the macroscale for the weakest material system tested, T700/3502, as captured by the optical measurement system.

This local buckling occurred because the weak fiber-matrix interface allowed for fiber movement within the composite, which caused microbuckling in the fibers before the inelastic region of the resin was reached. This behavior was common to the two weaker material systems; however, it was absent from the stronger systems. The same phenomena occurred in the transverse testing, although the specimens buckled at an earlier global stress.

4.4.1.3 Shear Testing Results

A minimum of four tests were conducted for each material system for the shear specimens. Two tests were conducted with the axial fibers running parallel to the direction of loading, and two were conducted with the axial fibers running perpendicular to the direction of loading. Figure 4.14 shows example shear stress-shear strain material response curves for the material systems.

All three material systems' material response curves show nonlinear behavior starting at approximately 0.2 percent strain. This was due to the fact that in shear testing, as in compression testing, the main loading-carrying mechanisms are the resin and the fiber-resin interface. The strength and modulus values for each material system were determined from the curves and are presented in Table 4.7. The two orientations yielded similar results, and the results reported are for a four-specimen average ±1 standard deviation.

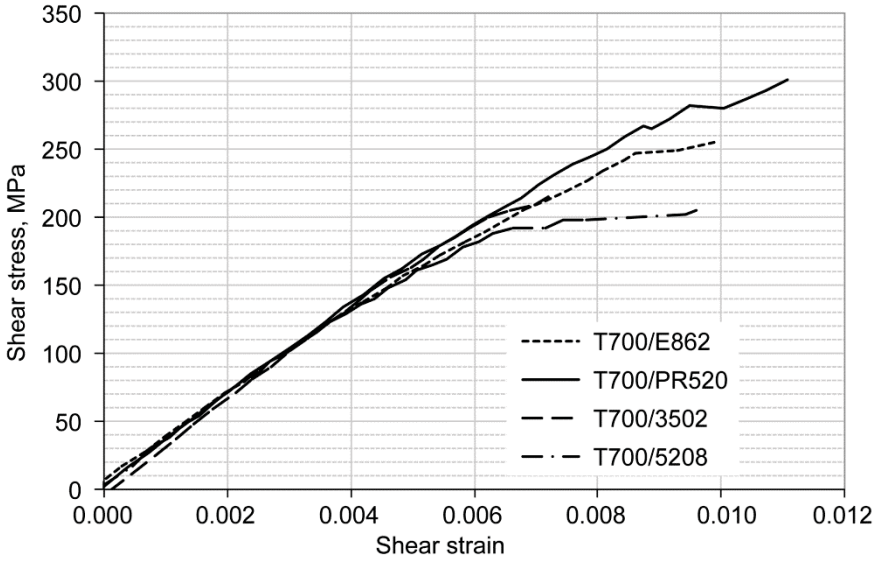

Figure 4.14.—Shear stress-strain response curves for fiber/resin material systems.

TABLE 4.7.—SHEAR RESULTS FOR FOUR COMPOSITE MATERIAL SYSTEMS

Material system[a] (fiber/resin)	Shear property[b]	
	Strength, MPa	Modulus, GPa
T700/E862	257±10	32±1.1
T700/PR520	307±6.8	34.9±0.6
T700/3502	224±30	33.7±1.2
T700/5208	200±20	33.5±0.7

[a] T700, Toray Industries, Inc.
Epon 862, Momentive Specialty Chemicals, Inc.
CYCOM PR 520, Cytec Industries, Inc.
3502, Hexcel Corporation.
5208, Cytec Industries, Inc.

[b] Values are shown as an average with ±1 standard deviation.

Table 4.7 shows the strength and modulus results for the three material systems. Trends in this table followed the tension and compression results. The T700/PR520 material system had the highest strength. It was higher than the T700/E862 system by 19 percent and higher than the T700/5208 system by 53 percent. Also, like with the other testing, the differences in the materials' moduli were negligible, which was expected since the resin moduli were similar. Since a nonstandard specimen geometry was used in shear testing, the failure of the specimen was also examined.

Figure 4.15 shows a picture of a shear specimen failure. The shear specimen is still gripped in the test machine, with the failure occurring in the gage section between the notches (circled). The nonstandard specimen geometry with the extended ends and longer notched gage section forced the failure of the material between the notches. The figure confirms that the shear specimen used in testing gave the desired failure surface and was sufficient to use for material property collection.

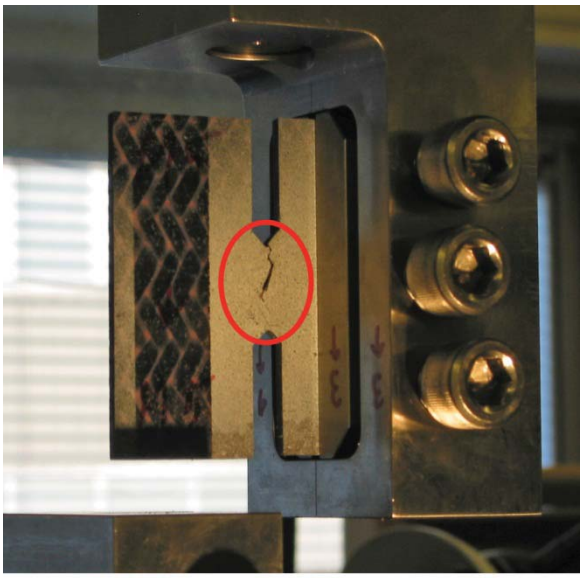

Figure 4.15.—Shear specimen failure.

4.4.2 Examination of Local Deformations and Failure

The full-field strain data in Figure 4.4 is presented to demonstrate the use of the point averaging method to obtain overall composite material response. However, it also shows an example of the occurrence of local strain concentrations typically present in the composite specimens, noted by the areas of yellow and red that appeared on the surface of the specimen. An examination of the full-field material strain in all test results revealed that such concentrations were present in all of the material systems, and the material response curves suggested that classical damage mechanisms occurring in the composite affected the material response. This section presents a closer look into the full-field strain data, providing further insight into the differences in the global material properties reported in the tables in Sections 4.4.1.1, 4.4.1.2, and 4.4.1.3.

However, because of specimen availability, not all techniques were used on all of the material systems, but rather the techniques were developed on example composite specimens to provide insight into material responses. Comparisons were done on a subset of the material systems, typically between strong (representing a high failure stress) and weak (representing a low failure stress) materials.

4.4.2.1 Development of Strain Overlay Techniques

Because the localized strain occurring in the specimen leads to global damage in the composite, the areas of strain concentrations were of interest to determine the types of damage present. Since the composite specimens were painted with the contrasting speckle pattern as described earlier to yield the full-field results, direct correlations between the full-field results and composite braid geometry locations could not be made because the braid geometry was covered by the painted speckle pattern. Full-field overlay techniques were developed to mitigate this problem by mapping the postprocessed full-field strain results onto the unpainted composite specimen. The step-by-step process by which to overlay the strain onto an axial specimen is shown in Figure 4.16 on an axial tensile specimen from the T700/PR520 material system. Figure 4.16 shows the data obtained in a representative axial composite coupon at the last data point collected before specimen failure. Part (a) shows the unpainted picture of the composite coupon taken before testing was begun. Part (b) shows the postprocessed global axial strain data obtained from the full-field measurement software after testing was completed. Part (c) shows the postprocessed strain data only. The overlay technique maps the full-field strain data onto the unpainted specimen via a

two-step process. The first step mapped the picture in part (b) onto the one in part (a) by matching the visible fiber locations and datum marks placed on the specimen. The second step mapped the picture in part (c) onto the one in part (b) by matching the common strain result locations. The picture in part (b) was then removed, leaving the final overlay with pictures from parts (a) and (c) only. Finally, the opacity on part (c) decreased such that the fiber bundles in part (a) were visible. Note that by using common datum marks, the deformed pictures could be stretched to match the unloaded specimen picture. Figure 4.17 shows the final overlay picture after the process was completed. This final image was then used to determine locations of the strain concentrations on the surface of the specimen because both the full-field strains and fiber bundle locations were visible.

The overlay in Figure 4.17 shows that the majority of the axial strain was approximately 2.19 percent (represented by the majority of the picture showing the strain in green), which is in agreement with the T700/PR520 axial failure strain data in Table 4.4. However, as Figure 4.17 shows, areas of high strain were present, as indicated by the yellow and red areas. The overlay technique shows the areas of lines of high strain present were in the middle of and running parallel to the surface bias fiber layers, which consisted of a mixture of the bias fiber bundles and surrounding resin matrix material. These areas of high strain could have been indicative of a transverse fiber bundle failure that was exposed by having the surface bias fibers "split" apart. These areas were located directly over the subsurface axial fibers, which are indicated by the black arrows in Figure 4.17.

These results were confirmed by examining a bias fiber bundle under a scanning electron microscope (SEM). Figure 4.18 shows a +60° bias fiber bundle of the T700/5208 material system removed from a tested axial specimen. Loose fibers in the failed region of the specimen were removed and scanned, with care being taken to ensure that artificial defects were not introduced into the specimen by the removal process.

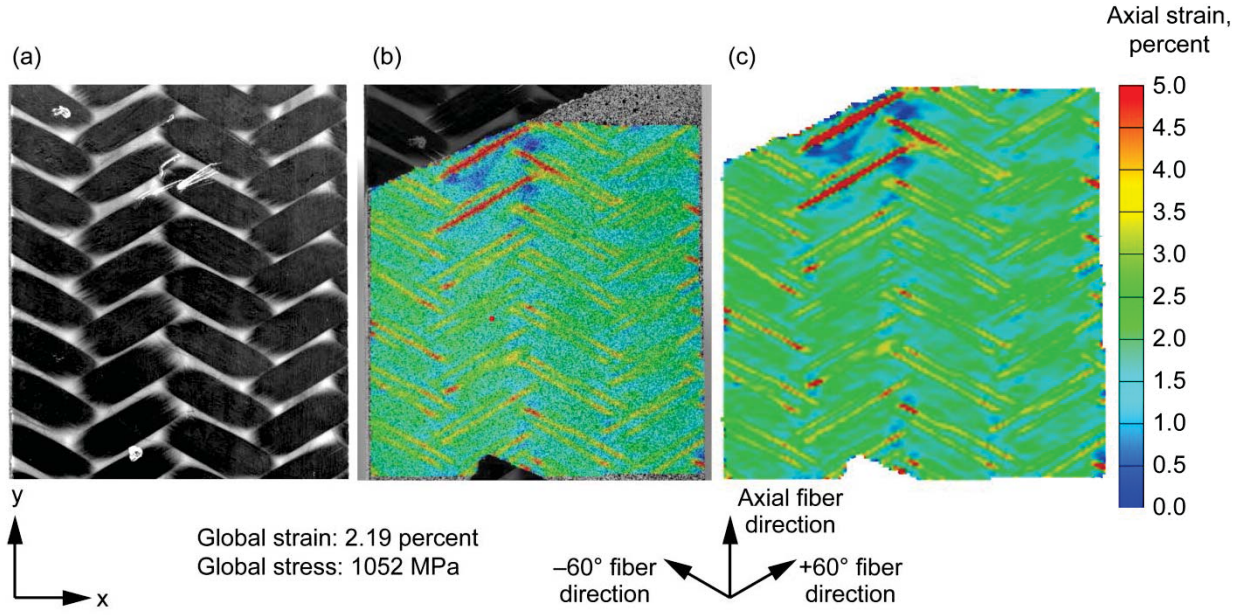

Figure 4.16.—Development of overlay technique for T700/PR520 fiber/resin material system. (a) Unpainted picture of coupon taken before testing. (b) Postprocessed global axial strain data obtained from full-field measurement software. (c) Postprocessed strain data only.

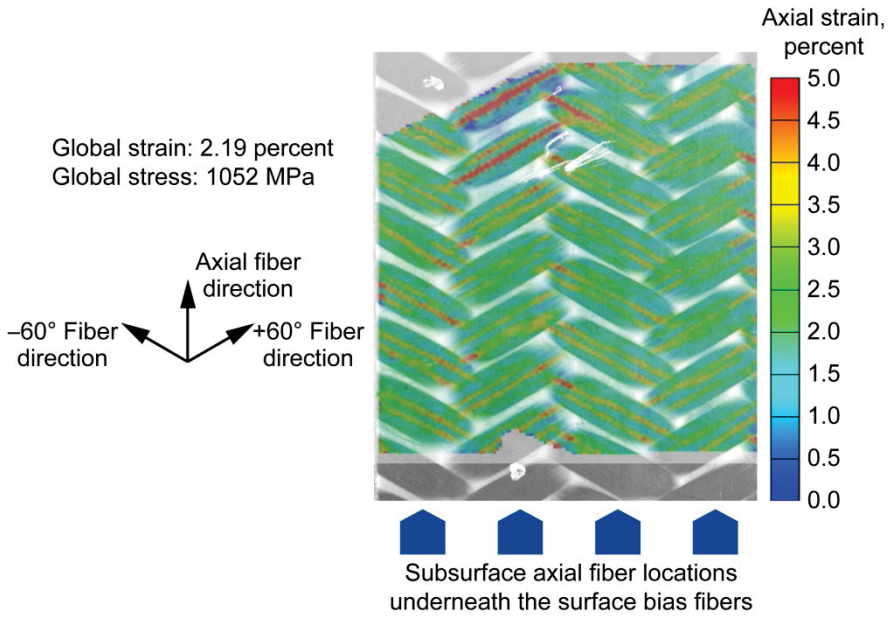

Figure 4.17.—Axial strain overlay on axial specimen (Fig. 4.16) in T700/PR520 fiber/resin material system.

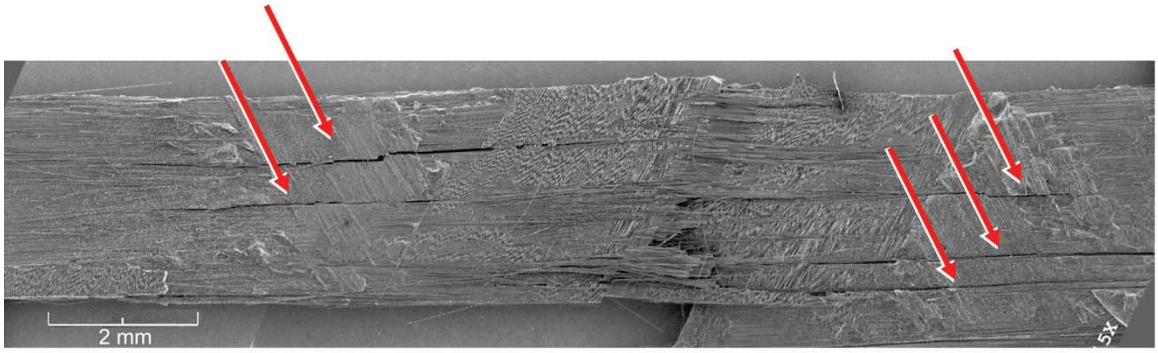

Figure 4.18.—Scanning electron microscope (SEM) picture of bias fiber bundle for T700/5208 fiber/resin material system (25× magnification) removed from failed region of tested axial specimen.

Figure 4.18 shows that in axial testing, the bias fiber bundles exhibited the splitting phenomena mentioned in the previous paragraph, as indicated by the arrows. These results confirm the observations obtained from the optical measurement system. The bias bundle splits are parallel to the direction of the fiber orientation. The strain data obtained from the optical measurement system at the locations of splits could be used for investigations of the fiber-matrix interface and local transverse failure strength (described in Sec. 5.0, "Development of Macromechanical Triaxial Braided Composite Computer Model"). Also note that the particular fiber bundle shown in Figure 4.18 was taken from the middle layer of the braid. This also confirms that even though the optical measurement system was only able to measure surface strains, the measured surface strain data was representative of all layers throughout the composite architecture.

The areas of high strain that occurred in the middle of the bias fiber bundle region developed from the load transfer between the subsurface axial and surface bias fiber bundle region consisting of fiber bundles and surrounding resin. As the subsurface axial fiber bundles underwent axial extension during testing, they also affected the surface bias fiber bundle region. The transfer of load between the subsurface axial

and surface bias fiber bundles occurred through the areas of resin material between the two fiber bundles, the fiber bundle-resin interface, and the interface between the resin and individual fibers that make up the fiber bundle. These areas of high strain are indicative of matrix cracking, which caused the surface bias fiber bundles to "split" and occurred when the strain was equal to the local ultimate transverse tensile strain of the area consisting of the bias fiber bundles and surrounding resin.

Another way to measure ultimate transverse strain of these regions around the fiber bundles is to examine the regions of high strain that occurred in a transverse tensile test, in which the axial fiber bundles were oriented perpendicular to the direction of the applied load. The high strains that develop in the region surrounding the axial fiber bundles represent a strain equal to the ultimate fiber bundle transverse tensile strain. Figure 4.19 shows an overlay of a transverse tension test.

Figure 4.19 shows the areas of high strain that developed on the subsurface axial fiber bundles (circled), which were visible between the surface bias fibers. The strain on the surface was assumed to be the same as the strain on the regions of the visible subsurface axial fiber bundles and surrounding resin. This assumption was verified by digital microscopic imaging.

Figure 4.20 shows a digital microscopic image of the side (edge) view of a transverse tensile specimen. The areas of dark grey represent the axial fibers, and the areas of white represent the bias fibers. The circled areas in Figure 4.20 show the fiber bundle splits that occurred in the axial fibers. The fiber bundle splits were present in not only the fibers captured by the optical measurement system, but also in the subsurface fibers. The digital microscopic picture confirmed the data seen by the optical measurement system that in transverse tensile tests the axial fiber splits were a major damage-causing mechanism.

Figure 4.21 shows an in-plane shear strain overlay on the gage section of a shear specimen. A uniform shear strain field was present in the middle of the gage section, which indicated that the local fiber bundle transverse "splits" or failures did not appear under shear loading. Instead, because of the loading direction, the specimen behaved homogeneously.

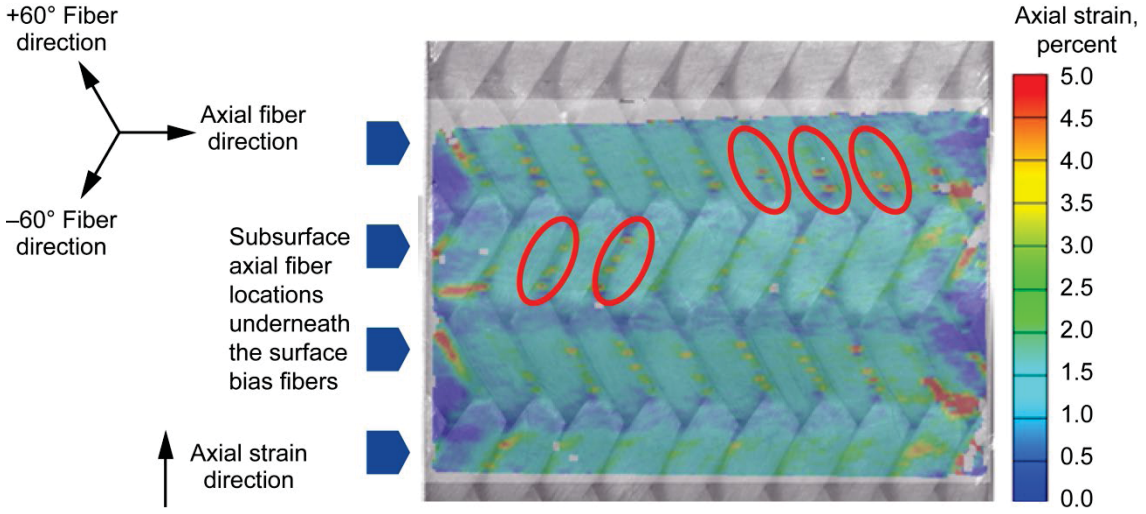

Figure 4.19.—Overlay of axial strain on representative T700/5208 fiber/resin transverse tension specimen.

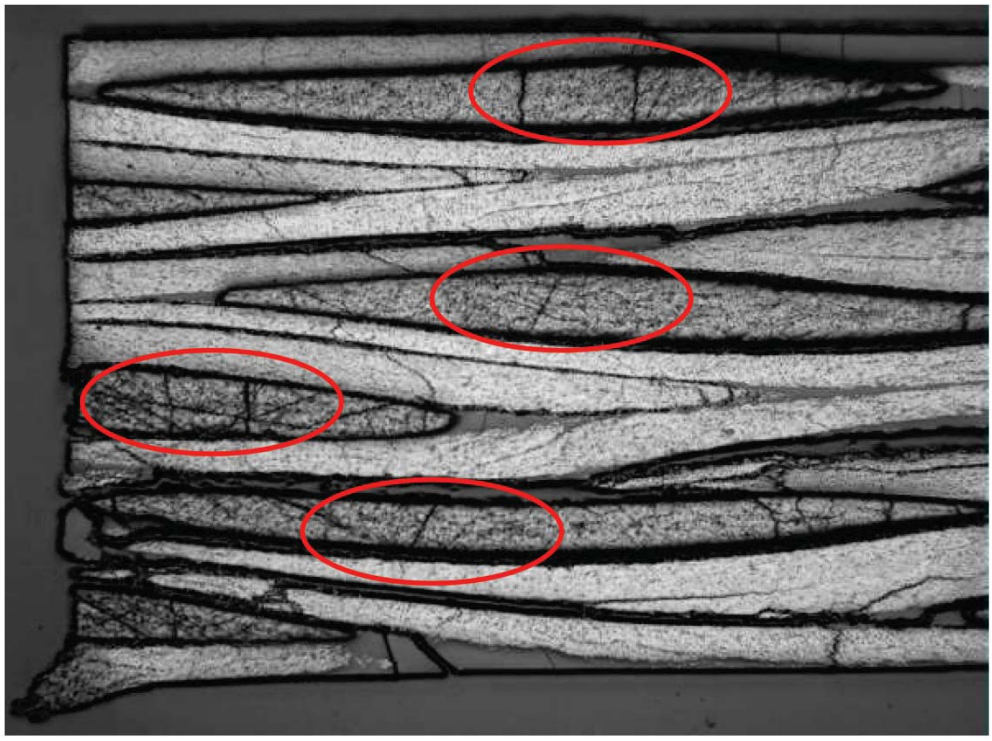

Figure 4.20.—Digital microscope picture of T700/5208 fiber/resin transverse tensile specimen.

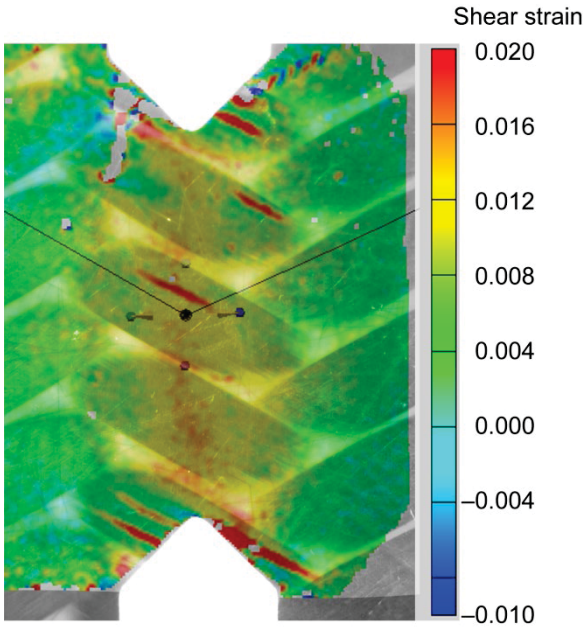

Figure 4.21.—Shear strain overlay on T700/5208 fiber/resin shear specimen.

The notched region in Figure 4.21 represents the gage section for the shear tests. A uniform area of approximately 0.012 shear strain developed in the gage section, which is represented in the yellow color in Figure 4.21, and a very small red area of slightly higher (approximately 0.016) shear strain developed between the gage sections notches. There are a few areas of strain concentrations represented by the diagonal red lines; however, these lines are not part of a regular repeating pattern and represent a local defect in the specimen. The main areas of high strain occur at the ends of the gage section represented by the red parallel diagonal lines show that there is slight cracking due to the notched edges. The area outside of the gage section (represented in green and blue) represent the gripped portion of the specimen. These outer areas saw little strain and confirmed that, in shear testing, the majority of the specimen deformation occurred in the middle of the notched gage section.

4.4.2.2 Examination of Transverse Fiber Bundle Failures

Section 4.4.2.1 shows the strain overlay techniques developed, which determined that there were areas of local fiber bundle failure. This section expands on the observations of transverse fiber bundle failures and how they related to the global material response. Specifically, the concept that the transverse fiber bundle failures initiated the damage propagation and progression in the composite coupon are elaborated in this section.

To reiterate the concept of the transverse fiber bundle splitting representing a transverse fiber bundle failure, Figure 4.22 shows the fiber bundle splits for the highest strength T700/PR520 material system that have developed in the transverse tensile specimen. The circled area in Figure 4.22 shows areas of high axial strain (in red) on the axial fibers orientated transversely to the loading in the picture, which are areas of high strain that represent matrix cracking. The matrix cracking caused the subsurface axial fiber bundles to split apart. With this knowledge, a random sampling of points on an example transverse tensile specimen was chosen for further examination.

Figure 4.23 demonstrates this principle by showing local strain results for four randomly picked points on the fiber bundle splits. Figure 4.23(a), shows the locations and labels of four example subsurface axial fiber bundle failures. Figure 4.23(b) shows the local strain at each of the individual chosen points plotted versus global composite stress for the specimen. A sudden increase in local strain at each chosen point without a significant increase in global specimen stress represents a fiber bundle failure (noted by the arrows on Fig. 4.23(b)). The value of the strain after the fiber bundle failure was examined carefully: the optical measurement system produced some erroneous results due to extreme distortions in

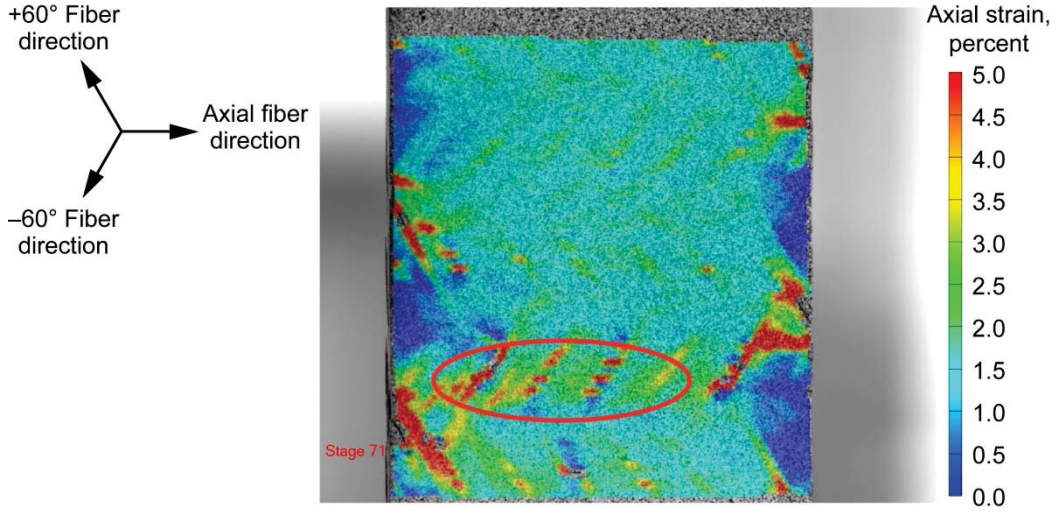

Figure 4.22.—Fiber splitting in T700/PR520 fiber/resin material system.

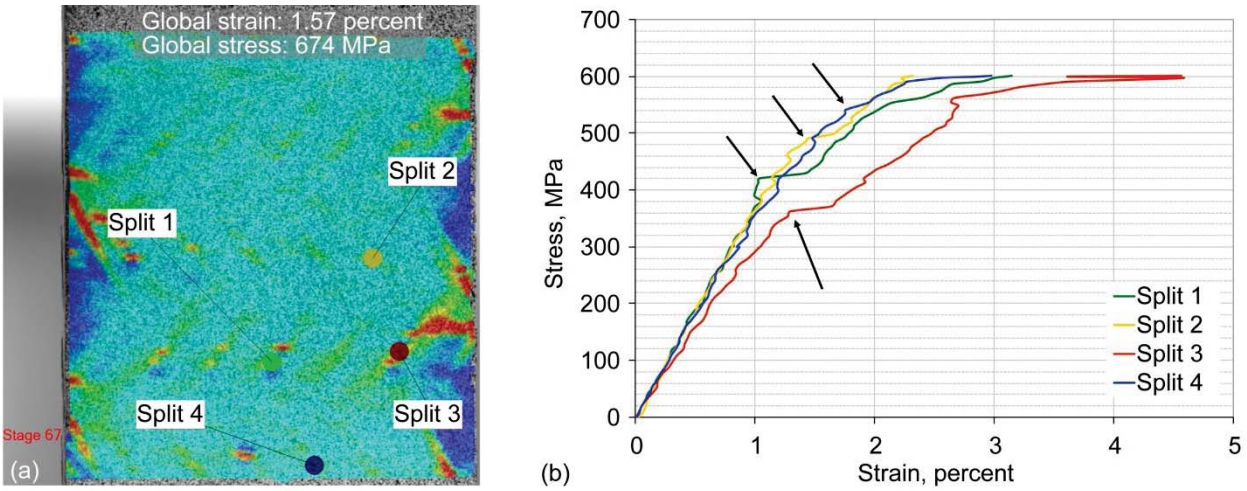

Figure 4.23.—Fiber bundle-matrix system splitting for T700/PR520 fiber/resin material system. (a) Subsurface axial fiber bundle failures. (b) Local strain at marked points in (a) versus global stress. Arrows denote fiber bundle failure.

the speckle pattern from the split at the chosen locations. Values of local strain or stress obtained after the split occurred were not used as material property information because of these extreme distortions in the speckle pattern. However, the value of the stress and strain immediately before the fiber failure was found and used as material parameters representing the effective transverse failure strain value of a fiber bundle and surrounding resin in a triaxial braided composite material. The mean value of strain at transverse failure was approximately 1.4 percent, with values ranging from 1.0 to 1.8 percent for the T700/PR520 material system.

The value of the global stress in which the first fiber bundle failed in Figure 4.23(b) was approximately 350 MPa. Comparing this value of stress to the global transverse tensile curve in Figure 4.6, one can note that 350 MPa was the approximate stress value in which the transverse tensile curve became nonlinear, suggesting that the transverse fiber bundle failures were causing the damage in the transverse tensile material response curves. Similarly, the same technique for examining the fiber bundle split locations was used on the low-strength T700/5208 material system and is shown in Figure 4.24.

The mean strain value for transverse fiber bundle failure in the T700/5208 system was approximately 0.5 percent, with values ranging from 0.4 to 0.7 percent strain (noted by the black arrows in Figure 4.24(b). The data show that transverse fiber bundle failure occurred at a lower strain in the T700/5208 system, leading to a lower ultimate failure strain than for the T700/PR520 system. These data also suggest that either the fiber-resin interface for the T700/5208 system was weaker than that of the T700/PR520 system or the ultimate strength of the resin was playing a major role in the material response.

The global composite stress at which the transverse fiber bundle failures started to occur was 150 MPa, which was a lower global stress value than for the T700/PR520 material system. Again, when comparing this global stress value to the transverse global material response curve in Figure 4.8, the data show that the global material behavior became nonlinear at approximately 150 MPa. These observations verify the data presented for T700/PR520, in that the transverse fiber failures were causing damage in the composite material systems.

Note that the values reported in Figures 4.23 and 4.24 are different than the composite transverse failure strain values reported in Table 4.4. The overall composite specimen failure is reported in Table 4.4, whereas the initiation of transverse fiber bundle failure, represented by the onset of fiber bundle splitting, is being reported in this section. By using the optical measurement system, the transverse failure of both the individual fiber bundles and the composite coupon were found. This led to an important conclusion about the composite material response in the transverse tests: In transverse tensile testing, the fiber bundles began

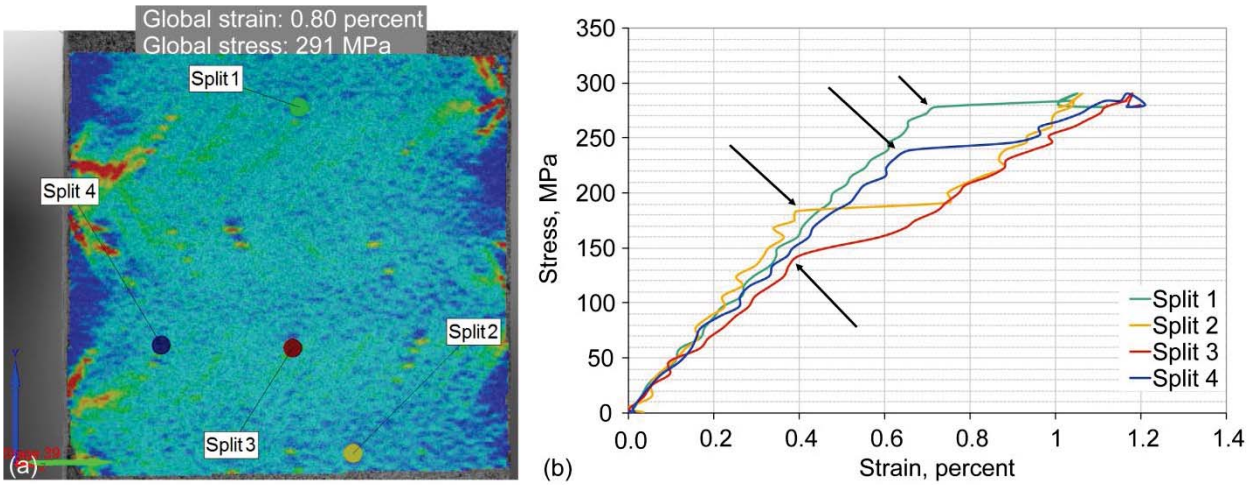

Figure 4.24.—Fiber bundle-matrix system splitting for T700/5208 fiber/resin material system. (a) Subsurface axial fiber bundle failures. (b) Local strain at marked points in (a) versus global stress. Arrows denote fiber bundle failure.

to split at the transverse fiber bundle failure strain, but the overall composite failed at the ultimate failure strain. Between the initiation of fiber bundle splitting and overall composite failure, the fiber bundle splits propagated throughout the composite, representing damage accumulation. Once the damage accumulation reached a critical value, the composite specimen then failed.

Also, Figures 4.22, 4.23(a), and 4.24(a), show that areas of low strain represented by dark blue sections developed along the free edges of the specimens. In the transverse specimens, this characteristic in the material response was common and occurred because the bias fibers terminated at the free edge of the transverse specimen. These areas of low strain were present because the bias fiber bundles at the edges of the specimens did not carry load from the test.

The full-field strain pictures and the transverse tensile data led to another important conclusion: For triaxial braided composite materials, standard coupon geometries may be inadequate for the determination of strength and elastic properties. For the quasi-isotropic assumption for the material properties of the composite to be valid, the strengths in both the axial and transverse direction should be equal. The data collected from this and the previous sections invalidated this assumption. The data show that strengths are 56 percent weaker for the T700s/PR520 fiber/resin system and 47 percent weaker for the T700s/5208 system in their transverse directions compared with their axial directions.

Alternative specimen designs have been proposed to eliminate the above deficiencies. One alternative specimen design that has been proposed is a “bowtie” or notched specimen geometry (Ref. 63), in which all of the axial and bias fibers located in the gage section could be gripped during the test. The other is a tubular specimen geometry, in which axial and bias fiber bundles extend along the entire specimen length and perimeter. Filament-wound tubular specimen geometries have been explored for obtaining shear properties by Foley, Roylance, and Houghton in Reference 64, but tubes containing the triaxial braid architecture have not been explored in detail.

The matrix cracking causing the fiber bundle splitting on the axial tensile specimens was examined next. Because of the differences in strength values between the strong T700/PR520 and weak T700/5208 material systems and the differences in the stress in which the fiber bundle splits begin to occur, the propagation of the fiber bundle splitting phenomenon was examined further through a series of time history snapshots. The three pictures for each system represented the specimen at a certain time during the history of loading. These three different points presented in Figure 4.25 represent (1) the onset of fiber bundle splitting, (2) the fiber bundle splitting that was occurring at a common stress value between the two material systems, and (3) the extent of fiber bundle splitting that occurred at the last data point collected before failure.

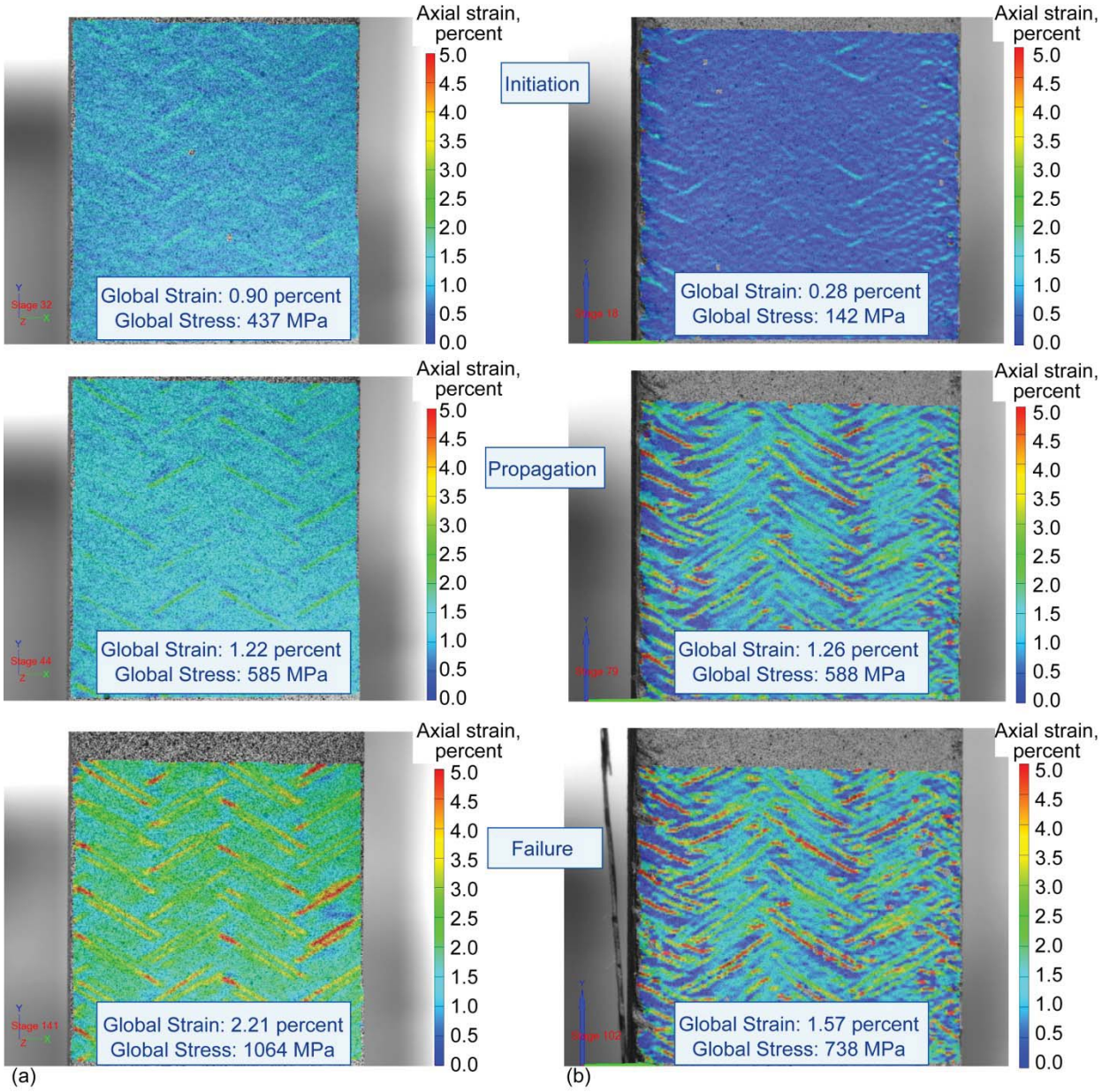

Figure 4.25 – Axial strain-time histories of fiber/resin material systems. (a) T700/PR520. (b) T700/5208.

For the T700/5208 material system, the onset of fiber bundle splitting occurred earlier during the test, which corresponded to a lower global stress value than for the T700/PR520 material system, and is represented by the top set of pictures in Figure 4.25. Also, the amount and extent of fiber bundle splits, as shown in the bottom set of pictures, was much greater in the weaker T700/5208 system. These two factors were also indications that the ultimate fiber-resin interface strength was lower in the T700/5208 material system than in the T700/PR520 system. The fiber-matrix interface was the main component holding the fibers to the matrix, indicating that the interface in the T700/5208 material system was weaker than that of the T700/PR520 system. The fiber bundles split apart earlier in the test and grew more abundant, giving rise to stress concentrations in the fiber bundles and ultimately weakening the composite. The results reported in Table 4.4 agree with these conclusions.

4.4.2.3 Examination of Subsurface Delaminations

In this section, the optical measurement system was used to examine and determine the extent of a different type of damage mechanism: subsurface fiber layer delaminations. To examine this type of damage mechanism, out-of-plane displacements were captured by the optical measurement system and examined in situ during testing. Note that to examine the areas of possible delaminations, the field of view from the optical measurement system was enlarged by reconfiguring the cameras and lenses to measure approximately 20 cm (8 in.) of the specimen height by the entire 3.579 cm (1.409 in.) of the specimen width. Any areas exhibiting large relative out-of-plane displacements coincided with areas of possible delamination. To verify delamination, results were compared with an ultrasonic through transmission (UTT) nondestructive evaluation (NDE) technique. Although UTT testing was not the scope of this work, a brief explanation of how UTT works will be presented to familiarize the reader with this NDE technique. A full explanation can be found in Reference 65.

For UTT an acoustic emitter was placed on one side of the specimen and a receiver was placed on the other side. The emitter then emitted a sound pulse, which was caught by the receiver. The transmitter-receiver system scanned the entire specimen, and the results of the scans were processed by a computer, showing the results as a full-field specimen visualization. The system was similar to the optical strain measurement system; the user can look at full-field postprocessed data. However, this technique differs such that the UTT must scan the specimen small areas at a time and cannot be done while the specimen is under loading. The UTT postprocessed data are also different because absolute measurements in the material response could not be made. Instead, relative degrees of the received signals are represented on a grayscale. A white color in the postprocessed visualizations indicates that the receiver captured the entire pulse emitted by the transmitter, meaning there were no subsurface defects in the material that scattered the transmitted wave. As more of the transmitted wave is scattered by passing through changes in local fiber architecture or local subsurface damage such as fiber delamination, the darker the postprocessed UTT images become. A black area in the UTT postprocessed data indicates that very little of the emitted sound wave was actually collected by the receiver.

The two material systems that were used to examine possible subsurface layer delaminations were a stronger material system, T700/E862, and a weaker material system, T700/3502. Four specimens from each material system were tested in both their axial and transverse directions. Each of the four specimens was tested to a different value of loading: 25, 50, 75, and 90 percent of its ultimate strength as determined from Section 4.4.1.1. Testing was conducted by loading the specimen at 0.635 mm/min (0.025 in./min) while taking pictures at specified intervals between 2 and 6 s, depending on the value of ultimate loading. Once the end value of load was reached, the loading was held constant, and a final loaded picture was taken by the optical measurement system. Finally, the specimen was unloaded, and a final unloaded picture was taken to compare with the pretest specimen data.

4.4.2.3.1 Subsurface Delaminations in the Axial Direction

The T700/E862 material system's axial tensile specimens were examined first. The UTT and out-of-plane optical measurements were taken before the test to establish baseline conditions, with which posttest results could be compared. Baseline conditions using the optical measurement system were established by gripping and taking a picture of an unloaded specimen, then computing the out-of-plane displacements. These baseline pictures also established the relative grip misalignment in the test machine.

Figure 4.26 shows the baseline results from the optical measurement system. Here, the baseline measurements made by the optical measurement system indicate that the specimens that were used for the 25-, 75-, and 90-percent ultimate strength tests exhibit a uniform field of very small out-of-plane displacements, with the exception of their bottom right corners. This small region of high displacement was due to the grip misalignment in the machine and was accounted for when examining the posttest results. The 50-percent specimen shows areas of high out-of-plane displacement near the top and low out-of-plane displacement near the bottom. This anomaly was due to a grip misalignment in the test fixture and was accounted for when examining the posttest results. To establish the UTT baseline conditions, specimens were scanned in an unloaded state before the test.

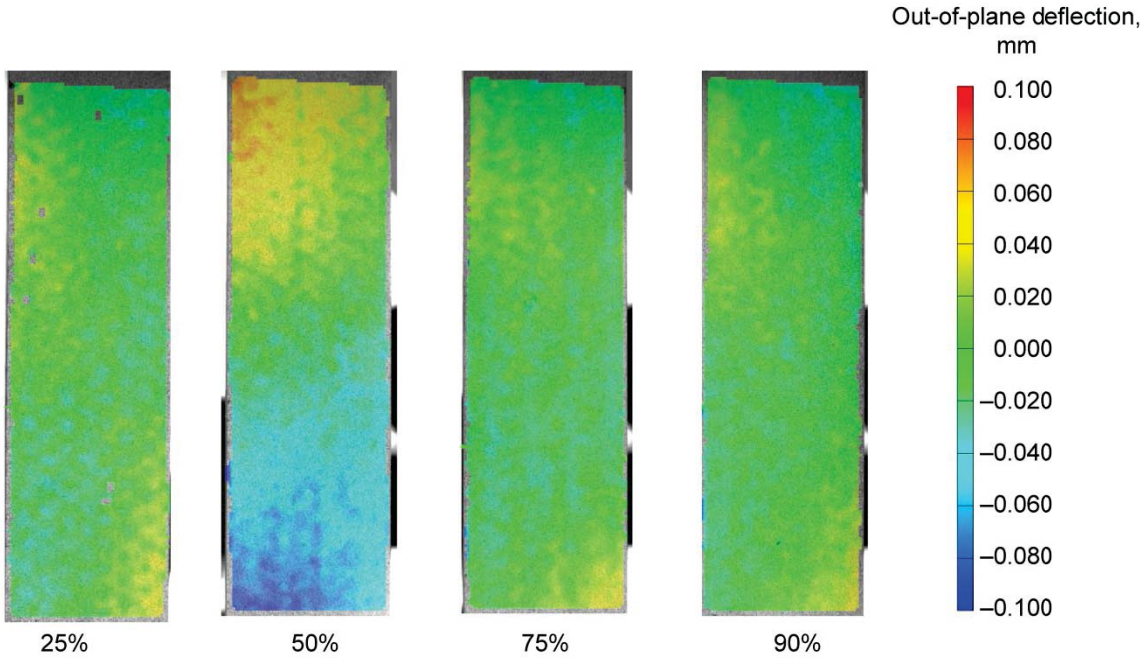

Figure 4.26.—Baseline displacements for T700/E862 fiber/resin specimens at 25, 50, 75, and 90 percent of ultimate strength for axial direction.

Figure 4.27 shows that the baseline scans made by the UTT system captured repeating patterns of white and dark areas in the specimen. These areas represent different locations within the fiber braid. The dark areas indicate areas where the bias fiber bundles met, and the white areas represent areas where the axial fibers are present. The braid architecture can also be seen by noting that the alternating white and dark parallel lines running in the –60° and +60° directions represented the bias fiber bundles present in the specimens.

After the baseline conditions were established, the test was run and the posttest results were examined. Figure 4.28 shows the out-of-plane displacement results gathered from the optical measurement system at the final load for the axial tests conducted for the T700/E862 material system, and Figure 4.29 shows the UTT results. Figure 4.28 shows the four axial tests conducted on the T700/E862 material system, and Figure 4.29 shows the UTT scans of the same specimens. The optical measurement data in Figure 4.28 are shown at the point of maximum load. Ultrasonic through transmission pictures are shown in a posttest unloaded state. By comparing Figures 4.28 and 4.29, one can see that similarities exist between the results from the optical measurement system and UTT. First, by looking at the baseline optical measurement data and UTT scans for the specimens loaded to 25 and 50 percent, the posttest results show identical images to the baseline results, indicating that there were variations that were normally present in the composite. Also note that the anomaly present in the 50 percent specimen during the baseline optical measurements was accounted for and was not present in the postprocessed results. However, when the 75 and 90 percent specimen results were examined, major differences between the posttest and baseline results became evident. Figure 4.30 shows comparisons of the UTT and optical measurement data for the 75 and 90 percent specimens.

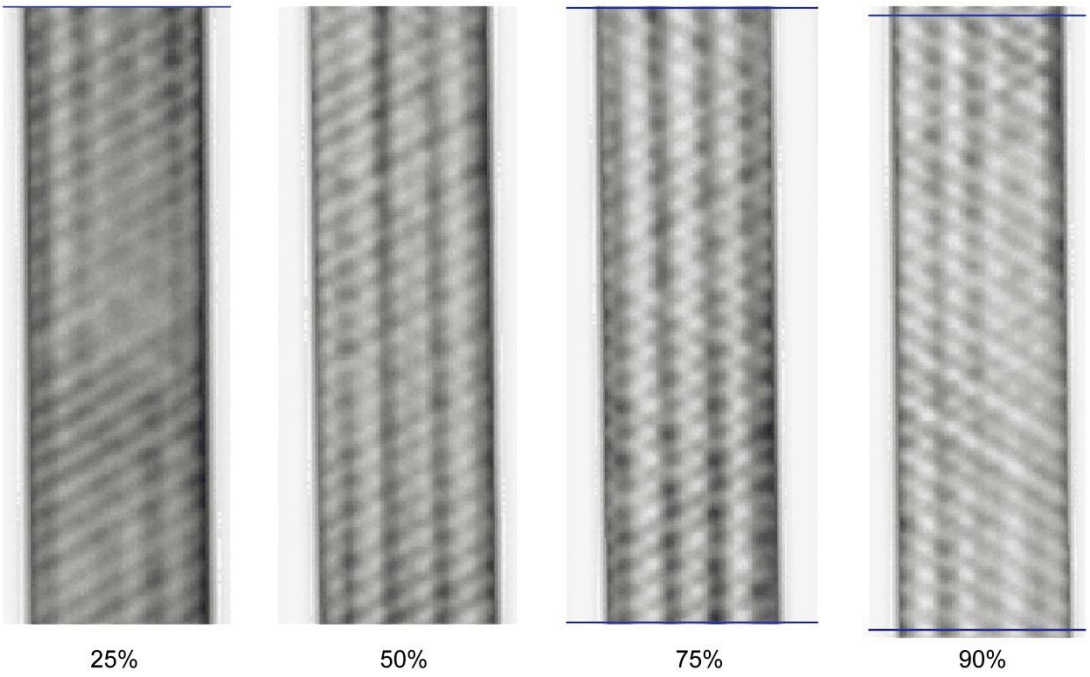

Figure 4.27.—Ultrasonic through transmission (UTT) baseline scans for T700/E862 fiber/resin specimens at 25, 50, 75, and 90 percent of ultimate strength in axial direction.

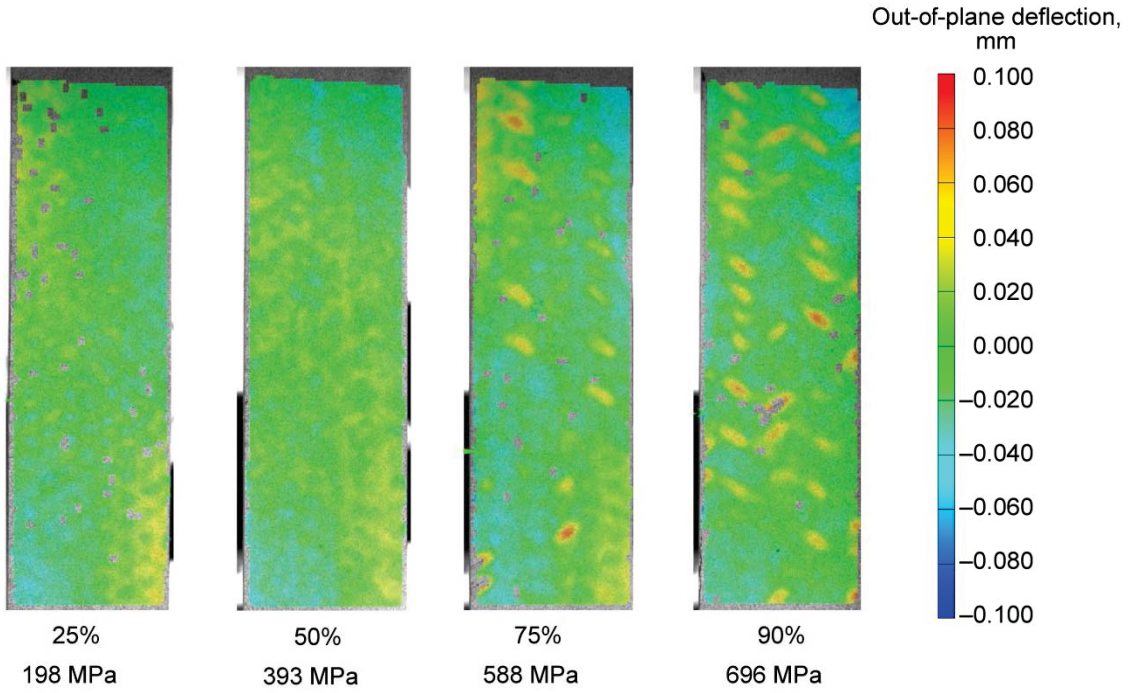

Figure 4.28.—Out-of-plane displacements from axial tests of T700/E862 fiber/resin specimens loaded to stress values shown, corresponding to 25, 50, 75, and 90 percent of ultimate strength.

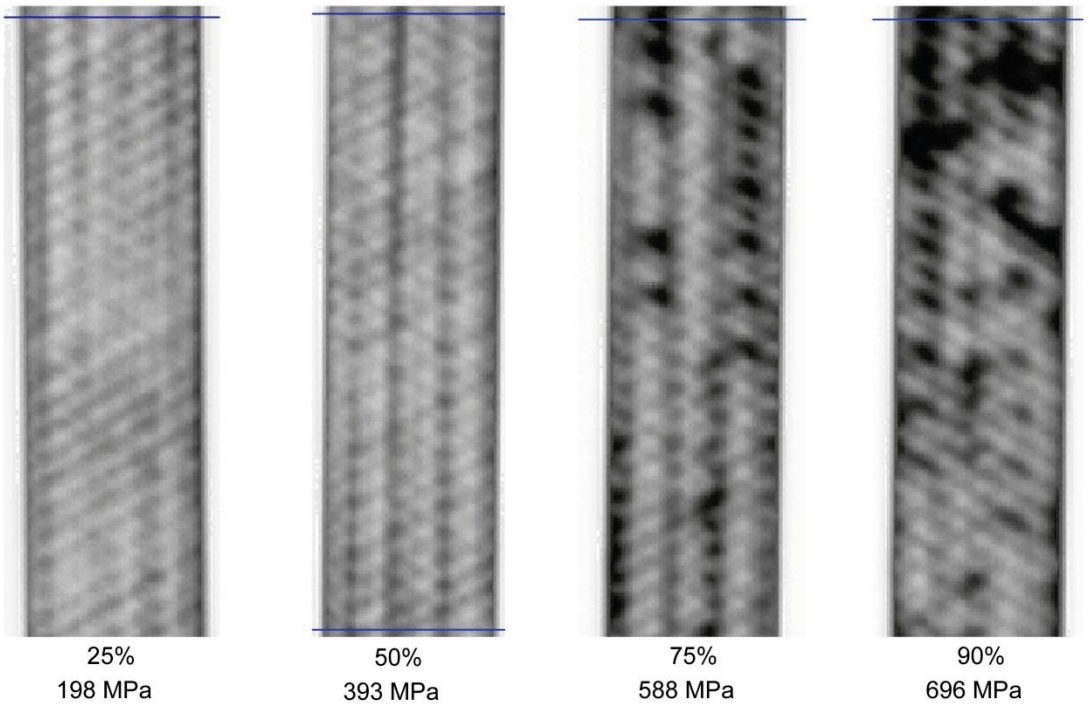

Figure 4.29.—Ultrasonic through transmission (UTT) scans from axial tests of T700/E862 fiber/resin specimens loaded to stress values shown, corresponding to 25, 50, 75, and 90 percent of ultimate strength.

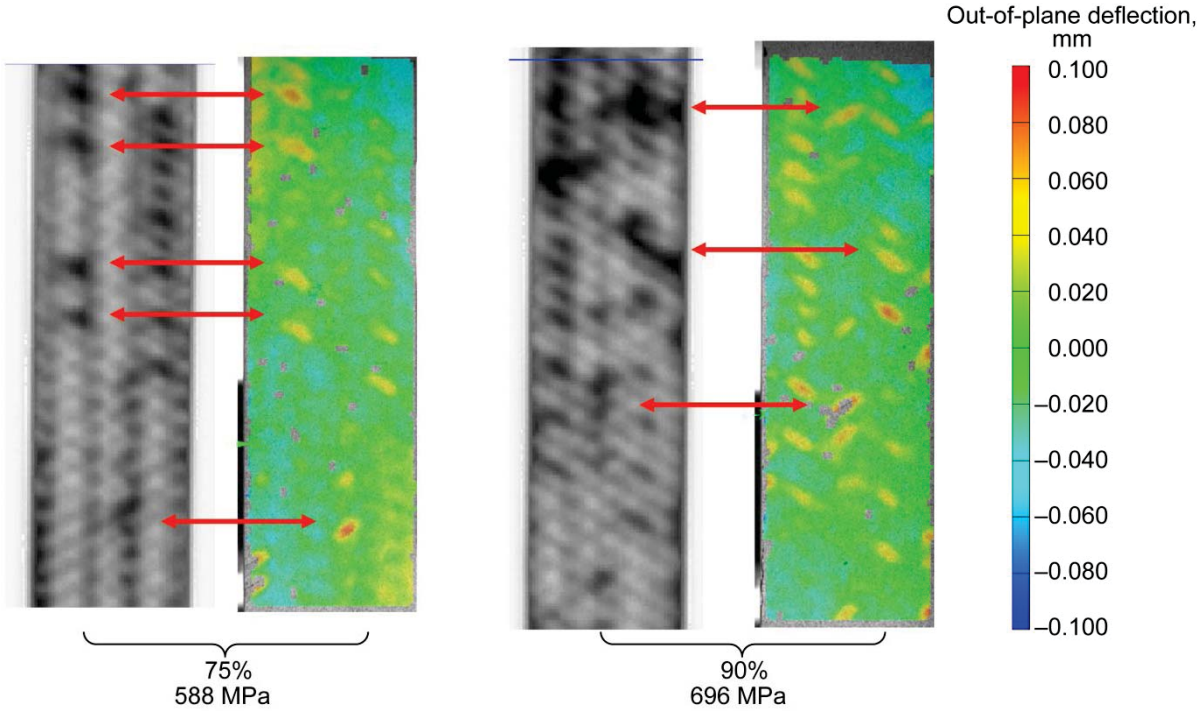

Figure 4.30.—Comparison of ultrasonic through transmission (UTT) and optical measurements from axial tests of T700/E862 fiber/resin specimens loaded to stress values shown, corresponding to 75 and 90 percent of ultimate strength.

When the material system was tested at 75 percent of ultimate loading, the optical measurement's out-of-plane data show areas of high out-of-plane deformation surrounded by regions exhibiting behavior similar to the baseline data, indicating a local delamination. Figure 4.30 also shows that strong correlations exist between the optical measurement system and the UTT NDE techniques for the specimen loaded to 75 percent of its ultimate load. This conclusion is important because it shows that in future testing, delaminations causing damage in the composite materials can be captured by examining the out-of-plane deflection obtained from the optical measurement system, without having to conduct an extra NDE test. The results from the specimen loaded to 90 percent of ultimate load verify these results. Out-of-plane deformation occurred on the highest loaded specimens, which indicates that delamination occurred at higher loadings.

To verify that the subsurface delaminations were present, regions of high out-of-plane deformation were cut from the specimens and examined under a digital microscope. Figure 4.31 shows the location of the section that was examined in the axial T700/E862 material system loaded to 90 percent of ultimate load. The optical measurement and UTT data showed that the specimen had a possible delamination in the middle of the section. Figure 4.32 shows a digital microscopic image of the section described in Figure 4.31.

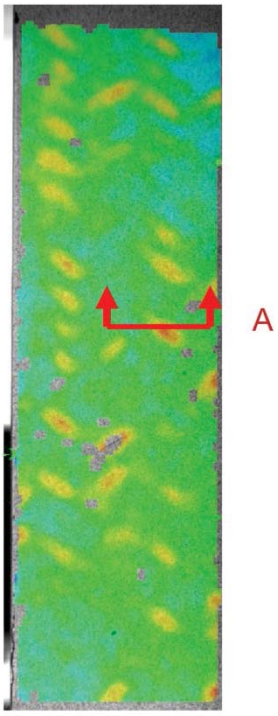

Figure 4.31.—Section location from T700/E862 fiber/resin material system loaded to 90 percent of ultimate strength in axial tests that was used for digital microscopic imaging (Fig. 4.32).

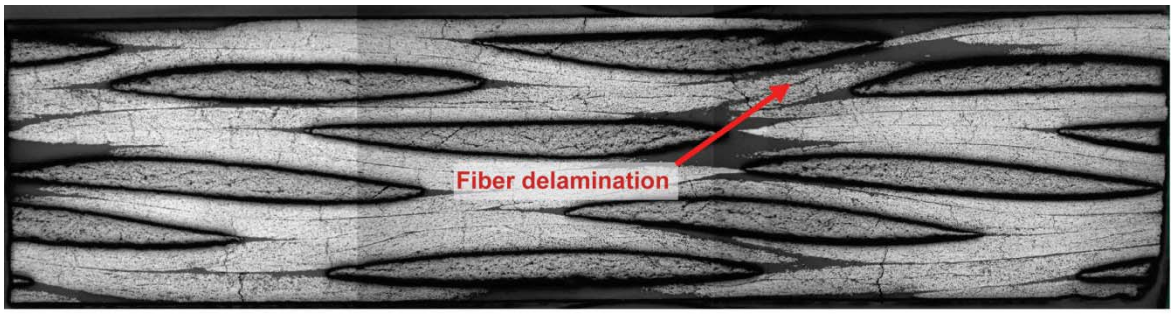

Figure 4.32.—Digital microscopic image of section (see Fig. 4.31) of T700/E862 fiber/resin specimen in axial tension loaded to 90 percent of ultimate load in axial tests.

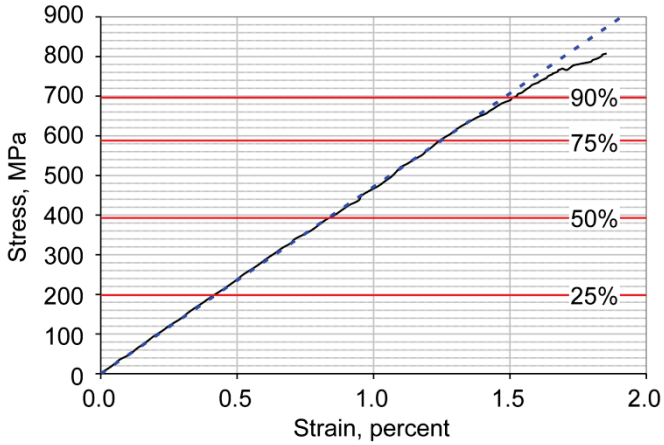

Figure 4.33.—T700/E862 fiber/resin stress-strain response curve from axial tests, noting stress levels at 25, 50, 75, and 90 percent of ultimate strength.

Figure 4.32 highlights the area shown to have a possible delamination as identified by both the optical measurement system and UTT technique. The axial fibers, which were orientated out of the plane of the picture, are shown in dark grey and the bias fibers are shown in light grey. The large black areas surrounding the axial fibers are the edges of the axial fibers. The indicated area in Figure 4.30 corresponds to the area of a possible delamination as seen by the optical measurement system and the UTT. The indicated area in Figure 4.32 shows damage in the subsurface bias fiber, which was caused by the surface axial fiber as pulled away from a subsurface bias fiber in its lower right corner. This was the out-of-plane deformation picked up by the optical measurement system and UTT.

Figure 4.33 shows where the 25, 50, 75, and 90 percent loading points occurred on the global stress-strain material response curve for T700/E862. The black curve depicts a typical axial material response. The four stress levels are marked with a red line. Finally, a perfectly linear material having the same modulus as T700/E862 is marked with the dotted blue line. The material response curve starts to behave in a nonlinear fashion at approximately 75 percent, or more specifically, where the subsurface delaminations begin to appear and are captured by the optical measurement system and UTT. Below the 75 percent stress level, the curve behaves in a linear manner, which corresponds with the lack of damage as seen by the UTT and the optical measurement systems. The conclusion garnered from this data supports the theory that the subsurface delaminations are damage mechanisms that occur in the axial direction, causing the stress-strain curve to become nonlinear.

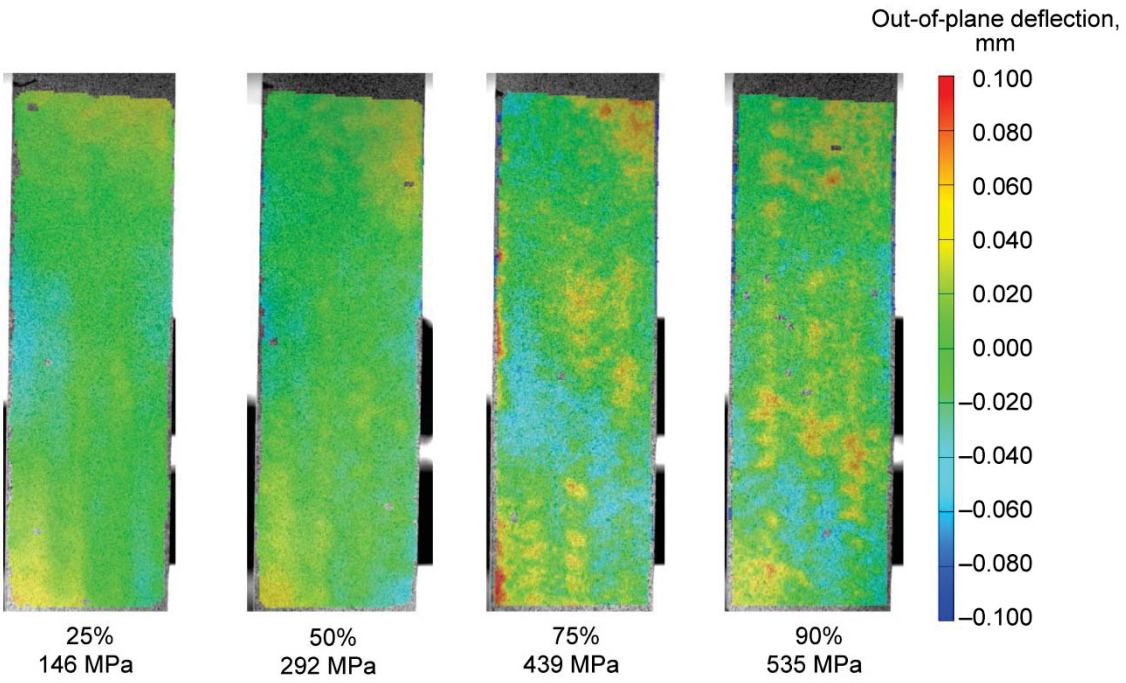

Figure 4.34.—Out-of-plane displacements from axial tests of T700/3502 fiber/resin specimens loaded to stress values shown, corresponding to 25, 50, 75, and 90 percent of ultimate strength.

Next, the same procedure was repeated on the weaker T700/3502 material system's axial test specimens. Baseline pictures from the optical measurement system and pretest scans from the UTT were taken. As before, the specimens were loaded to 25, 50, 75, and 90 percent of ultimate strength as determined by the material response curves presented in Section 4.4.1.1 and then unloaded.

The baseline optical measurement system pictures confirmed that the untested specimen shows very little displacement, and the baseline UTT scans show similar results to Figure 4.27: repeating patterns in the braid architecture were found, with no anomalies present. Therefore, the tests were run and the posttest results are presented. Figure 4.34 shows the out-of-plane displacement results from the optical measurement system at maximum load.

The T700/3502 material system starts to show a small amount of out-of-plane displacements when the specimen was loaded to 50 percent of ultimate strength. The specimen shows pronounced out-of-plane displacements at 75 and 90 percent of its ultimate load. Again, to verify these conclusions, the specimens were also scanned with the UTT.

Figure 4.35 shows the results of the UTT scans. At 25 percent of ultimate load, the scans only show the normal variation in braid pattern. However, slight amounts of dark areas appear at the bottom of the specimen loaded to 50 percent of ultimate load. At 75 and 90 percent, large dark areas were clearly present, indicating delaminations. Figure 4.36 shows the comparisons of the optical measurement's out-of-plane deformation and the UTT scans. The optical measurement's out-of-plane deflection results show good agreement with that from the UTT. As with the T700/E862 material system, T700/3502 was examined with digital microscopic imaging.

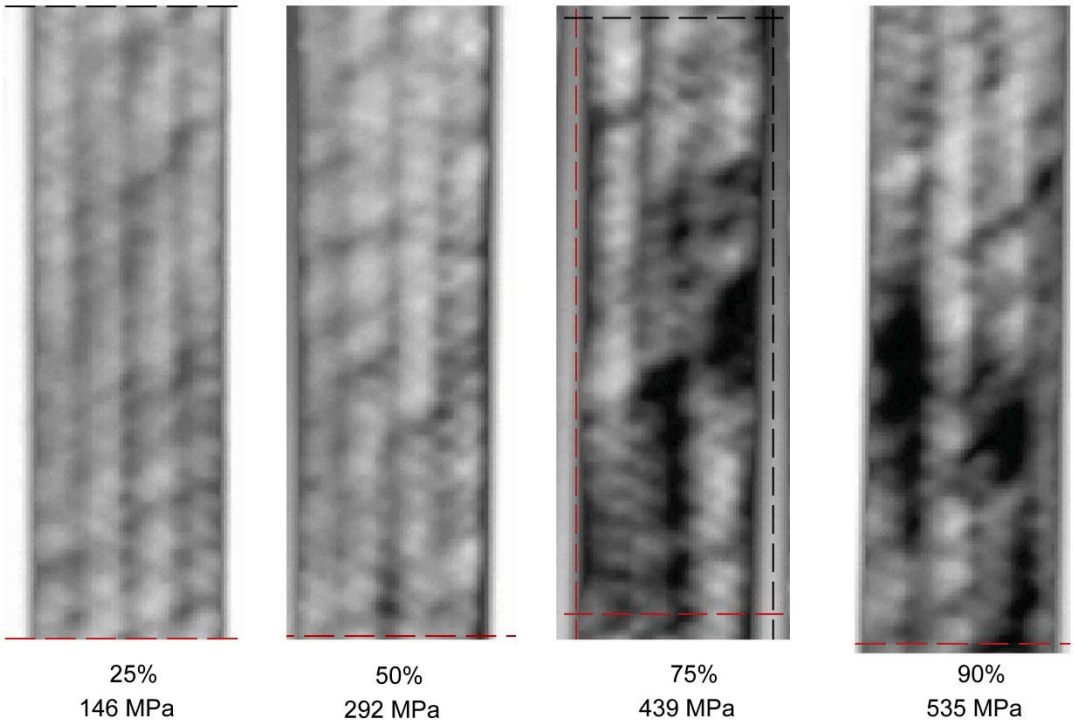

Figure 4.35.—Ultrasonic through transmission (UTT) scans from axial tests of T700/3502 fiber/resin specimens loaded to stress values shown, corresponding to 25, 50, 75, and 90 percent of ultimate strength.

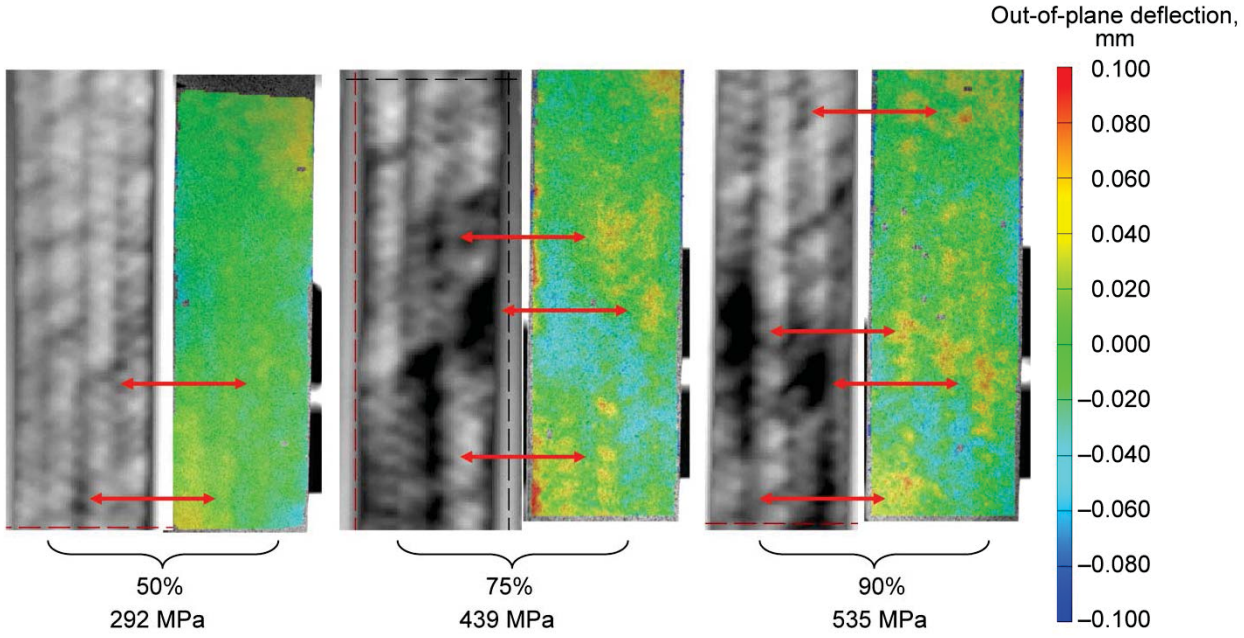

Figure 4.36.—Comparisons of ultrasonic through transmission (UTT) and optical measurements from axial tests of T700/3502 fiber/resin specimens loaded to stress values shown, corresponding to 50, 75, and 90 percent of ultimate strength.

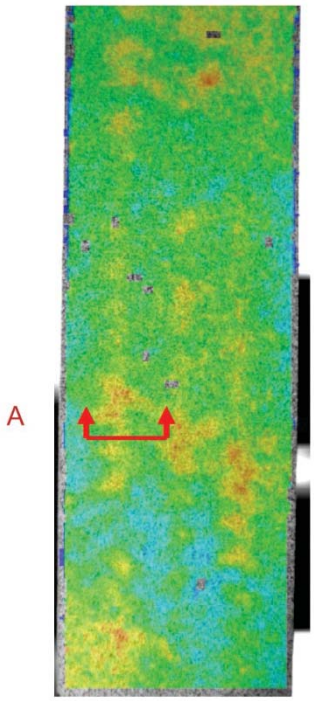

Figure 4.37.—Section location from T700/3502 fiber/resin material system loaded to 90 percent of ultimate strength in axial tests that was used for digital microscopic imaging (Fig. 4.38).

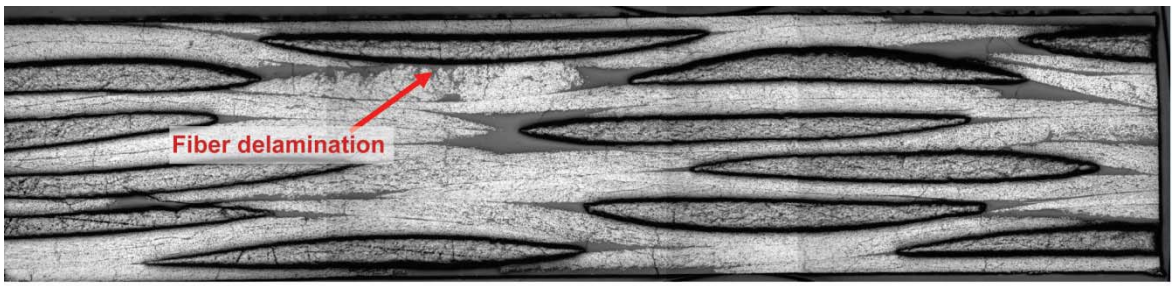

Figure 4.38.—Digital microscopic image of section (see Fig. 4.37) of T700/3502 fiber/resin axial tension specimen loaded to 90 percent of ultimate load.

Figure 4.37 shows the section from the 90 percent specimen used for digital microscopic imaging. The optical measurement and UTT data show that the specimen had a possible delamination in the middle of the section. Figure 4.38 shows the digital microscopic image of the section cut from the specimen. The dark grey areas represent the axial fibers, which are orientated out of the plane of the picture, and the light grey areas are the bias fibers. The dark outlines around the axial fiber represent the edge of the fibers. The indicated area is an area that corresponds to a possible delamination, as observed by the optical measurement system and the UTT. Figure 4.38 shows damage to the subsurface bias fiber directly underneath the axial fiber as well as a small gap between the two. This gap is the data point picked up by the optical measurement system and the UTT.

However, the digital microscopic imaging pictures are not as conclusive as either the optical measurement or UTT data. There are two possibilities for this discrepancy: The first possibility is that since the delaminations are very localized in the braid architecture, the sections cut from the specimen

might not have captured the spot of maximum delamination but rather were cut in an area slightly away from the delamination, which only captured the propagation. The second possibility is that the area in question became unusable in the process of cutting and preparing the areas where possible delaminations occurred from the composite. By cutting the specimen, the delaminated fiber bundle could have been able to "relax," or set back into its original position in the braid architecture, closing the gap seen by the optical measurement system and UTT. Because of these reasons, digital microscopic imaging was used only as a third check on the data. In many cases, when trying to observe nonvisible damage in tested material systems, UTT techniques are accepted methods of detecting subsurface damage occurring in materials and have been widely reported. Thus, the correlations between the UTT and optical measurement system provide a way to measure and detect subsurface delaminations leading to damage accumulation in the composite specimens.

As with the stronger T700/E862 material system, Figure 4.39 shows the material response curve for the T700/3502 material system in the axial direction with four stress levels are marked by a red line. A theoretical material having a perfectly linear modulus the same as T700/3502 is added as a dotted blue line for reference. The figure shows that the nonlinearities in the material response starts to occur around 50 percent ultimate load, which corresponds to the first detectable subsurface delamination damage. Beyond this region, the delaminations are clearly present in the material, leading to the conclusion that in the axial tensile direction, the subsurface delaminations were damage mechanisms occurring in the axial direction that caused the nonlinearities in the global material response curves.

Using the data gathered in this section along with that gathered in Section 4.4.2.2 and the global material response curves in Section 4.4.1.1, an understanding of the composite response in the axial direction can be described: Under loading, the axial fibers in the composite specimens are the main load-carrying mechanisms. The fiber-matrix interface dictates when the surface bias fiber bundle splitting begins to occur, which is a good indication of the interface strength; however, the nonlinearities in the global material response curves begin to appear once the subsurface delaminations appear. The composite coupon's ultimate failure is dependent on the fiber-matrix interface: the interface influenced the ultimate failure strain of the axial fiber bundles. A stronger interface causes a clean fiber-matrix separation and allows for the fibers to reach their ultimate failure strain, as shown with the T700/PR520 material system. A weaker interface allows for the matrix to degrade the fiber ultimate strength by bringing concentrations to the fiber bundles, while also allowing for fiber layer delaminations to occur more frequently and at earlier stages in the loading.

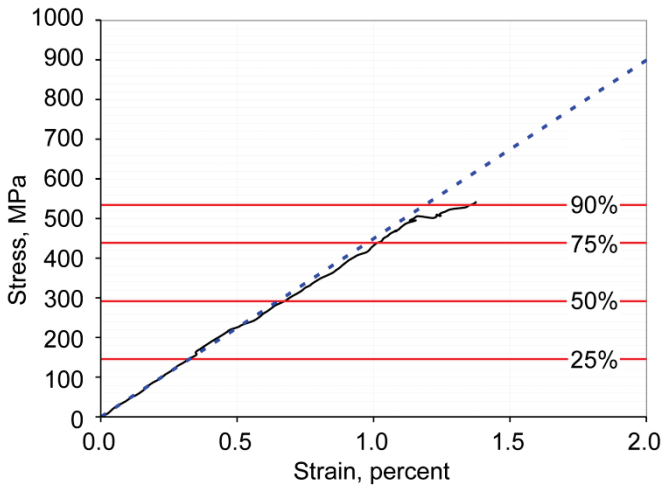

Figure 4.39.—T700/3502 fiber/resin stress-strain response curve from axial tests, noting stress levels at 25. 50, 75, and 90 percent of ultimate strength.

4.4.2.3.2 Subsurface Delaminations in the Transverse Direction

Recall that in transverse tensile testing, the axial (0°) fibers did not extend throughout the gage section, but rather were oriented perpendicular to the direction of loading. As pointed out in the previous section, the transverse fiber bundle failures in the axial fibers were one of the causes of the nonlinearities occurring in the global stress vs. strain material response curve. However, out-of-plane displacements were also examined to determine whether subsurface delaminations played a role in the material response.

Testing was done in the same fashion as the axial testing: four different specimens were loaded to four different loading levels, 25, 50, 75, and 90 percent of ultimate strength, as determined by the overall material response testing presented in Section 4.4.1.1. To start, baseline UTT scans and optical measurement pictures were taken for posttest comparisons.

Figure 4.40 shows the baseline optical measurement system out-of-plane displacements for the T700/E862 material system and indicates that the specimens exhibit a uniform field of very small out-of-plane displacements, with the exception of their bottom right corners. As with the axial tests, this small region of high displacement was due to the grip misalignment in the machine and accounted for when examining the posttest results. Again, as with the axial test, the UTT baseline conditions were established by scanning the specimens in an unloaded state before the test.

Figure 4.41 shows that the baseline scans made by the UTT system again captured white and dark areas in the specimen. These areas represent different locations within the fiber braid. Again, the dark areas indicate areas where the bias fiber bundles met, and the white areas represent areas where the axial fibers are present. The braid architecture can also be seen, by noting that the alternating white and dark parallel lines running in the –30° and +30° directions represent the bias fiber bundles present in the specimens, which in the transverse test, run 60° to the horizontal axis. Also the areas of parallel black and white lines running in the horizontal direction represent the axial fiber bundles. After the baseline conditions were established, the test was run and the posttest results were examined.

Figure 4.42 shows that the high localized areas of out-of-plane deformation seen in the axial tests are not present in the transverse testing, even at the highest loaded conditions. The majority of the results show a uniform field of little displacement, with slightly higher areas around the bottom right corner of the specimens. This slightly higher area of displacement was due to the slight grip misalignment present in the machine. To verify the results seen by the optical measurement system, the specimens were scanned with the UTT.

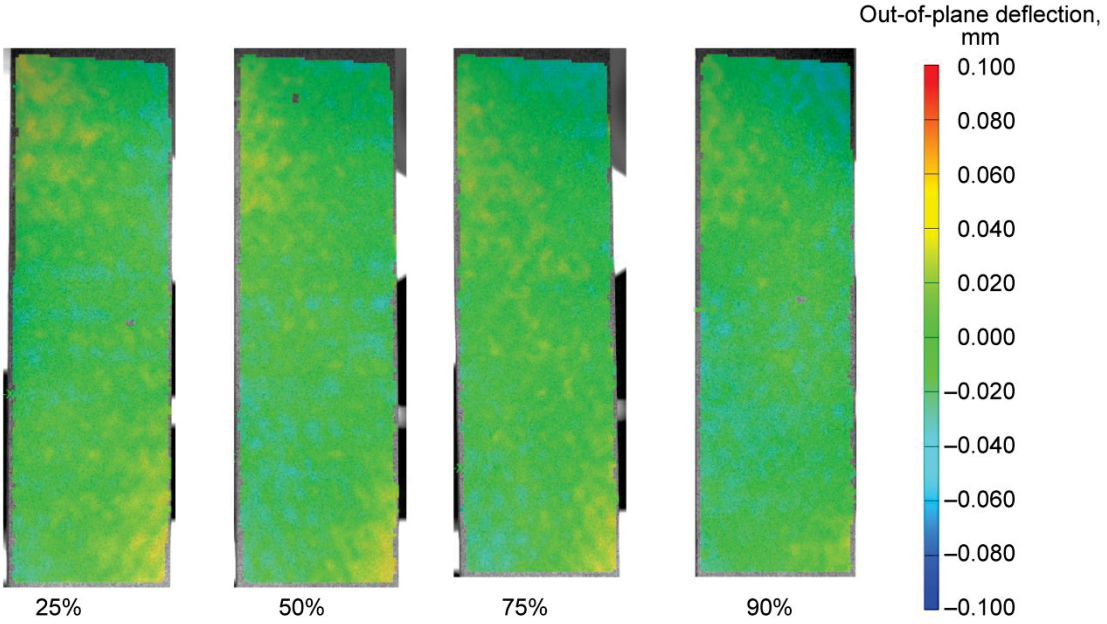

Figure 4.40.—Baseline displacements for T700/E682 fiber/resin specimens at 25, 50, 75, and 90 percent of ultimate strength in transverse direction.

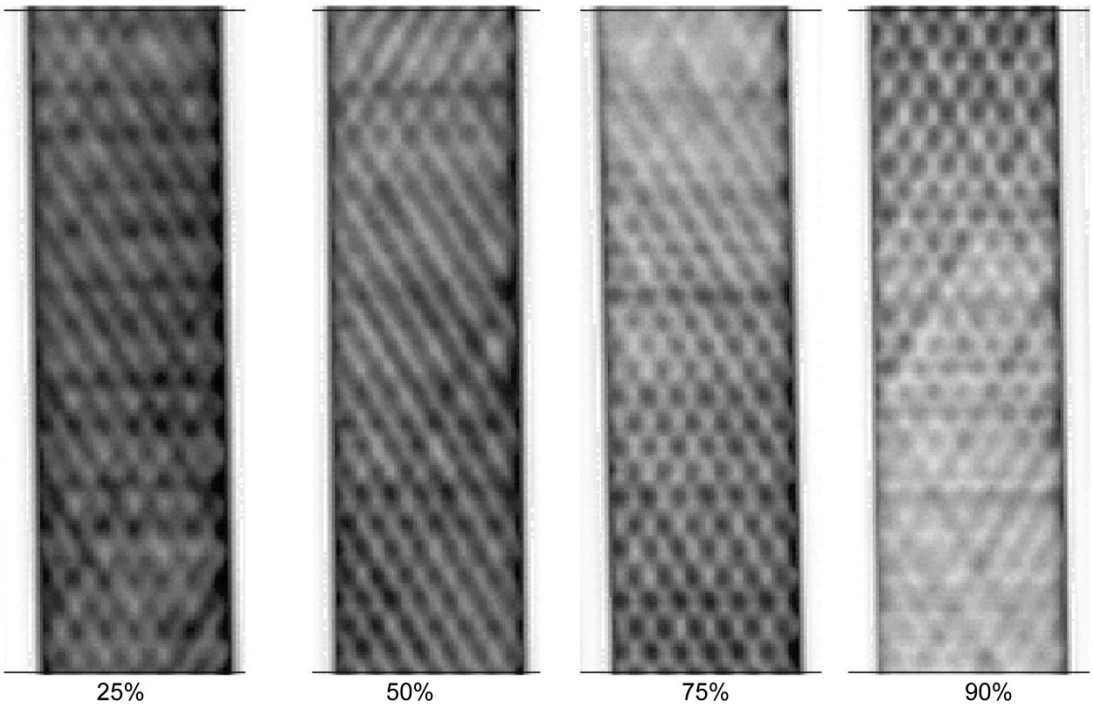

Figure 4.41.—Ultrasonic through transmission (UTT) baseline scans for T700/E862 fiber/resin specimens at 25, 50, 75, and 90 percent of ultimate strength in transverse direction.

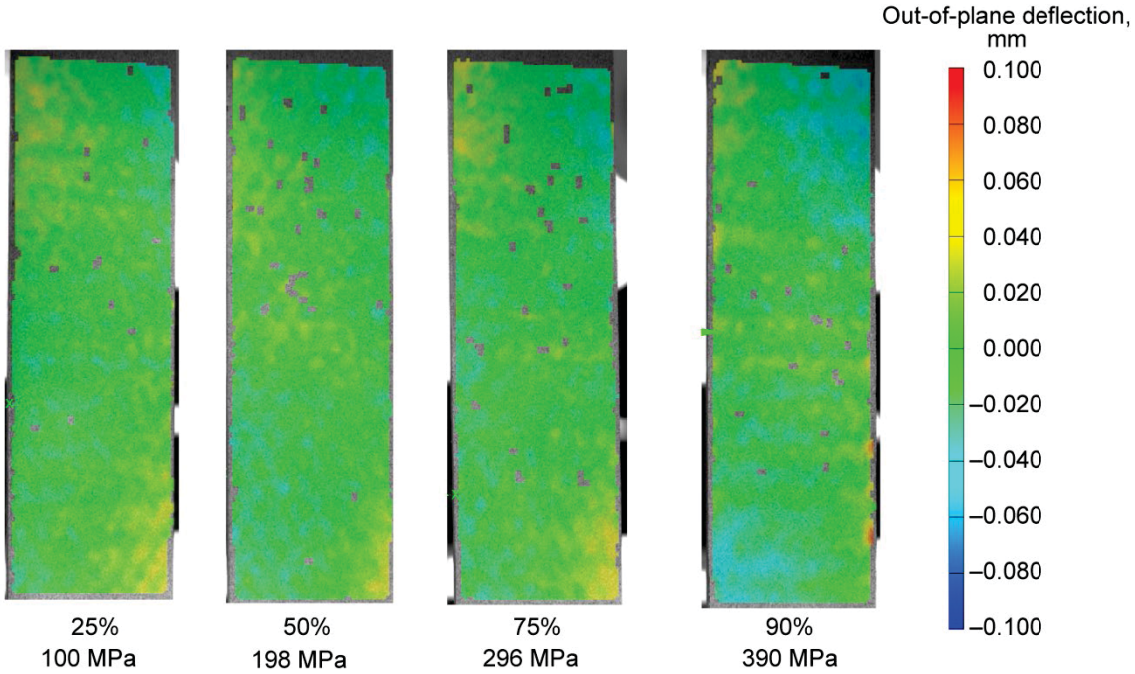

Figure 4.42.—Out-of-plane displacements from transverse tests of T700/E862 fiber/resin specimens loaded to stress values shown, corresponding to 25, 50, 75, and 90 percent of ultimate strength.

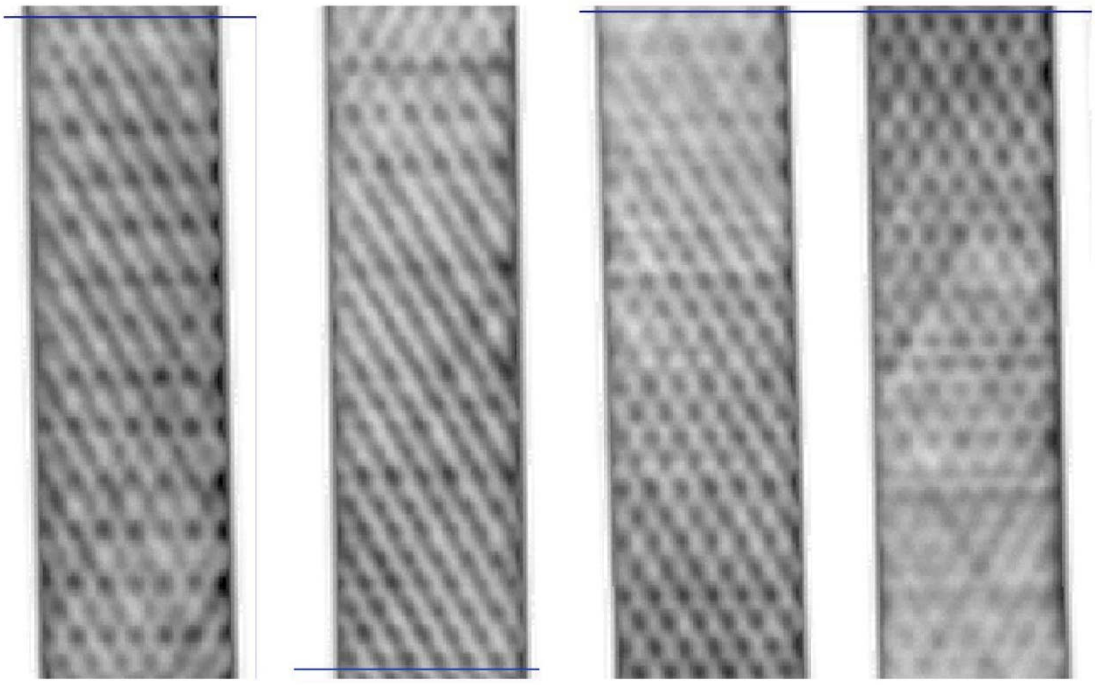

Figure 4.43.—Ultrasonic through transmission (UTT) scans from transverse tests of T700/E862 fiber/resin specimens loaded to stress values shown, corresponding to 25, 50, 75, and 90 percent of ultimate strength.

The UTT scans (Fig. 4.43) confirmed the results seen by the optical measurement system. The UTT scans completed on the tested transverse specimens show only patterns normally present, created by the braid architecture. This led to the conclusion that delaminations did not occur and did not influence the material response in the transverse tensile composite coupon as they did with the axial tension specimens.

For completeness, the T700/3502 material system was also tested. Figure 4.44 shows the results from these four tests.

Figure 4.44 shows that for specimens at 25, 50, and 75 percent loading, the results agree with the T700/E862 results. The 90-percent specimen however, showed results that indicated possible delaminations. As with all of the testing done in this section, the specimens labeled 90 percent were loaded to a nominal 90-percent ultimate stress level as determined by an average from the specimens tested for the generation of material response curves in Section 4.4.1.1. However, the specimen tested in Figure 4.44 began to fail before 90 percent of the average ultimate strength was reached, representing the low end of the standard deviation of the data. The 90-percent picture in Figure 4.44 shows the specimen at the onset of ultimate failure, more likely at 99 percent of its ultimate strength. Had this specimen been loaded higher than 279 MPa (40 470 psi), the specimen would have failed completely, leaving both the optical measurement and UTT results unusable. Thus, the test was stopped at the initial onset of ultimate failure, which is being shown in Figure 4.44. Again, these results were verified with UTT scans, as shown in Figure 4.45.

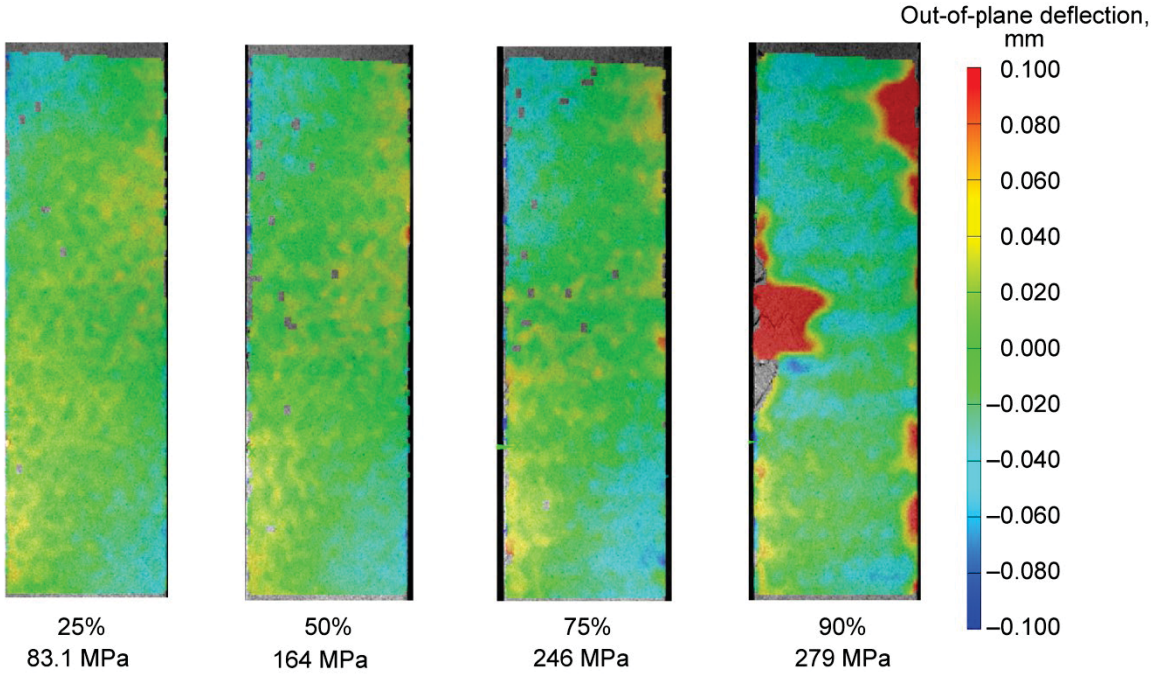

Figure 4.44.—Out-of-plane displacements from transverse tests of T700/3502 fiber/resin specimens loaded to stress values shown, corresponding to 25, 50, 75, and 90 percent of ultimate strength.

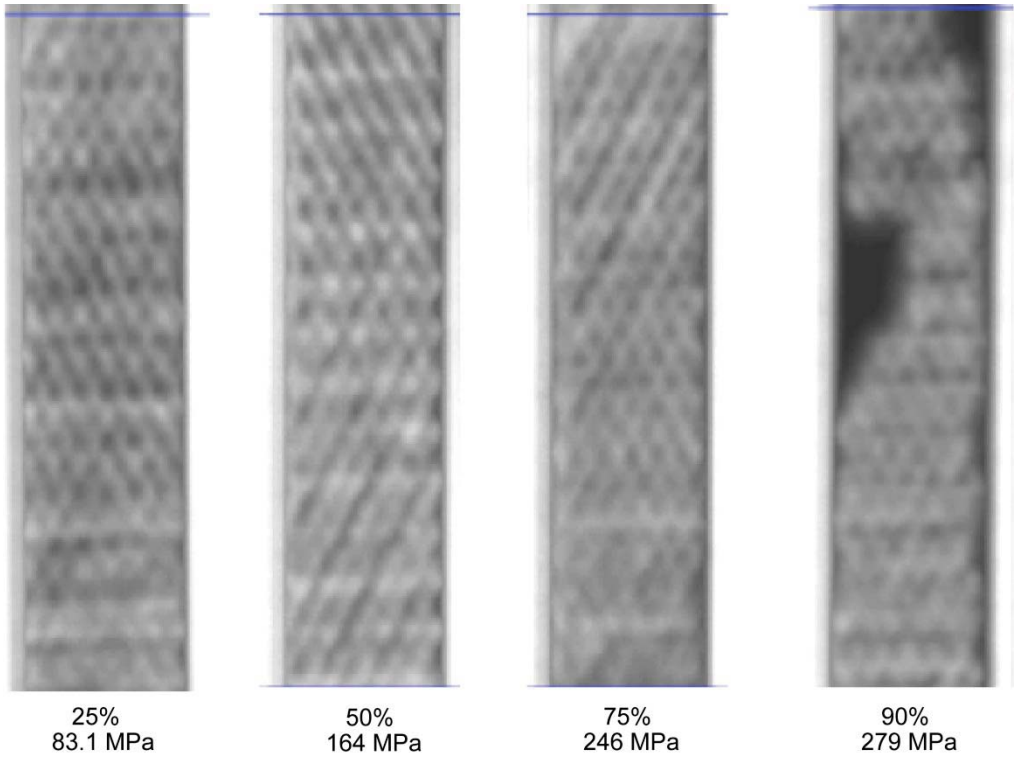

Figure 4.45.—Ultrasonic through transmission (UTT) scans from transverse tests of T700/3502 fiber/resin specimens loaded to stress values shown, corresponding to 25, 50, 75, and 90 percent of ultimate strength.

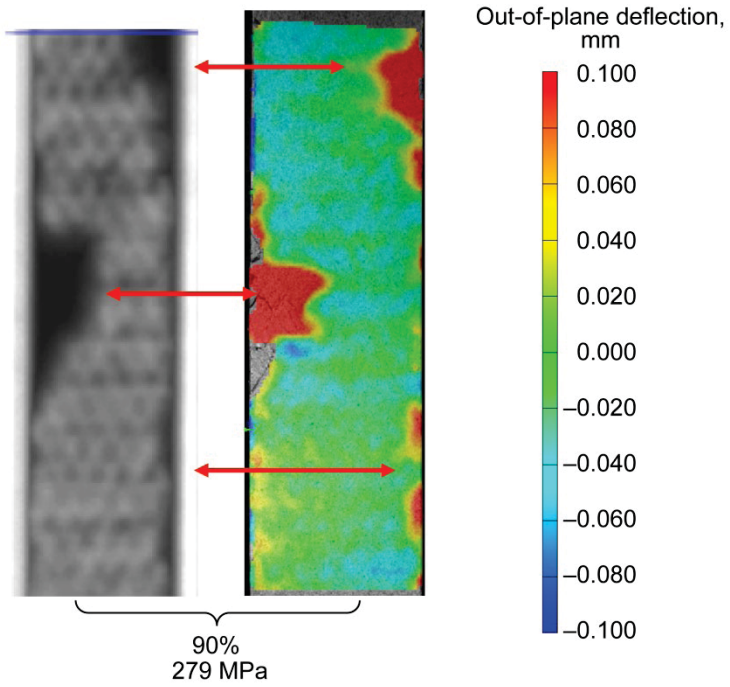

Figure 4.46.—Comparison of ultrasonic through transmission (UTT) and optical measurements from transverse tests of T700/3502 fiber/resin specimens loaded to stress value shown, corresponding to 90 percent of ultimate strength.

UTT scans confirmed the results shown by the optical measurement system. Only the 279-MPa specimen showed signs of out-of-plane displacements, whereas the others showed only normal deviations in the braid pattern. Figure 4.46 compares the two results.

The specimen loaded to 279 MPa presents a unique data point because it was the only specimen tested in the transverse direction that was able to be captured at the onset of specimen failure and showed any sort of damage occurring. The specimen failure was first detected by visible inspection after the test was completed; the areas of high out-of-plane displacement on the edges are areas in which the specimen showed visible cracks on the surface. The conclusion drawn from this test was that in transverse testing, specimens show that only right before failure did they exhibit out-of-plane displacements, which start along the specimen edges and propagate throughout the entire gage width. In order to understand the failure process, such detailed examination of the onset of failure in the transverse specimens is necessary.

Finally, digital microscopic imaging was used to examine the onset of the specimen failure at the microscopic scale. Figure 4.47 shows the two sections used for the microscopic imaging. Both are areas at the onset of specimen failure. Section “A” was cut such that the face of the viewing surface was parallel to the direction of applied load, whereas Section “B” was cut such that the face of the viewing surface was perpendicular to the direction of applied load. Figure 4.48 presents Section A from the specimen and shows clear damage in the axial fiber bundles, which was represented by the vertical cracks present in the axial fiber bundles. As described in Section 4.4.2.2, the cracking present in the axial fiber bundles represents the fiber bundle splitting, and is the main damage mechanism occurring in the transverse tensile tests, leading to nonlinearities in the global material response curve. Figure 4.49 shows Section B from the 90-percent transverse specimen. The circled areas show cracks on the specimen surface causing the delaminations seen by the out-of-plane displacement measurements from the optical measurement system.

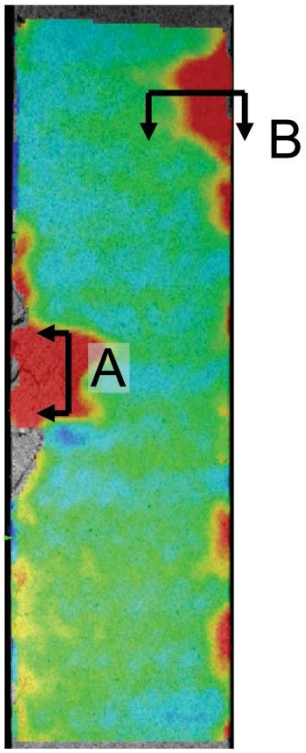

Figure 4.47.—Section locations in the T700/3502 fiber/resin transverse specimen loaded to 90 percent of ultimate strength in transverse tests that were used for microscopic imaging (Fig. 4.48).

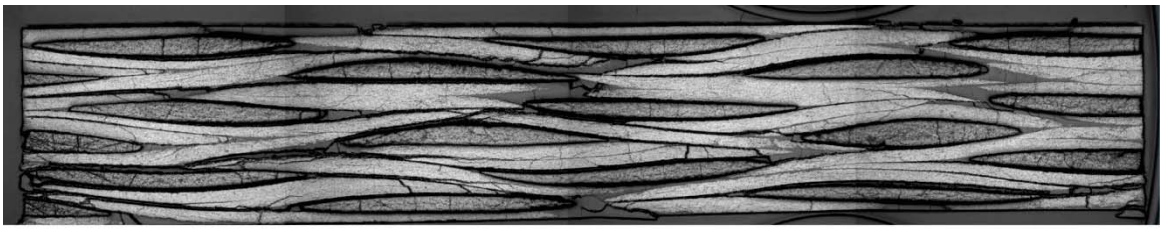

Figure 4.48.—Digital microscopic image of section A (see Fig. 4.47) of T700/3502 fiber/resin transverse tension specimen loaded to 90 percent of ultimate strength.

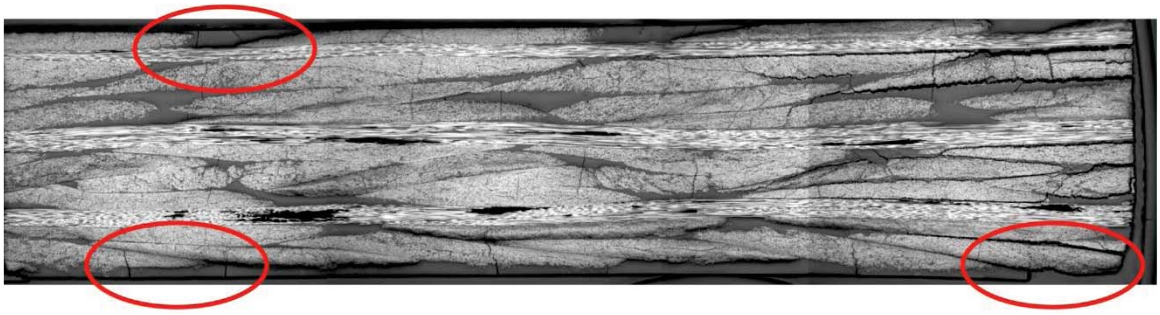

Figure 4.49.—Digital microscopic image of section B (see Fig. 4.47) of T700/3502 fiber/resin transverse tension specimen loaded to 90 percent of ultimate strength.

By using Figures 4.48 and 4.49 and the material response data, a full understanding can now be obtained of how the transverse tensile specimens fail. The damage in the specimen starts from the initiation of the axial fiber bundle splits. The onset of these splits causes the global material response curve to become nonlinear. The damage accumulation in the composite is the result of the fiber bundle split propagation. At the onset of specimen failure, the fiber bundle splits are great enough to cause surface cracks near the edges of the composite, leading to the out-of-plane displacements seen in Figure 4.47. The final failure in the composite occurs when the surface cracks extend from one edge of the composite to the other, leaving no path for the load to travel. Once the surface crack reaches both edges of the composite coupon, the coupon fails.

4.5 Composite Testing Summary

This section presents the composite material testing that has been completed using optical measurement techniques, which capture some important characteristics of triaxial braided composite materials normally undetectable using conventional methods. Composite coupon testing has been completed, and global stress-strain material response curves have been presented. The global material response data shows that optical measurement techniques can be utilized in static testing to obtain material properties of triaxial braided composite materials.

The data also show that the local deformations of the composite specimens can be examined and quantified. By utilizing some of the overlay techniques developed, precise locations for areas of high and low strain were determined. Also, material parameters such as matrix cracking causing transverse fiber bundle failure and delaminations in the braid architecture were examined.

The use of the optical measurement system provided insight into the nature of the premature failure of the weaker material systems and led to preliminary conclusions about the fiber-matrix interface in general. The results obtained by the optical measurement system suggest that a weak interface causes initiation of transverse fiber failure sooner than a strong interface. A weak interface also distributes the load more evenly than a strong interface, and properties like fiber splitting grow more abundant because of this load distribution. Also, a weak interface causes premature failures in the axial fibers and fiber layer delaminations resulting in nonlinear behaviors in the stress-strain response curves. However, the interface characteristics did not influence the modulus of the overall composite because the modulus values are taken from the very beginning of the stress-strain curves.

The optical measurement system, along with confirmations from UTT scans, was able to show that some of the damage causing mechanisms in the composite tests for the axial direction was delaminations within the fiber braid layers. The stronger T700/E862 fiber/resin material system started to show signs of delamination at approximately 75 percent of its ultimate stress, and the weaker T700/3502 material system showed signs of delamination at approximately 50 percent ultimate stress. It was at these points that the global specimen material response curves became nonlinear. In the transverse direction, the optical measurement system was able to capture the large out-of-plane deformations at the onset of failure.

The information presented in this section not only provides a greater insight into the nature of specimen response, but also will provide critical material parameters used when developing a computer model, which will be presented in the next section.

5.0 Development of Macromechanical Triaxial Braided Composite Computer Model

The previous chapters describe test methods developed and implemented to measure the material response of the constituents and coupons of triaxial braided composites. Also, mechanisms affecting the overall material response have been presented. While the full-field data presented provides a unique insight into the nature of the material response, it can also be utilized in the development of a finite-element-based approach to model braided composites. The methods described in this chapter provide a

systematic approach that utilizes the full-field material response data and braid geometry for implementation into a finite-element model. Information from the experiments is used along with the current material models available in LS–DYNA (Ref. 66), a commercially available transient dynamic finite-element code, to simulate the influence of the braided architecture on the failure process of the testing completed.

5.1 Material Background

Two material systems from the tested composite coupons described in Section 4.0, "Investigations of Triaxial Braided Composite Material Response" were simulated. The T700/PR520 and T700/E862 fiber/resin material systems were chosen because they were the highest strength material systems studied as shown by the test data and are therefore of the greatest interest for use in composite structures. As described in the previous sections, the fiber was Toray's high-strength, standard-modulus T700 fiber, and the resins were CYCOM PR520 (Cytec Industries, Inc.) and Epon 862 (Momentive Specialty Chemicals, Inc.).

5.2 Composite Microstructure

The method for modeling the composite braid architecture is presented first. Figure 5.1 shows the composite braid architecture and highlights the unit cell geometry common to the material systems tested. A unit cell is considered to be the smallest repeating volume of the composite where the behavior of the unit cell can be considered to be representative of the composite as a whole. For the analysis technique developed, a single unit cell was also divided into four subcells, labeled A through D. Figure 5.1(a) shows the fiber orientation in a single layer of a braided preform. In Figure 5.1(b), part I, shows a magnification of one unit cell for one layer of braid of the composite. Part II is a top view of a geometric representation of the three-dimensional model of the braid architecture, and part III shows a side view of the geometric representation. The +60° fibers are represented in green, while the –60° fibers are represented in red, and the 0° fibers are represented in blue. Finally, part IV shows the braid architecture in a homogenized condition by using the layers of the composite braid, and dividing them up into layers of unidirectional composites within each subcell. The full composite architecture was represented by placing each of the stacked unidirectional layers comprising each subcell adjacent to each other to make a complete unit cell.

Because of the nature of the braiding scheme, the fiber layup was different in each of the individual subcells. As shown by the subcell illustrations in Figure 5.1(b), part II, subcell A contains a –60° fiber above of a 0° fiber, which is above a 60° fiber on the bottom (represented by red). Subcell B contains only a –60° fiber above a 60° fiber; subcell C contains a 60° fiber above a 0° fiber on top of a –60° fiber. Finally, subcell D contains a 60° fiber above a –60° fiber. This braid architecture in each of the subcells shown in Figure 5.1(b), part II, was represented by stacking these fiber directions as layers through the thickness, as shown in Figure 5.1(b), part IV. A single unit cell with braid orientation was represented as a series of subcells with layers of unidirectional fiber tows stacked through the thickness. The unit cell with subcell geometries as defined here was the basis for the modeling technique.

When making the finished composite material, six layers of braid (representing the fabricated composite) were used. Figure 5.2 shows a cross section of a finished composite panel, with the full six layers of braid present, that was obtained from digital microscopic imaging.

Figure 5.2 shows a side view cross section of a digital microscopic picture of a finished composite panel. Upon examination of the microscopy pictures the phenomena known as fiber shifting, or the relative position of the unit cells through the specimen thickness, was observed. Fiber shifting was incorporated into the model because if the assumption was made that all of the subcells were in the same relative position throughout the thickness, then subcells B and D (having only +60° and –60° fibers as shown in Figure 5.1) would potentially be overly weak due to the lack of axial (0°) fibers. Also, shifting was included to account for the assumption of quasi-isotropy (by shifting the subsequent layers of subcells, each of the subcells of the full six-layer finished composite would have an equal number of 0°, –60°, and 60° fibers). In Figure 5.2, the dark areas represent the cross sections of the axial fiber bundles,

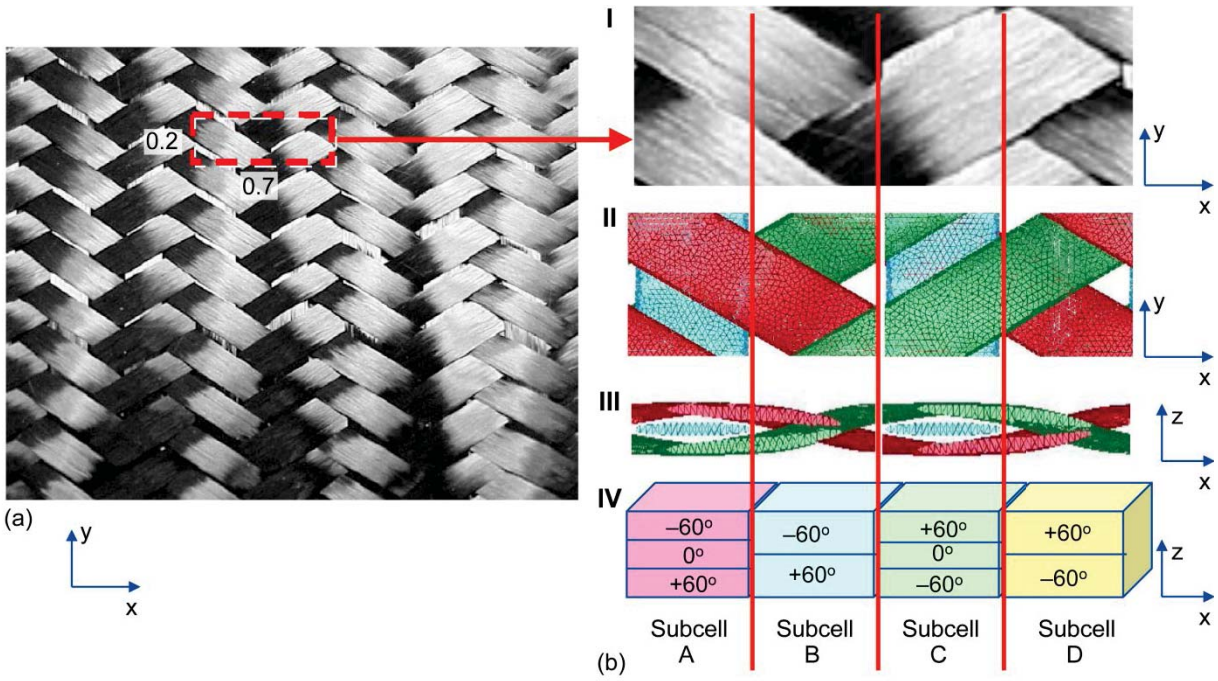

Figure 5.1.—Triaxial braided preform. (a) Single layer of preform, identifying unit cell. (b) Unit cell detail.

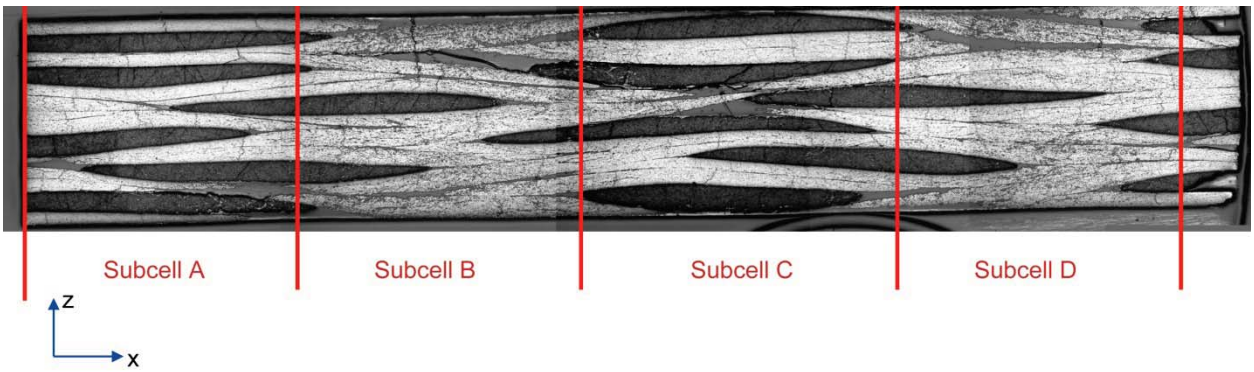

Figure 5.2.—Cross section of finished triaxially braided composite panel.

as they are orientated perpendicular to the cut, while the white areas represent bias fiber bundles, and are orientated at 30° to the cross-sectional cut. The small areas of grey between the fiber bundles represent resin-rich pockets. Subcell designations shown in the figure were picked to represent the subcells for the topmost layer of braid. Subsequent layers were shown to have significant misalignments under the topmost layer. These relative changes in position for subsequent layers through the thickness suggested that subcell shifting was prevalent enough such that it needed to be accounted for when modeling. Subcell shifting is accounted for in an idealized way when modeling the braid geometry; the analysis method shifted the unit cell by one subcell for each of the layers through the thickness of the composite, which will be described in detail in Section 5.3.1, “Development of Braid Geometry.”

5.3 Triaxial Braided Composite Model Development

The commercial transient dynamic finite-element code, LS–DYNA (Ref. 66), was used to analyze the triaxial braided composites discussed in this paper. LS–DYNA was used because of its ability to simulate impact events, which is the ultimate goal of this modeling technique, and will be discussed in Section 6.0.

Both the triaxial braid geometry and the material properties obtained from testing were incorporated into the model. First, the methods for approximating the composite braid architecture will be discussed, and then the methods developed for the utilization of the test data within the finite-element model will be presented.

5.3.1 Development of Braid Geometry

The idealized full six-layer composite geometry that will be simulated in the finite-element model is shown in Figure 5.3. The model developed is an extension of the model first developed by Cheng (Ref. 67). Cheng's original methodology will be modified because Cheng did not include the fiber shifting phenomena observed and described in the previous section.

As Figure 5.3 shows, the shifting of the unit cell under the topmost layer was accounted for in the braid geometry. Subcell A, represented in pink, was in the leftmost portion of the unit cell on the top layer; however, subsequent layers underneath the top layer show that it has shifted to the left by one subcell.

In LS–DYNA, each subcell was modeled as a Part, which is the LS–DYNA term for a discrete entity. All subcells were modeled using a shell element since the length and width of the composite structures being examined were much greater than the thickness. Each Section card contained properties such as element thickness, which represented the thickness of the entire composite specimen; number of integration layers, which defined the number of fiber layers through the cross section; and integration layer orientation, which described the angle of the fiber at each particular layer. Thus, the Section card in each of the subcells included 15 integration points, which represented the 15 layers of fibers through the thickness of the composite. Finally, separate Integration cards were used for each subcell. The Integration card was referenced by each individual subcell Section cards. The Integration card included parameters

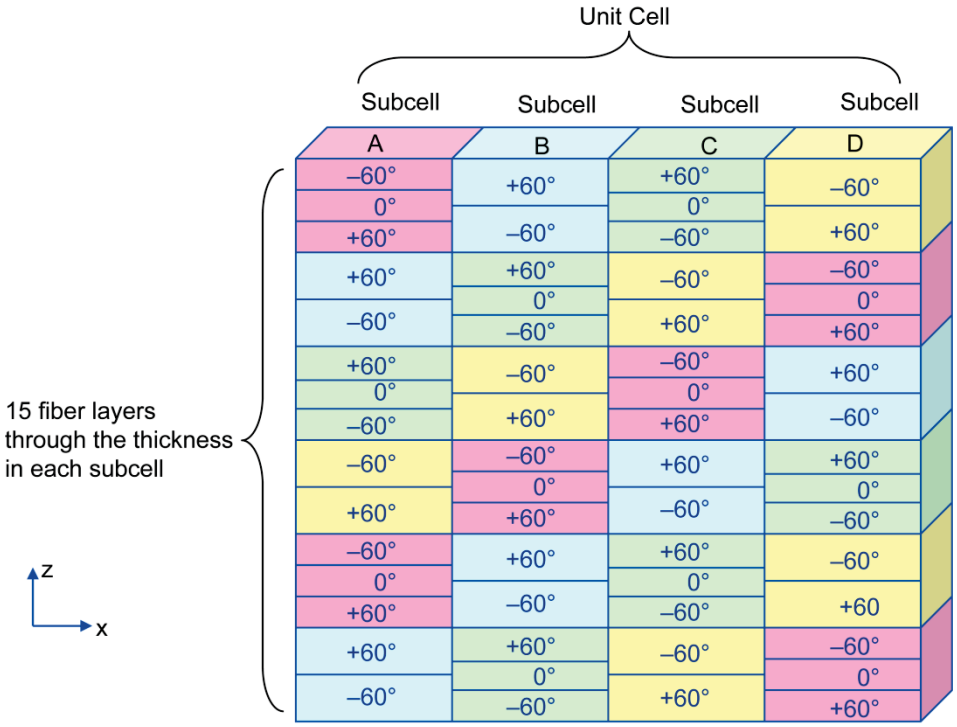
Unit Cell
Subcell
Subcell
Subcell
Subcell
A
B
C
D
–60°
0°
+60°
+60°
0°
–60°
+60°
–60°
–60°
+60°
+60°
0°
–60°
–60°
+60°
+60°
0°
–60°
–60°
+60°
+60°
0

such as individual fiber layer position through the thickness of the section, and relative weight for each of the layers. For ease of the material model equation development, the analysis method assumed that each of the 15 fiber layers had the same thickness, which spaced all of the fiber layers equally throughout the thickness. To account for the differences in sizes between the 24k axial and 12k bias fiber bundles, the axial layers were weighted twice the amount as the bias layers.

For example, looking at Figure 5.3, Subcell A was modeled as Part 1, which had a corresponding Section 1. Section 1's integration layers reflected the braid geometry seen in Figure 5.3. Going from bottom to top in subcell A, the orientation of the fibers were as follows: –60°, 60°, 60°, 0°, –60°, –60°, 60°, –60°, 0°, 60°, –60°, 60°, 60°, 0°, –60°. All layers were equally spaced, and the normalized weights on the axial (0°) fibers were double that of the bias (60°) layers.

5.3.2 Composite Material Property Implementation

The constitutive material model within LS–DYNA that was employed for all of the subcells was a continuum-damage-mechanics-based orthotropic material model, based on a model developed by Matzenmiller, Lubliner, and Taylor (Ref. 68). This material model assumes that applied deformation causes damage initiation and progression, which is captured by a stiffness reduction in the material. The stiffness reduction is accounted by introducing three damage parameters: ω_{11}, ω_{22}, and ω_{12}, which represent damage in the axial, transverse, and shear directions, respectively, into the compliance matrix in the constitutive equation. Detailed evolution laws govern the relationship between applied deformation and values of the damage variables. A detailed discussion about general uses of this material model in LS–DYNA is presented in Schweizerhof et al. (Ref. 69).

The continuum-damage-based material model used for the computer model was called MAT_LAMINATED_COMPOSITE_FABRIC (Mat 58) within LS–DYNA as a Material card for each of the individual parts. For the elastic portion of the analysis, which will be described first, each layer's effective unidirectional ply properties needed to be entered as part of the model input.

The unidirectional laminate properties needed for the material models are as follows: axial modulus (E_{11}), transverse modulus (E_{22}), in-plane shear modulus (G_{12}), and in-plane Poisson's ratio (ν_{21}). The methods for obtaining the effective unidirectional ply-level properties (E_{11}, E_{22}, ν_{21}, G_{12}) that are needed for each integration layer in each of the subcells are developed in this section. Cheng (Ref. 67) used carbon fiber and resin matrix properties, along with classically based composite micromechanics approaches for material property implementation, which represented a bottom-up approach. The method developed in this section also differs from Cheng in that it will take a top-down approach. The key feature of the approach is that the required properties were "backed out" from coupon-level test data obtained and presented in Section 4.0 by using classical laminated plate theory (CLPT) and classical composite micromechanics techniques. A discussion of these techniques can be found in References 41, 70, and 71. Many of the specimen geometries and boundary conditions utilized for the model development were the same as those used in the composite testing described in Section 4.0. The analytical technique started by first examining results from a transverse tensile test, in which the specimen geometry was taken from the ASTM D3039 standard (Ref. 17). In this test, the axial (0°) fibers are oriented perpendicular to the applied load P_x as shown in Figure 5.4. To represent the transverse tensile test in the model, the four subcells of the unit cell were orientated parallel to the direction of the load (Fig. 5.4).

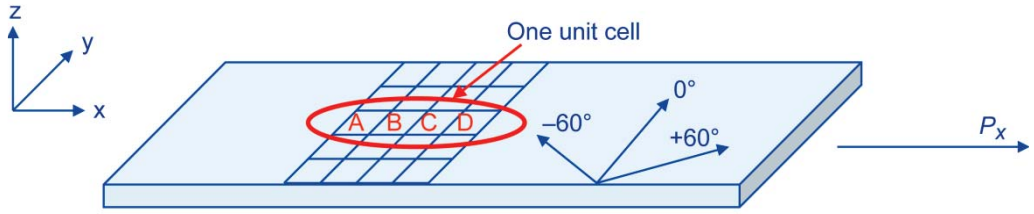

Figure 5.4.—Triaxial braided composite transverse tension test geometry with load P_x.

The development of the technique required some assumptions. By first assuming that all six layers of braid in the specimen carried the same load, the total load gathered from the test was divided by the number of layers in the composite to determine the load P_x in each layer of braid. Next, the assumption was made that all of the unit cells along the width of the specimen carried equal loading, so the load was also divided by the number of unit cells along the width, which gave the total load for each unit cell. This means that the analysis technique was developed for the unit cell shown in Figure 5.1 (bottom right), not the full 15-layer composite geometry shown in Figure 5.3. The full 15 layers of the braid architecture were implemented in the LS–DYNA Section card. Note, that CLPT also required traction $N_{x,}$ so the total load was taken to be per unit length, which meant that it was also divided by the width of each unit cell. Equation (5.1) shows the final traction value used in the analysis:

$$N_x = P_x \Big/ (\#\text{Layers} * \#\text{Unit cells} * \text{Width}) \tag{5.1}$$

The traction N_x next had to be partitioned among each of the subcells in the unit cell. For this process, and for the methods described in the remainder of this section, uniform stress (or load) and uniform strain assumptions that have been applied in micromechanics methods in the past (Ref. 41) need to be applied between the subcells. For example, in the ASTM 3039 transverse tensile test configuration, the load N_x was assumed to be equal in all of the subcells:

$$N_x^A = N_x^B = N_x^C = N_x^D \tag{5.2}$$

The subscript x in Equation (5.2) represents the direction of loading, and the superscript represents the subcell name. Next, the volume average of the load in the y-direction in each of the subcells N_y was assumed to be equal to 0 since there was no applied load in that direction.

$$V_f^A * N_y^A + V_f^B * N_y^B + V_f^C * N_y^C + V_f^D * N_y^D = 0 \tag{5.3}$$

Each V_f represents the volume fraction of its subcell as compared to the volume of the entire unit cell, and not the fiber volume fraction of the as-fabricated composite. Note that because subcell C had the same volume fraction as subcell A and subcell D had the same volume fraction as subcell B, Equation (5.3) can be rewritten:

$$2 * V_f^A * N_y^A + 2 * V_f^B * N_y^B = 0 \tag{5.4}$$

Next, CLPT was used to relate N_x and N_y in each subcell to the strains in the subcell. Although on a local level the laminate orientations in each subcell were not symmetric, when accounting for all six layers in the composite on a global level, the composite was assumed to be symmetric. This assumption was verified by looking at the full-field strain data. By examining the out-of-plane deflections on the composite specimens during testing, care was taken to ensure that out-of-plane bending did not occur. Knowing that out-of-plane bending did not occur, the assumption was made that the B constitutive matrix normally associated with CLPT, which would account for the out-of-plane bending, was set equal to 0. Furthermore, on the local level only the in-plane strains were needed and obtained from the test data, so the D matrix normally associated with CLPT was not analyzed. The laminate orientations were assumed to be balanced on the global level, so the A16 and A26 components of the A matrix from CLPT were set equal to 0. To summarize, in-plane normal loads were assumed to be a function of in-plane normal strains, and shear loads are assumed to be a function of shear strains; that is, the strains were uncoupled. These are commonly used when examining composite material response using CLPT and have been widely reported. The assumptions above can be used to rewrite the CLPT in equation form, as shown in Equation (5.5):

$$\begin{bmatrix} N_x^A \\ N_y^A \\ N_{xy}^A \end{bmatrix} = \begin{bmatrix} A11^A & A12^A & 0 \\ A12^A & A22^A & 0 \\ 0 & 0 & A66^A \end{bmatrix} \begin{bmatrix} \varepsilon_x^A \\ \varepsilon_y^A \\ \varepsilon_{xy}^A \end{bmatrix} \tag{5.5}$$

In Equation (5.5), the superscript A represents the subcell name. Similarly, the constitutive equations for subcells B, C, and D were written. Expanding the matrix in Equation (5.5) above for N_x and N_y, Equations (5.6) and (5.7) were obtained for subcell A and Equations (5.8) and (5.9) were obtained for subcell B:

$$N_x^A = A11^A * \varepsilon_x^A + A12^A * \varepsilon_y^A \tag{5.6}$$

$$N_y^A = A12^A * \varepsilon_x^A + A22^A * \varepsilon_y^A \tag{5.7}$$

$$N_x^B = A11^B * \varepsilon_x^B + A12^B * \varepsilon_y^B \tag{5.8}$$

$$N_y^B = A12^B * \varepsilon_x^B + A22^B * \varepsilon_y^B \tag{5.9}$$

Noting that subcells A and C both had the same layers of 0° fibers, layers of 60° fibers, and layers of –60° fibers, only subcell A was examined. Similarly, since subcells B and D had the same number of 60° and –60° layers, only subcell B was examined.

The A matrix terms were expanded by using CLPT, and are represented in Equation (5.10):

$$A_{ij} = \sum_k \overline{Q}_{ij} * t_k \tag{5.10}$$

In Equation (5.10), t is the thickness of the k^{th} layer. The expansion of the A_{ij} matrix was specifically written for subcells A and B is shown in Equations (5.11) and (5.12):

$$A_{11}^A = \overline{Q}_{11}^{60°} * t + \overline{Q}_{11}^{0°} * t + \overline{Q}_{11}^{-60°} * t \tag{5.11a}$$

$$A_{12}^A = \overline{Q}_{12}^{60°} * t + \overline{Q}_{12}^{0°} * t + \overline{Q}_{12}^{-60°} * t \tag{5.11b}$$

$$A_{22}^A = \overline{Q}_{22}^{60°} * t + \overline{Q}_{22}^{0°} * t + \overline{Q}_{22}^{-60°} * t \tag{5.11c}$$

$$A_{11}^B = \overline{Q}_{11}^{-60°} * t + \overline{Q}_{11}^{+60°} * t \tag{5.12a}$$

$$A_{12}^B = \overline{Q}_{12}^{-60°} * t + \overline{Q}_{12}^{+60°} * t \tag{5.12b}$$

$$A_{22}^B = \overline{Q}_{22}^{-60°} * t + \overline{Q}_{22}^{+60°} * t \tag{5.12c}$$

In Equations (5.11) and (5.12), the $\overline{Q}$ terms are the transformed stiffness terms for a unidirectional ply in the structural axis system. Note that the $\overline{Q}$ terms for the 0° fiber are not present in subcell B because 0° fibers are not present in subcell B. The $\overline{Q}$ terms were then decomposed into their representative Q terms, which represent the stiffness for a unidirectional ply layer in the material axis system for the axial, transverse, and shear directions. In general,

$$\overline{Q}_{11} = m^4 * Q_{11} + n^4 * Q_{22} + 2 * n^2 * m^2 * Q_{12} + 4 * m^2 * n^2 * Q_{66} \tag{5.13a}$$

$$\overline{Q}_{12} = m^2 * n^2 * Q_{11} + m^2 * n^2 * Q_{22} + \left(m^4 + n^4\right) * Q_{12} - 4 * m^2 * n^2 * Q_{66} \tag{5.13b}$$

$$\overline{Q}_{22} = n^4 * Q_{11} + m^4 * Q_{22} + 2 * n^2 * m^2 * Q_{12} + 4 * m^2 * n^2 * Q_{66} \tag{5.13c}$$

In Equation (5.13), *m* represents the cosine of the braid angle and *n* represents the sine of the braid angle. Thus Equation (5.13) was substituted into Equations (5.11) and (5.12) noting that the values for *m* and *n* changed for the different bias directions.

There are six unknown variables in the equations derived above for the transverse test configuration—Q_{11}, Q_{12}, Q_{22}, Q_{66}, N_y^A, and N_y^B—and only five equations available for finding the unknown variables—Equations (5.4) and (5.6) to (5.9). Representative subcell strains in both the axial and transverse directions were directly measured from the optical measurement system described in Section 4.0. The main advantage of the method described is that by using the above-developed equations and the optical measurement system's results, strain was not an unknown; rather, strains in each of the subcells for both directions were known.

Figure 5.5 shows an example of the subcell strains in both the axial and transverse direction for both subcells A and B, as measured by the optical measurement system. Since the optical measurement system computed strain over the full specimen, multiple subcells were visible. The local subcell strains presented were representative samples of the many subcells measured.

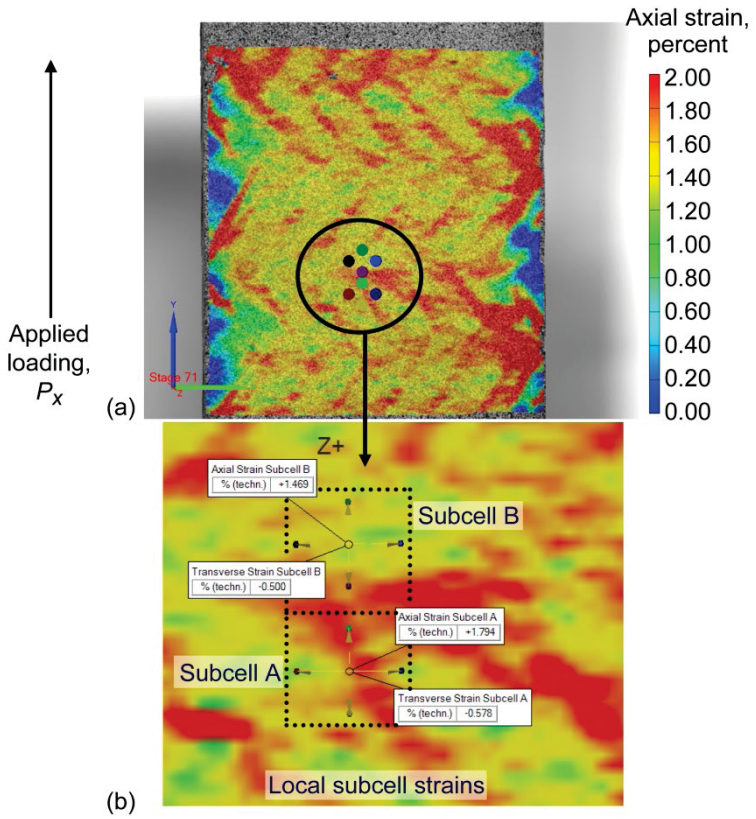

Figure 5.5.—Optically measured strains for a triaxial braided transverse composite specimen. (a) Global axial strain. (b) Local subcell strain.

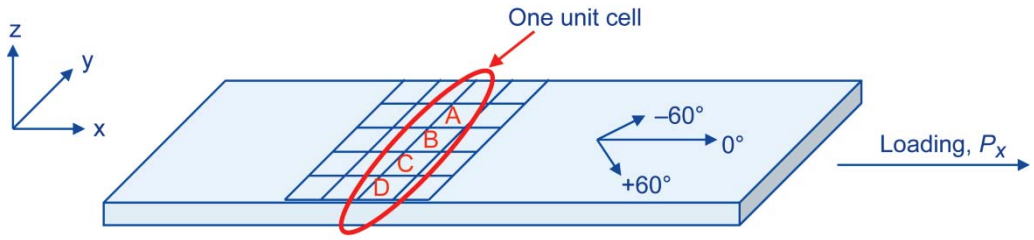

Figure 5.6.—Triaxial braided composite axial tension test schematic.

In an axial tension test, the axial (0°) fibers were oriented to the direction of loading. This was represented by orienting the four subcells perpendicular to the direction of loading.

An important point to note for the discussion that follows is that the composite was once again assumed to be loaded in the "x-direction." That means that in terms of the unit cell orientation the axis orientation was switched 90° from the transverse loading case. In other words, what was considered to be the y-direction previously was now the x-direction, and vice versa. In axial tension testing, only one uniform stress assumption needed to be applied for the model development. Since the unit cell was being pulled in the x-direction, the effective force in the y-direction must have been equal to 0. The force in the y-direction in each of the subcells was also assumed to be equal. Expressed as equations, these assumptions translated to

$$N_y^A = N_y^B = N_y^C = N_y^D = 0 \tag{5.14}$$

The CLPT equations were expressed for the y-direction only for the case of an axial tension test. Note that the A_{ij} terms were not the same as they were for the transverse tension testing, as the angles for m and n have changed by 90° because the orientation of the unit cell has changed by 90°.

$$N_y^A = 0 = A12^A * \varepsilon_x^A + A22^A * \varepsilon_y^A \tag{5.15}$$

$$N_y^B = 0 = A_{12}^{B\,B} * \varepsilon_x^B + A_{22}^B * \varepsilon_y^B \tag{5.16}$$

By taking into account the 90° change in angle in the A_{ij} terms, there were seven equations (Eqs. (5.4), (5.6) to (5.9), (5.15), and (5.16)) and only six variables (Q_{11}, Q_{12}, Q_{22}, Q_{66}, N_y^a, and N_y^b) for the transverse tensile test. Now 6 out of the 7 equations can be used for the solution and the 7th equation can be used for verification.

Since the ultimate goal was to find the unidirectional ply material properties required for the material model, the Q terms were decomposed as follows:

$$Q_{11} = \frac{E_{11}}{1 - v_{12} * v_{21}} \tag{5.17}$$

$$Q_{22} = \frac{E_{22}}{1 - v_{12} * v_{21}} \tag{5.18}$$

$$Q_{12} = \frac{v_{21} * E_{11}}{1 - v_{12} * v_{21}} \tag{5.19}$$

$$Q_{66} = G_{12} \tag{5.20}$$

In Equations (5.17) to (5.20), the unidirectional-ply-level axial modulus (E_{11}), transverse modulus (E_{22}), in-plane shear modulus (G_{12}), and in-plane Poisson's ratios (v_{12} and v_{21}) were the unknown variables. Again, there were more unknowns than equations. The final equation came from elasticity theory:

$$\frac{E_{11}}{v_{12}} = \frac{E_{22}}{v_{21}} \tag{5.21}$$

Knowing the Q_{ij} from above and using Equations (5.17) to (5.21), E_{11}, E_{22}, G_{12}, v_{12}, and v_{21} were found. These values were the effective unidirectional engineering properties of the composite ply at each integration point in the finite-element model.

By using the measured subcell strains and values of load from the test data as the inputs into the material model, representative material properties were found. Because the values of strain and load were measured from fabricated composite coupons, the model's effective unidirectional-ply-level properties included items such as the interface effects between the fibers and matrix and also inherent localized deficiencies present in real fabricated composite materials such as resin rich pockets. Thus, the material model does include many of the micromechanical properties and deficiencies present in the fabricated composite materials, but utilizes them macromechanically.

5.3.3 Development of Material Failure Parameters

Ply-level material properties were one portion of what the material constitutive model in LS–DYNA required as inputs. The other requirement was that the initial ply-level unidirectional failure strengths for the composite needed to be found. The initial failure criteria implemented within the LS–DYNA material model was based on the Hashin (Ref. 72) failure criteria and has the parameters specified in Table 5.1 as input.

Failure values were extracted from the composite test data based on the requirements in Table 5.1. Observations were made on the full-field strain data from the various axial and transverse tensile and compressive tests conducted. The T700/PR520 fiber/resin material system will be used for an example of how the material properties needed were obtained.

The simplest parameters to observe were the axial tensile values. The main assumption for extracting the axial tensile strength from these results was that the braided composite was effectively acting as a unidirectional laminated composite, and therefore the axial tensile strength obtained during the test could be extrapolated to be the axial tensile strength of a unidirectional layer. The LS–DYNA strain at axial tensile strength, E11T, was found by observing the strain in an axial tensile specimen at failure. The LS–DYNA axial tensile strength XT was found by recording the ultimate tensile strength that occurred at the ultimate strain. Figure 5.7 shows a representative example of an axial tension test.

TABLE 5.1.—FAILURE VALUES NEEDED IN LS–DYNA FINITE-ELEMENT MATERIAL MODEL

Parameter	Description
E11T	Strain at longitudinal tensile strength
E11C	Strain at longitudinal compressive strength
E22T	Strain at transverse tensile strength
E22C	Strain at transverse compressive strength
GMS	Strain at in-plane shear strength
XT	Longitudinal tensile strength
XC	Longitudinal compressive strength
YT	Transverse tensile strength
YC	Transverse compressive strength
SC	Shear strength

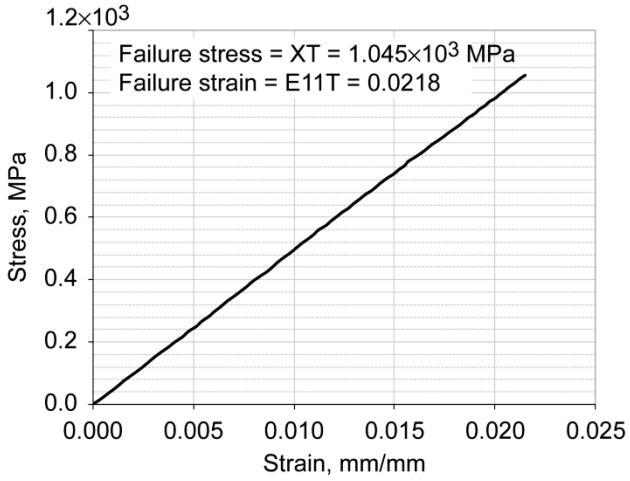

Figure 5.7.—T700/PR520 fiber/resin axial tensile test response, yielding XT and E11T parameters (longitudinal tensile strength and strain at longitudinal tensile strength, respectively) for material modeling in LS–DYNA.

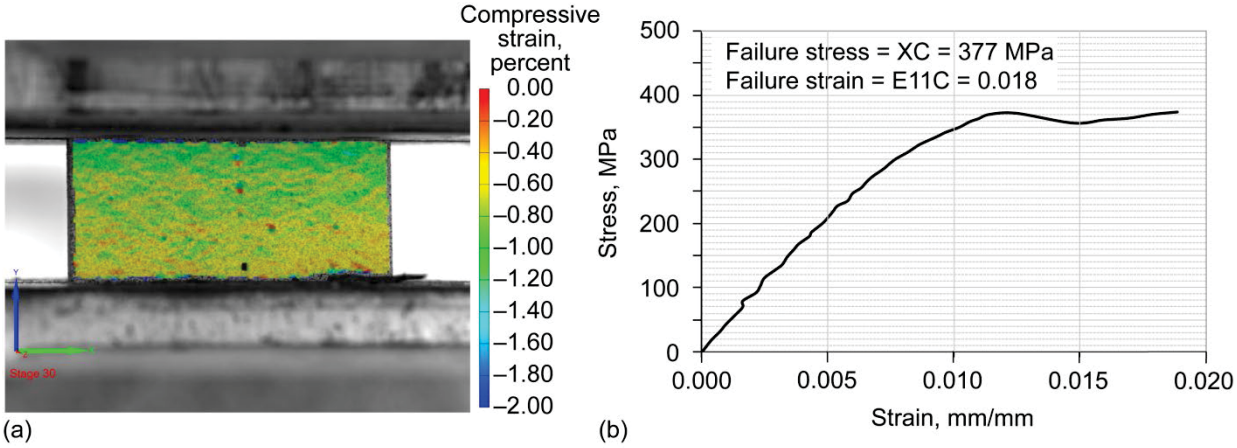

Figure 5.8.—Axial compression of T700/PR520 fiber/resin system. (a) Full-field axial compressive strain from optical measurements. (b) Axial compression test response, yielding XC and E11C parameters (longitudinal failure strength and strain, respectively) for material constitutive modeling in LS–DYNA.

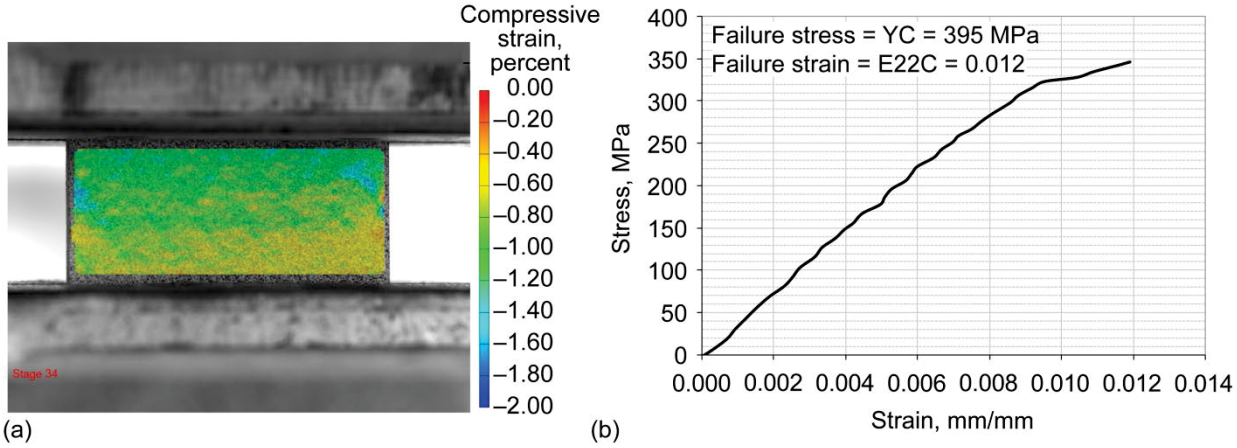

Figure 5.9.—Transverse compression of T700/PR520 fiber/resin system. (a) Full-field transverse compressive strain from optical measurements. (b) Stress-strain response, yielding YC and E22C parameters (longitudinal failure strength and strain, respectively) for material modeling in LS–DYNA.

In compression, the full-field strain data show that the composite behaved as a homogenous material. Unlike tensile tests, there were no areas of high and low strain, but rather a uniform strain field was present in the composite. Knowing this, the LS–DYNA strain at axial compressive strength, E11C, was found by observing the strain in an axial compression specimen at failure. The LS–DYNA axial compressive strength XC was found by recording the ultimate compressive strength that occurred at the ultimate compressive strain, even after the inelastic deformation, which is represented by the plateau in the material response curve. Figure 5.8(a) shows the uniform strain field present in an axial compression specimen, as measured by the optical measurement system, and Figure 5.8(b) shows the material response, with material parameters used.

Similarly, for compression in the transverse direction, the composite acted as a homogenous material. The LS–DYNA transverse tensile strength YC and strain at transverse compressive strength, E22C, were obtained from the material response from a transverse compression test. Figure 5.9(a) shows the uniform strain field present in a transverse compression specimen, and Figure 5.9(b) shows the stress-strain response from a transverse compression test.

Finding the transverse tensile values was not as well defined. Since the failure strength input that was required was that of an effective unidirectional composite, the transverse tensile strengths could not be directly determined by looking at the composite coupon stress-strain because the bias fibers significantly contributed to the composite failure strength. Instead a different approach was used. By using the full-field strain measurement technique and examining the stress that caused the onset of fiber bundle splitting, YT was assumed to be this stress. For reference, a discussion on transverse fiber bundle failures is presented in Section 4.4.2.2, and states that a fiber bundle split was a result of the matrix cracking, causing the fiber bundles to split in their transverse direction, representing a transverse failure of layers in the composite. However, the composite failed once the overall composite material response reached its failure strain, assumed to be E22T. Between the onset of the splitting in the individual fiber bundles (YT) and specimen failure (E22T), damage accumulated in the composite, which was demonstrated by the nonlinearities in the overall specimen response curves, shown in Section 4.4.1.1. As each of the individual fiber bundles reached their failure stress and split, their load-carrying capability diminished. The load from the failed fiber bundles was then distributed to other nonfailed fiber bundles in the specimen. As the other fiber bundles begin to carry the extra load from the failed bundles, they, in turn, began to fail. When the number of fiber bundle failures reached a critical value the composite specimen then failed at its ultimate failure strain, E22T.

The transverse failure caused by the fiber bundle splitting was represented in by setting the transverse tensile stress limiting parameter (SLIMT2) equal to 1 in the material model. Setting this parameter to 1 made each individual layer for each of the subcells in the model behave in an elastic-plastic manner in the transverse direction. In the elastic region, the fiber bundles carried load until they reached their ultimate stress value YT, and split. They then went into a plastic region. The plastic region represented the region in which each layer could not carry any more load and simulated the loading on the layer after a fiber bundle split occurred in the composite test. It allowed for the overall composite specimen to still carry load, even though individual fiber bundles could not. This meant that even though some of the individual fiber bundles failed, the overall specimen stress vs. strain material response continued to grow until the final strain assumed to be E22T, took place. In the transverse direction, the material response for a single layer would be as shown in Figure 5.10.

Figure 5.11(a) shows the full field strain measurement on a representative transverse coupon, and the global coupon stress versus local fiber bundle strain from a transverse tension test. When the transverse fiber bundle reached its failure stress, highlighted in Figure 5.11(b), the SLIMT2 parameter controlled the layers' material response until the composite reached its ultimate failure strain.

The material response curve of the localized area around a fiber bundle split should not be used after the fiber bundle split because of distortions in the speckle pattern caused by the split. Even though the fiber bundle splits do appear in the composite coupon in a regular fashion, the split itself caused discontinuities in the painted pattern, thus rendering it unusable. Accordingly, data obtained after the highlighted region in Figure 5.11(a) were not used after the value of YT was obtained. As a result, the value of E22T used in the analysis was the value of the transverse composite specimen failure. The value for E22T was taken from the overall composite stress-strain response and not from the failure value at the first fiber bundle split. The overall composite failure strain in the test specimen was representative of a composite coupon failure from the accumulated damage created by the fiber bundle split propagations. The overall composite transverse stress versus strain response is shown in Figure 5.12.

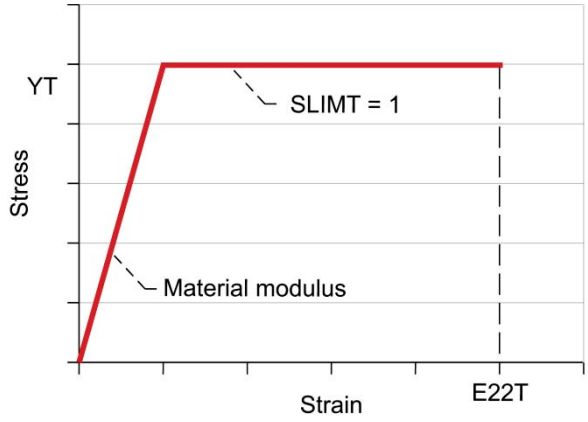

Figure 5.10.—Generic elastic plastic material response illustrating LS-DYNA parameters (transverse tensile strength YT, tensile stress limiting parameter SLIMT, and strain at transverse tensile strength E22T.

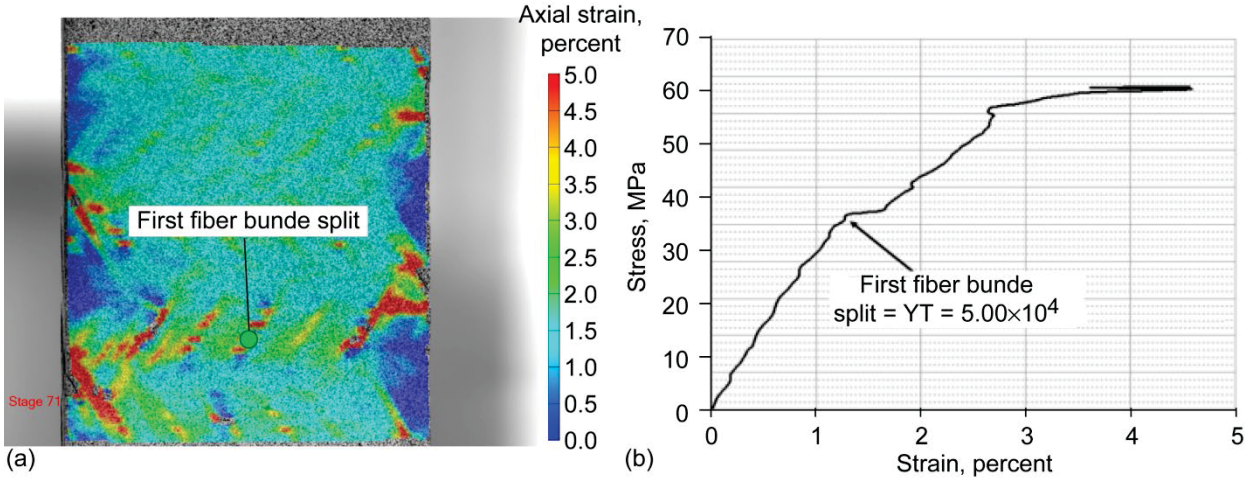

Figure 5.11.—Transverse tension of T700/PR520 fiber/resin system. (a) Full-field transverse tensile strain from optical measurements. (b) Stress-strain response, yielding the YT parameter (transverse tensile strength) for material modeling in LS-DYNA.

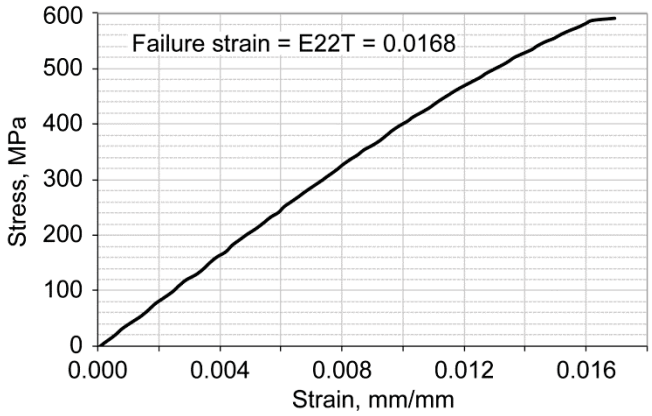

Figure 5.12.—Parameters used from transverse tensile test. T700/PR520 fiber/resin transverse tensile test response, yielding E22T parameter (and strain at transverse tensile strength) for material modeling in LS–DYNA.

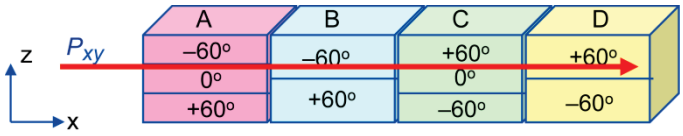

Figure 5.13.—Triaxial braided composite shear test geometry with load P_{xy}.

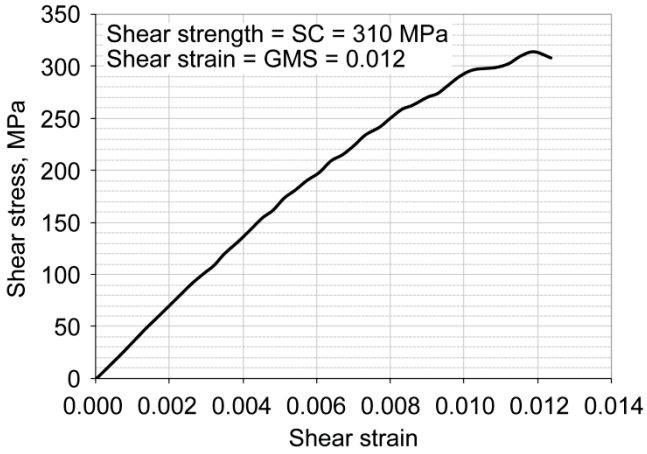

Figure 5.14.—T700/PR520 fiber/resin shear test response, yielding SC and GMS parameters (shear strength and strain at shear strength, respectively) for material modeling in LS–DYNA.

Shear parameters were found using shear testing according to ASTM D5379 (Ref. 20). Figure 5.13 shows the orientation of the unit cell under shear loading. Each of the subcells carried the same shear stress, and if the assumption was made that all thicknesses in each layer were the same, each layer for each subcell took the same shear stress. Knowing this, the shear data measured from the test were directly implemented into the model as unidirectional layer material parameters. A representative shear stress versus strain response is shown in Figure 5.14.

5.4 Finite Element Model Implementation for Prediction of Static Tests

The modeling approach described in the previous section was developed into an LS–DYNA finite-element model. Four shell elements, each having the dimensions of one subcell, were used as the basis for the finite-element model mesh. From this generic finite-element model, appropriate specimen geometries were created by using repeated patterns of the four-subcell layout.

To check the validity of the braided modeling approach used for analysis, two static finite-element models were created in LS–DYNA, one simulating an axial tensile test, and the other simulating a transverse tensile test. Both geometries were based on ASTM 3039 geometries. Figure 5.15 shows the geometries.

The fixed end in the model was constrained in all three displacement and rotation directions. The loading was applied at a constant velocity 0.635 mm/s (0.025 in./s), which was consistent with the test conditions. The red elements represent subcell A, the blue elements represent subcell B, the green elements represent subcell C, and the yellow elements represent subcell D. The unit cell orientations for both of the modeling conditions are highlighted for reference. In the axial test conditions the unit cell was oriented perpendicular to the direction of applied loading, which oriented the axial layers parallel to the direction of loading. In the transverse test conditions, the unit cell was oriented parallel to the direction of applied loading, which oriented the axial layers perpendicular to the direction of loading. These orientations were consistent with the test conditions.

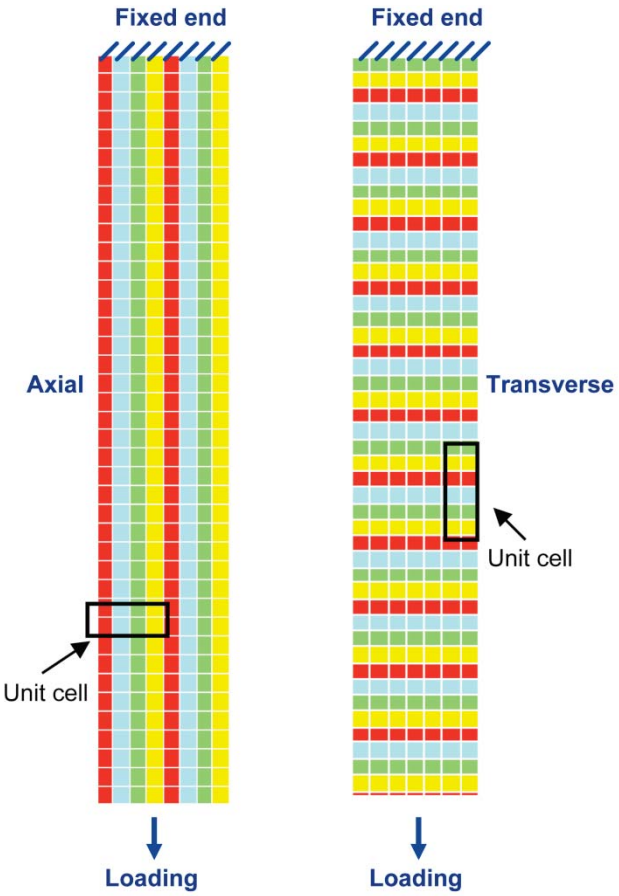

Figure 5.15.—Finite element model of triaxial braided composite ASTM 3039 (Ref. 17) test geometries.

Axial and transverse tensile tests were simulated in LS–DYNA and overall stress versus strain material response plots were output for each test. The stress-strain plots for the LS–DYNA simulations were compared against the experimental stress-strain curves obtained as discussed in Section 4.0. The next two sections divide up the two material systems tested: Section 5.4.1 discusses results obtained from the T700/PR520 material system, and Section 5.4.2 discusses results obtained from the T700/E862 material system.

5.4.1 T700/PR520 Fiber/Resin Material Response

Simulations were run using the data from the T700/PR520 material test as inputs in the finite-element model. Table 5.2 shows the parameters and values obtained from the developed method and used in the material model.

Figure 5.16 shows material response curve comparisons of a sample axial test and LS–DYNA simulations, which show good agreement. Table 5.3 compares the results of the LS–DYNA simulation and average test results.

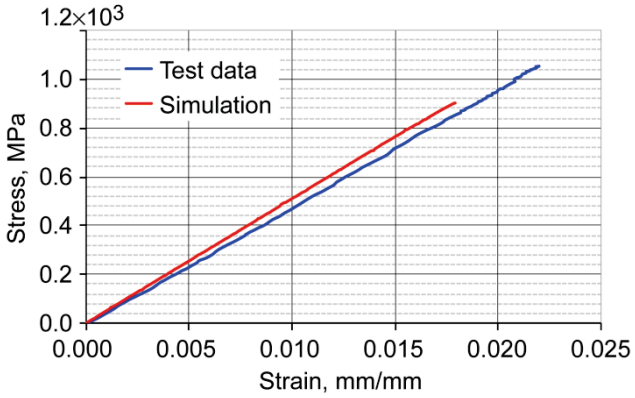

Figure 5.16.—Comparison of test and LS–DYNA simulation axial tension response for T700/PR520 fiber/resin material.

TABLE 5.2.—T700/PR520 FIBER/RESIN MATERIAL PARAMETERS USED FOR LS–DYNA MODEL

Material parameter (LS–DYNA name)	Value
Axial modulus (EA), GPa	51.3
Transverse modulus (EB), GPa	25.0
In-plane shear modulus (GAB), GPa	19.0
In-plane Poisson's ratio (PRBA)	0.071
Axial tensile failure strain (E11T)	0.0216
Axial compressive failure strain (E11C)	0.018
Transverse tensile failure strain (E22T)	0.0168
Transverse compressive failure strain (E22C)	0.011
In-plane shear failure strain (GMS)	0.012
Axial tensile stress at failure (XT), MPa	1045
Axial compressive stress at failure (XC), MPa	377.1
Transverse tensile stress at failure (YT), MPa	362
Transverse compressive stress at failure (YC), MPa	345
In-plane shear stress at failure (SC), MPa	307.3
Stress-limiting parameter for axial tension (SLIMT1)	0
Stress-limiting parameter for transverse tension (SLIMT2)	1
Stress-limiting parameter for axial compression (SLIMC1)	0
Stress-limiting parameter for transverse compression (SLIMC2)	0
Stress-limiting parameter for shear (SLIMS)	0

TABLE 5.3.—COMPARISON OF T700/PR520 FIBER/RESIN TEST AND LS–DYNA SIMULATION AXIAL TENSION DATA

	Axial tensile property[a]	
	Strength, MPa	Modulus, MPa
Test	1050±34	$4.7\times10^4\pm1.1\times10^3$
LS–DYNA	903	5.1×10^4
Error, percent	12	7

[a]Values are shown as an average with ±1 standard deviation.

The axial test results show that the material modulus for the simulation correlates well with the material modulus for the test; however, the strength obtained with the simulation was low compared to the test data. One reason for this discrepancy is that the value chosen for axial strength (XT) was only based on the axial fibers, which is consistent with the assumptions used, and did not take into account the bias fibers. Modifying these assumptions to include the bias layers may have brought the strength to more closely match the test data. Another reason is that the material model used in LS–DYNA was a continuum damage model. Damage could have been occurring in the axial layers leading to a reduced strength in these layers not shown by the test data. Also, interactions between each layer could have been causing localized stress concentrations in the LS–DYNA model that may be not present in the test. However, the model's results show good agreement with the test data in that both response curves show linear behavior until failure.

Figure 5.17 shows the results in the transverse direction. The transverse results also showed good correlation between the test results and the simulation. Table 5.4 shows the comparisons.

The simulations captured the nonlinearities due to damage accumulation in the composite usually encountered with transverse testing. However, the strength values for the simulation were higher than the test. This could have been due in part to the value picked for the transverse strength of the fiber bundle split. More detailed investigations are needed to determine if the first fiber bundle split should be used for the analysis, or if a median value of stress based on the number of fiber bundle splits should be used.

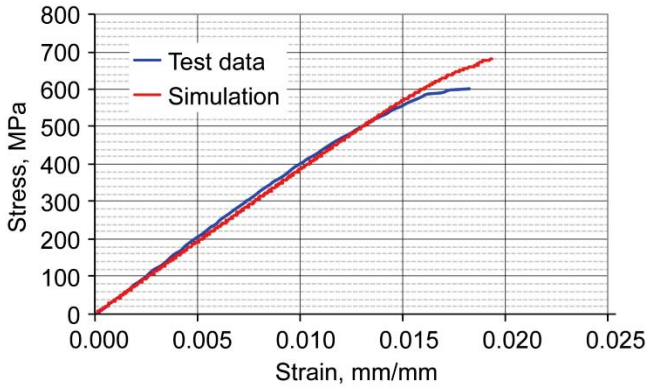

Figure 5.17.—Comparison of test and LS–DYNA simulation transverse tension response for T700/PR520 fiber/resin material.

TABLE 5.4.—COMPARISON OF T700/PR520 FIBER/RESIN TEST AND LS–DYNA SIMULATION TRANSVERSE TENSION DATA

	Transverse tensile property[a]	
	Strength, MPa	Modulus, MPa
Test	$8.69\times10^{4}\pm4.3\times10^{2}$	$4.3\times10^{4}\pm1.6\times10^{3}$
LS–DYNA	647	3.9×10^{4}
Error, percent	8	9

[a]Values are shown as an average with ±1 standard deviation.

5.4.2 T700/E862 Fiber/Resin Material Response

Simulations also were run using the data from the T700/E862 tests. Table 5.5 shows the parameters used in the material model, and Table 5.6 shows the result comparisons between the tests and simulations.

Figure 5.18 shows the material response curves for both the LS–DYNA simulation and an example axial tension test. Good agreement is seen between the simulations and test data. However, one can see that the nonlinearities occurred in the test data, particularly at higher strains. These nonlinearities may have been caused by the delaminations occurring in the composite at higher strains, as discussed in Section 4.4.2.3, "Examination of Subsurface Delaminations." However, because of the limitations in the shell element model formulation, the computer model cannot currently simulate a delamination failure mechanism. However, using the failure data that was obtained from the testing, the model and test data did agree within 10 percent for both the modulus and ultimate strength.

Figure 5.19 shows the transverse material response curves, and Table 5.7 presents a comparison of the data.

TABLE 5.5.—T700/E862 FIBER/RESIN MATERIAL PARAMETERS USED FOR LS–DYNA MODEL

Material parameter name (LS–DYNA name)	Value
Axial modulus (EA), GPa	51.3
Transverse modulus (EB), GPa	25.0
In-plane shear modulus (GAB), GPa	19.0
In-plane Poisson's ratio (PRBA)	0.071
Axial tensile failure strain (E11T)	0.0178
Axial compressive failure strain (E11C)	0.0058
Transverse tensile failure strain (E22T)	0.0144
Transverse compressive failure strain (E22C)	0.0086
In-plane shear failure strain (GMS)	0.0095
Axial tensile stress at failure (XT), MPa	809.4
Axial compressive stress at failure (XC), MPa	320
Transverse tensile stress at failure (YT), MPa	196
Transverse compressive stress at failure (YC), MPa	303
In-plane shear stress at failure (SC), MPa	257
Stress-limiting parameter for axial tension (SLIMT1)	0
Stress-limiting parameter for transverse tension (SLIMT2)	1
Stress-limiting parameter for axial compression (SLIMC1)	0
Stress-limiting parameter for transverse compression (SLIMC2)	0
Stress-limiting parameter for shear (SLIMS)	0

TABLE 5.6.—COMPARISON OF T700/E862 FIBER/RESIN TEST AND LS–DYNA SIMULATION AXIAL TENSION DATA

	Axial tensile property[a]	
	Strength, MPa	Modulus, MPa
Test	807±25	$4.7\times10^{5}\pm1.6\times10^{3}$
LS–DYNA	5.19	5.1×10^{4}
Error, percent	6.8	8.8

[a]Values are shown as an average with ±1 standard deviation.

Because of the large amount of scatter in the strength test data, the average error was over 10 percent; however, if the highest value of strength obtained from testing was used in the comparison, the error was 10 percent. As with the T700/PR520 material system, the transverse strength was again overpredicted by the computer simulation. This data suggested that the value used for the transverse fiber bundle strength was again picked too high. This may have been due in part to the fact that fiber bundle splits could have been occurring within the composite, and therefore were not visible to the measurement system before the fiber bundle splits appeared on the surface. However, as with the tension data, the cumulative error between the tests and simulations was within 10 percent.

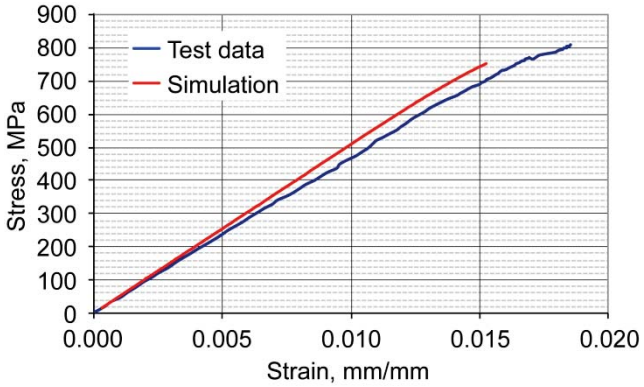

Figure 5.18.—Comparison of test and LS–DYNA simulation axial tension response for T700/E862 fiber/resin material.

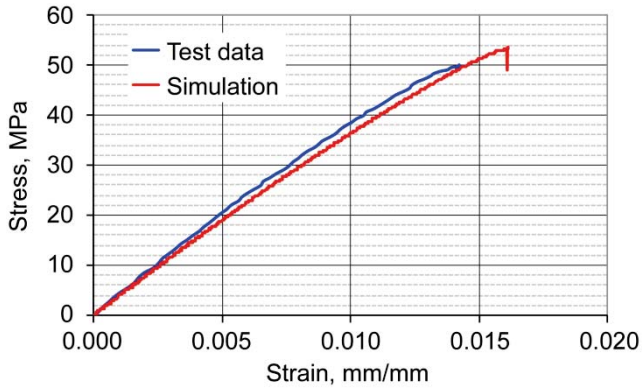

Figure 5.19.—Comparison of test and LS–DYNA simulation transverse tension response for T700/E862 fiber/resin material.

TABLE 5.7—COMPARISON OF T700/E862 FIBER/RESIN TEST AND LS–DYNA SIMULATION TRANSVERSE TENSION DATA

	Transverse tensile property[a]	
	Strength, MPa	Modulus, MPa
Test	460±36.3	$4.1\times10^{4}\pm1.3\times10^{3}$
LS–DYNA	7.7×10^{4}	3.9×10^{4}
Error, percent	14	6.6

[a]Values are shown as an average with ±1 standard deviation.

5.5 Conclusions

This section shows the development of a macromechanical computer model used for the prediction of composite material response. The macromechanical model includes aspects from the composite braid geometry as well as the material property data from test composite materials. Axial and transverse tensile tests have been simulated on two example fiber/resin material systems, T700/E862 and T700/PR520, with stress-strain curves presented. The macromechanical composite computer model predicts the tensile response of the materials to within 10 percent accuracy.

6.0 Triaxial Braided Composite Impact Simulations

As described in Section 1.0, "Introduction," the composite materials presented in this research are primarily going to be used in impact situations, in which the impact resistance of these materials must be known and quantified. This chapter presents preliminary investigations that use the developed composite computer models for impact simulations for the detection and prediction of impact velocity thresholds and failure depictions. Two fiber/resin material systems, which have been extensively investigated in earlier chapters, are going to be used for impact simulations: T700/E862 and T700/PR520. This section will discuss the test setup, composite impact geometry of the finite-element model, the material properties used, and also the rationale for conducting simulations with a soft projectile. It will also show preliminary results for the two material systems and compare to the test data, when available.

6.1 Background

The following sections present background information on the triaxial braided composite testing approach and the LS–DYNA finite-element software utilized in this study.

6.1.1 Material Testing

There has been ongoing research at the NASA Glenn Research Center to efficiently screen different triaxially braided composite material systems for use in containment applications. The screening process involves impacting a triaxially braided composite plate with a soft projectile made of gelatin from a gas gun in the ballistic velocity regime. Gelatin was picked as the projectile because it was an efficient way of transferring a maximum amount of its kinetic energy into strain energy in the composite panel. This process was an effective way in determining the composite material's threshold velocity, which is the lowest velocity at which the projectile penetrated the composite panel. Penetration was established when the gelatin could be seen exiting the back of the composite panel.

The screening process has been partially completed on the four fiber/resin material systems examined and presented earlier: T700/E862, T700/PR520, T700/5208, and T700/3502. However, only the top two performing material systems, T700/E862 and T700/PR520, will be examined in this section to compare threshold velocities and examine differences in material response.

6.1.2 LS–DYNA Introduction

In order to conduct impact simulations for the above-mentioned materials, a commercial finite-element code, LS–DYNA, was utilized. A detailed explanation of LS–DYNA can be found in Reference 73, but a brief summary is presented here for completeness.

LS–DYNA is a commercially available nonlinear transient explicit finite-element code commonly used in impact and crashworthiness applications by the automotive and aerospace industries. The main solver in LS–DYNA uses a central difference explicit time integration to solve transient dynamic impact problems. LS–DYNA has a large material library (>150 material models), much of which is based on constitutive laws developed by researchers, and a robust set of contact laws to handle complex interactions between objects. It is capable of computing traditional structural impact problems in Lagrangian space (used in Sec. 5.0, "Development of Macromechanical Triaxial Braided Composite

Computer Model"), in which the finite-element mesh is fixed to and deforms with the structures, but LS–DYNA also has features which allow it to solve fluid-structure interaction problems (e.g., a structure landing in water) using a combination arbitrary Lagrangian-Eulerian (ALE) meshing technique. The ALE technique will be utilized in the computer models presented for the composite impact problems. In the ALE space, the fluid material (representing the gelatin) is allowed to flow freely and is remapped within the mesh at each time step. Thus, the material exhibits large deformations within the mesh without causing extreme deformations within the elements or time step.

6.2 Finite Element Model Development

The composite impact finite-element model used the same material and section properties that have been described in Section 5.0, a 0.6-m by 0.6-m by 3.18-mm (2-ft by 2-ft by 0.125-in.) panel geometry.

Figure 6.1 shows the geometry of the composite subcell model. The alternating patterns of pink, blue, green, and yellow represent the four subcells used to simulate the composite braid geometry. To simulate the test conditions in an impact test, the four sides of the panel were constrained in all three displacement and all three rotation directions.

Fundamental studies on gelatin impacts were originally done by Wilbeck (Ref. 74). Wilbeck showed that the gelatin material exhibited extreme deformation at the velocities under investigation. For LS–DYNA implementation, because the gelatin was a low-strength, low-stiffness, and high-flow material, it was modeled using a null formulation in which its pressure-volume relation, which simulated the shock wave throughout the gelatin at impact, was modeled using an equation of state relationship. A propriety set of material parameters were used for the gelatin in this study. The gelatin was given an initial velocity (representing the impact velocity from the test), and the run time was set to 2×10^{-3} s, with output results written at 5×10^{-5} s. The finite element model consisted of a total of 243 209 nodes, 16 320 composite shell elements, and 41 040 solid elements for the gelatin formulation. To simulate the contact between the gelatin and the composite, the *CONSTRAINED_LAGRANGE_IN_SOLID contact card was used. The model was run on a single precision version of LS–DYNA 971. Figure 6.2 shows the LS–DYNA model compared to the test setup.

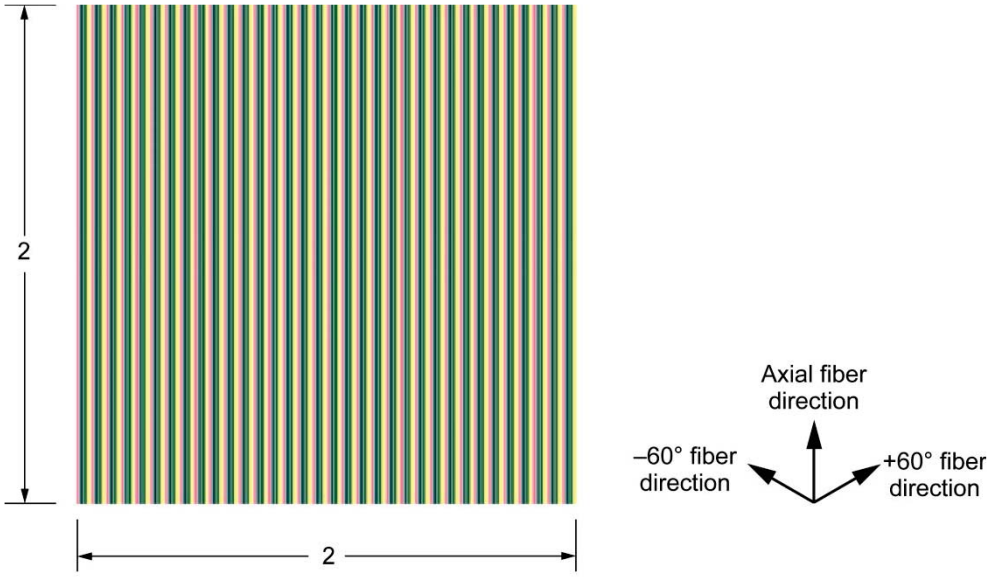

Figure 6.1.—Finite-element triaxial braided model. Dimensions are in feet.

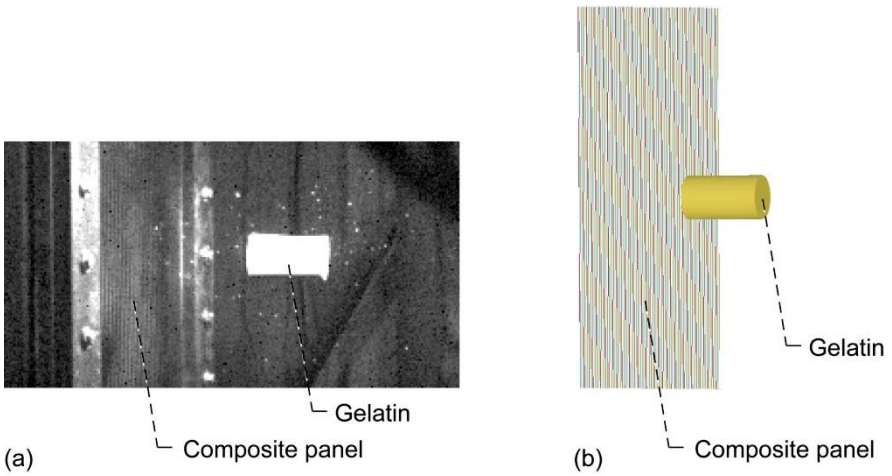

Figure 6.2.—Triaxial braided composite impact. (a) Test setup. (b) Computer model.

Testing was done at the NASA Glenn Research Center Impact Ballistic Lab by NASA personnel and is described in Reference 3. In the test setup, a composite panel was fixed into a steel frame normal to the end of the gas gun barrel. The gelatin was placed in the gun barrel such that the longitudinal axis of the gelatin projectile was in the direction of flight, and the flat end made contact with the composite panel. Calibrated high-speed cameras were used to track and measure the gelatin's position and velocity before impact. This velocity measurement was the number used when determining an impact threshold velocity, and also when correlating simulation speeds to test speeds. The optical measurement system was also used on the nonimpacting side of a subset of the composite panels tested. The optical measurement system measured maximum out-of-plane deflection as well as axial and transverse surface strains on the panel. These measurements, along with the failure patterns were the main parameters compared to the simulations.

6.3 Simulation Results

The penetration threshold for the simulations of the material system was determined by examining the lowest velocity causing element failure in the model. Element failure occurred when all of the integration points in the element (representing each of the different fiber layers) failed. However, if only a partial number of the layers failed, the element remained in the model. These partially failed elements contained a reduced modulus because the failed layers did not contribute to the overall stiffness in the element.

For T700/E862, the lowest velocity that caused element failure, and thus was the penetration threshold, was 143 m/s (470 ft/s). Figure 6.3 depicts these results with part (a) showing containment at (140 m/s) 460 ft/s and part (b) showing results from a 143 m/s impact velocity, which depicts penetration.

A pressure wave can be seen in both parts of Figure 6.3. Figure 6.3(b), shows element failure. The failure depicted shows that the composite panel opened both along the axial fiber direction (global y in the figure) and transversely to the axial fiber direction (global x in the figure). This failure depicts the composite behaving more as a quasi-isotropic material, which was primarily caused by the inclusion of the fiber shifting phenomena into the model. However, the failure data cannot be validated because, at the time of this writing, no test data exists at the penetration threshold of this particular material system.

At the time of this writing, the only two test data points available for T700/E862 were at 141 m/s (463 ft/s) and at a much higher 226 m/s (741 ft/s). The T700/E862 test data showed containment when tested at 141 m/s and showed penetration for 226 m/s. The LS–DYNA results fell within this band and agreed with these results. The LS–DYNA was also run at 226 m/s to compare the failure results.

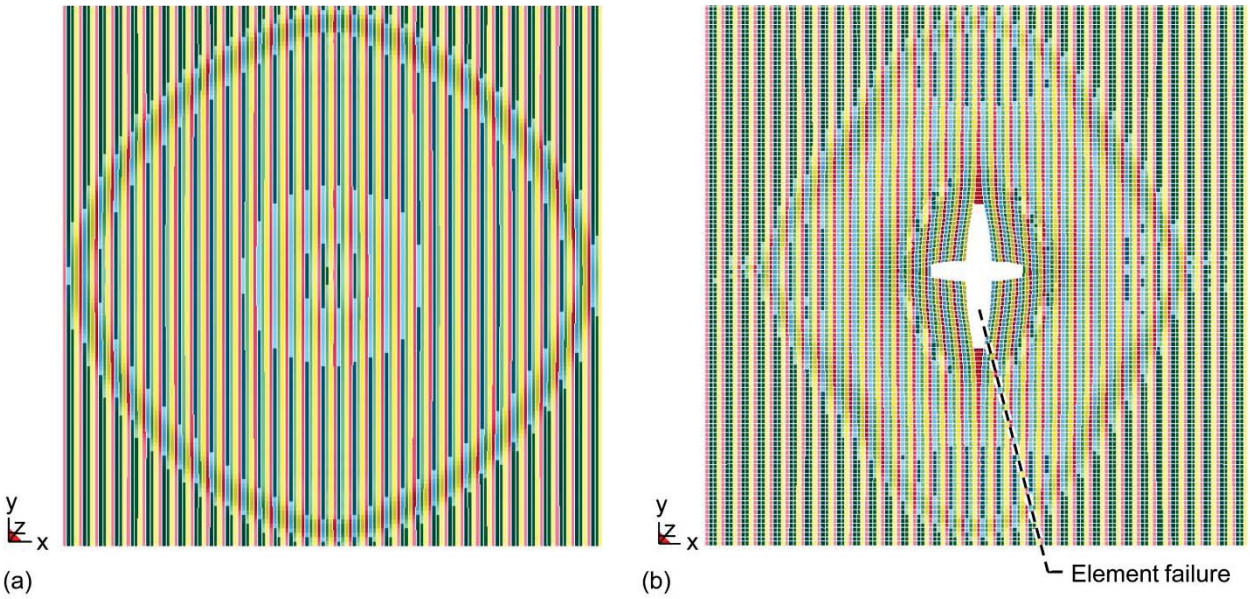

Figure 6.3.—Finite element model comparisons showing T700/E862 fiber/resin impact at different velocities. (a) 140 m/s (460 ft/s). (b) 143 m/s (470 ft/s).

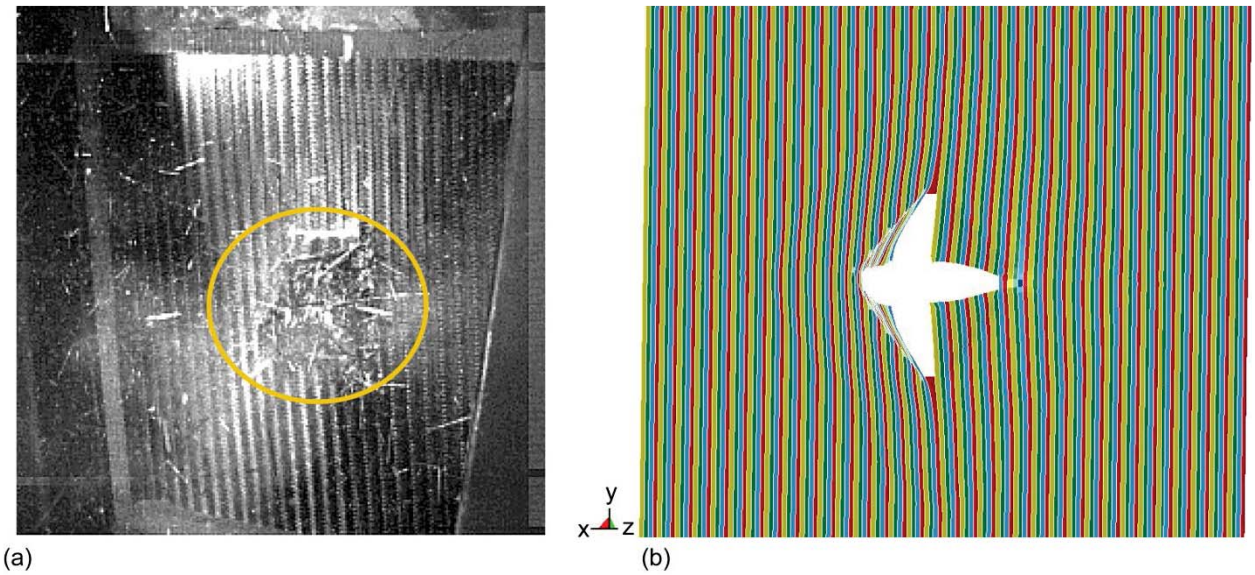

Figure 6.4.—Comparison of experimental and LS–DYNA simulation impact failure for T700/E862 fiber/resin composite panel at 626 m/s (741 ft/s). (a) Test. (b) Simulation.

Figure 6.4 compares the failures of the T700/E862 composite panel at 226 m/s. Note that the test picture presented is at a 45° off-axis angle to the rear of the panel. The simulation picture in Figure 6.4(b) has attempted to emulate this view. The test data shows a penetration by hole in the middle of the panel (circled). This hole was also present in the computer simulation, which can be seen in Figure 6.4(b), which mimicked the failure in Figure 6.3(b).

Similarly, the LS–DYNA models were run for T700/PR520. Two data points were available from the testing of the T700/PR520 composite panels; the first test showed containment below threshold at 186 m/s (609 ft/s), and the second test showed penetration at 194 m/s (637 ft/s). The computer model predicted a

penetration velocity threshold of 192 m/s (630 ft/s), which agreed well with the test data. Since the optical measurement system was also used on the impacted panels, items such as maximum out-of-plane deflection and axial and transverse strains at failure were compared between the test data and simulation.

Comparisons were first done for the velocity of 186 m/s, which was below the penetration threshold. The simulation predicted a maximum out-of-plane deflection of 4 cm (1.57 in.) in the middle of the panel, whereas the test data obtained from the optical measurement system showed that the actual deflection was 4.3 cm (1.68 in.). The axial strains in the middle of the panel were compared next. The maximum values obtained from the test data were 1.67 and 1.49 percent for the global axial and transverse strains, respectively. The simulation showed that the maximum axial strain value was 1.74 percent and the transverse strain value was 1.75 percent.

Figure 6.5 shows the comparisons between the test and simulation at the time in which the maximum axial strain occurred. Both images show very low far-field strain. The simulation accurately reflects the concentration seen in the impact location. The next item to note is that both pictures show a concentrated area of high strain in the middle of the panel, which is in the impact location. One difference between the pictures is that whereas the test data show concentric circles of gradually increasing strain, the simulation shows a small oval of concentrated strain in the center. This difference could be attributed to one main reason: the resolution on the test data is not great enough to capture the highly localized areas of strain seen in the simulation because of the limitations in camera speed resolution. However, for the results on maximum out-of-plane deflection and axial and transverse strains, there were good correlations between the test data and simulation results.

Next, comparisons were done between the test and simulation data above the penetration velocity threshold. The simulation was run with the gelatin projectile having a velocity of 194 m/s to match with the test, and only comparisons in the failure shapes were done. Items such as failure strain and maximum out-of-plane deflection were not able to be compared because of the removal of the elements for the simulation and distortions of the dot pattern for the test in the regions in question. Figure 6.6 compares the failures shape of the composite panels.

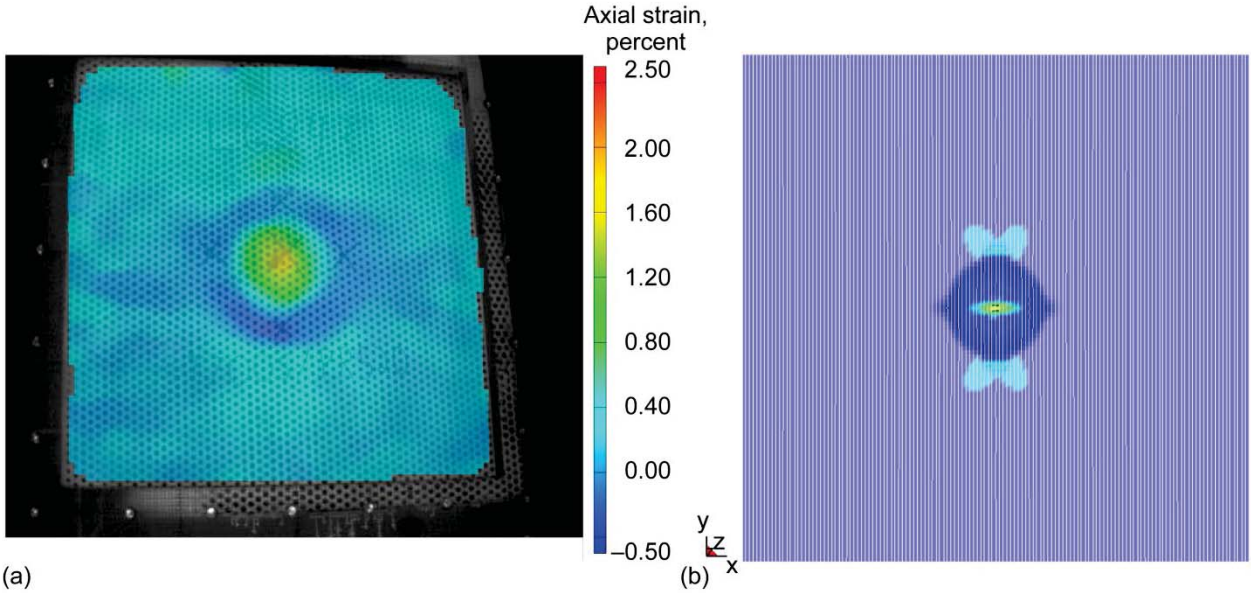

Figure 6.5.—Comparison of measured and LS–DYNA simulated axial strain behavior for T700/PR520 fiber/resin composite impact at 186 m/s (609 ft/s). (a) Test measurement. (b) Simulation.

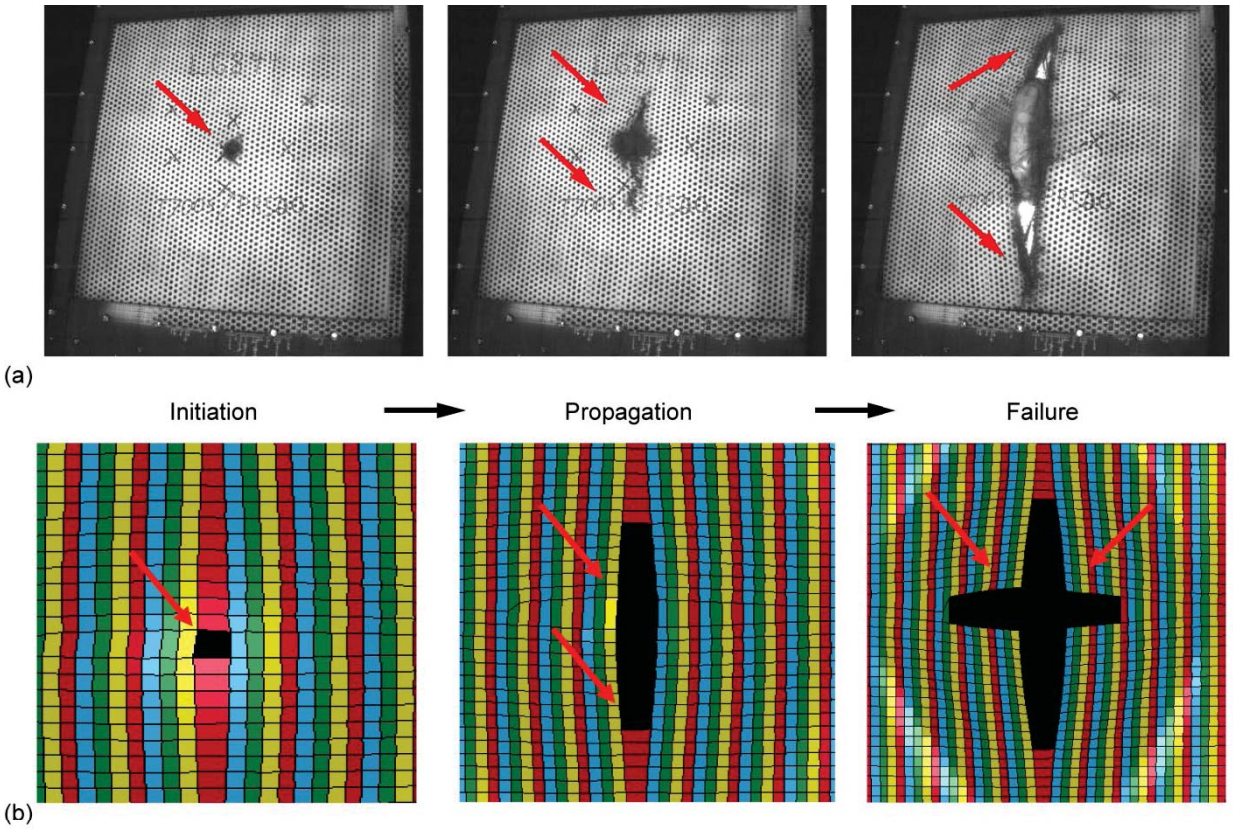

Figure 6.6.—Progression of failure in T700/PR520 fiber/resin material system under impact at 194 m/s (637 ft/s). (a) Test. (b) LS–DYNA simulation.

Examining the test data, the initiation of the failure occurred in the middle of the panel. The failure propagated in the vertical direction, parallel to the axial fibers, and the panel failed when the propagation reached the boundaries. This failure showed the panel "unzipping," or transversely failing, along the axial fiber direction. The simulation results match both the initiation and propagation of the failure, but differed in the final failed picture. In the simulation, the failure initiated in the middle of the panel. It then progressed in the vertical direction, parallel to the axial fibers; however, by the time the panel failure occurred, there were both axial and transverse failures. The axial failures occurred in the horizontal direction to the left and right of the middle of the panel, and caused the final "diamond" shape to occur in the failed panel.

Limited examinations were able to be conducted on some of the failed elements in the model. The time history of the axial strain was further examined for the first failed element in the middle of the panel.

Figure 6.7 shows the axial strain time history for an element in the middle of the composite model. Notice that the failure occurs when the E11T parameter is reached. Since the failure occurred between the two points in which the output results were written (between 5.0×10^{-4} and 5.5×10^{-4} s), the result can be assumed to be between the two. Since the SLIMT1 parameter is set to 0 in the model, the element immediately fails and the load-carrying capacity of the element goes to 0.

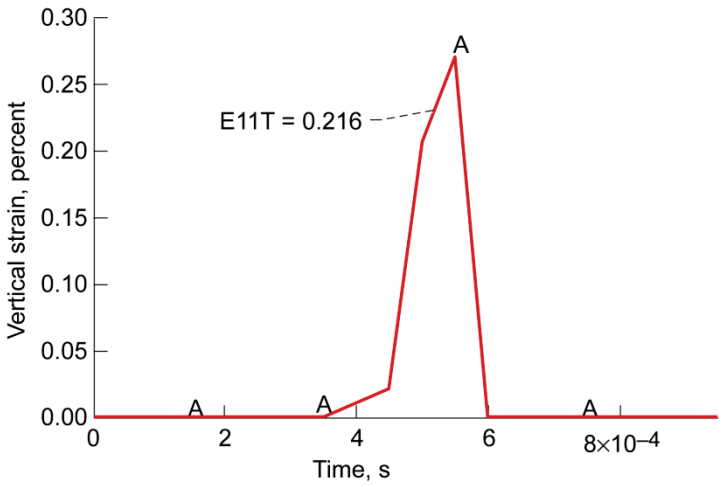

Figure 6.7.—Axial strain time history during impact at 194 m/s (637 ft/s) for T700/PR520 fiber/resin composite panel's midpoint; strain at axial tensile strength E11T is identified.

Both of the material systems examined in this research show failures different from what was reported by Cheng (Ref. 67). Cheng saw a "barn door" failure, which was represented by a transverse failure occurring in the middle of impacted region, with failures in the bias fiber direction leading toward the sides of the panel. The differences in failure modes can be attributed to a variety of factors, with the main one being that the fiber shifting was employed in this composite model to account for the real composite layups seen in the digital microscopic imaging, as shown in Sections 4.0 and 5.0. The fiber shifting made the composite material behave as a quasi-isotropic material much more than by stacking layers of subcells on top of each other. Another main difference is that Cheng examined different material systems than the ones examined for this study, which could affect the panel's material responses greatly. Finally, whereas measured material properties are used in this model development, Cheng employed classical mechanics of composite materials models to obtain the effective unidirectional properties for the model, which may have led to some inaccuracies in material property determination.

6.4 Conclusions

Conclusions drawn from the impact simulations presented in this chapter are limited because of the lack of test data for the materials. Using the measured material properties for the static models originally presented in Section 5.0, simulations were conducted on the two highest strength material systems under impact loading. The results show that for the T700/E862 fiber/resin material system, the threshold velocities and failure depictions for the simulations did agree with the test data that were available.

Because there was a defined threshold for the T700/PR520 material system, more extensive investigations were conducted. The T700/PR520 simulation predicted a penetration threshold of 192 m/s (630 ft/s), which was in good agreement with the 194 m/s (637 ft/s) penetration threshold measured in testing. When examining the out-of-plane displacement and strains for the simulation below the penetration threshold, results also matched up well with the test data. Finally, when comparing the failure surface above threshold, the simulation predicted the initiation and propagation well, but did not match the final failed shape.

7.0 Concluding Remarks

The research presented in this report presents investigations into the nature of triaxial braided composite material response and composite constituent response with implementations into finite-element computer models for simulation.

7.1 Summary of Results

The work is summarized here to remind the reader of the important points demonstrated throughout the research.

Section 3.0, "Investigations Into Composite Constituent Material Response," proposed a unique way to measure the mechanical response of matrix materials used in triaxial braided composites with an optical measurement system using unique, nonstandard specimen geometries. Utilizing the test method presented, tension, compression, and shear results for pure load-to-failure and load-unload-reload tests were obtained on an example material for a variety of strain rates and temperatures. The results showed that the resin is both rate and temperature dependent for all of the loading conditions. The results also show the effects of hydrostatic stress when examining the differences between the tensile and compressive results as well as a damage accumulation, represented by a reduced modulus on the unloading portion of the load-unload curve. The results obtained were important because many resin constitutive models in development need all of the data acquired in this report, but also provide a first insight to the rate and temperature dependence of the material.

In Section 4.0, "Investigations of Triaxial Braided Composite Material Response," the material properties for four example composite material systems were determined. As with the resin testing, optical measurement techniques were used to measure the triaxial braided composite material response. By using this method, the nature of each different material system's microscale and macroscale behavior was categorized and quantified. The optical measurement technique was able to obtain global stress versus strain material response curves, and also able to identify local failure mechanisms present within the different composite material systems, which led to the differences in the global material response curves. The results led to the conclusion that there were different damage mechanisms affecting the material properties.

For the composite testing in the axial tensile direction, the load transfer between the loaded axial fibers and bias fibers accounted for the surface bias fiber bundle splits that occurred and were captured by the optical measurement system. The fiber bundle splits in the bias fibers caused strain concentrations in the axial fiber bundles, which led to the axial fibers failing prematurely, causing a reduced strength in the material. Also, the results showed that the nonlinearities seen in the global axial material response curves were a result of damage in the form of subsurface delaminations, which were previously very difficult to be measured in situ.

In the transverse tensile direction, since there were no continuous fibers extending throughout the entire gage section, the resin played a major role in the material response. The main damage-causing mechanism was the fiber bundle splitting that occurred in the axial fibers. Failure in the transverse tests was a result of edge delaminations that occurred and quickly propagated along the bias fibers.

All of the characteristics described above led to the ultimate failure in the composite specimens; however, the results indicate that differences in the fiber-matrix interface properties allowed for the specimens to fail at different strain levels. The data show that the T700/PR520 fiber/resin material system had the strongest interface, and the T700/3502 system had the weakest interface.

In compression, the stronger two material systems exhibited inelastic behavior prior to failure. This inelastic behavior occurred because the fiber-matrix interface was sufficiently strong enough to hinder the microbuckling phenomena. The two weaker material systems exhibited microbuckling, which occurred because the weak fiber-matrix interface was not strong enough to hold the fiber bundles together under the compressive loading.

Shear testing showed that a modified ASTM specimen design was viable for use in the collection of shear data. The modified specimen design allowed for a uniform region of high strain in the gage section and between the grips. Under shear loading, specimens did not exhibit fiber bundle splitting or other microscopic failures; rather, the specimens failed catastrophically when the ultimate strain was reached.

Along with being an integral tool in determining and quantifying material response properties for the composite material systems investigated, the data obtained from the optical measurement system were also used for developing a finite-element-based analytical model to simulate the responses of the triaxial braided composites.

In Sections 5.0, "Development of Macromechanical Triaxial Braided Composite Computer Model," and 6.0, "Triaxial Braided Composite Impact Simulations," a triaxially braided finite-element-based analytical computer model was created and utilized to simulate the static and impact response of composite coupons and panels. The computer model simulates the braid geometry by dividing the unit cell into four subcells and stacking the layers of braid using a novel through-thickness integration technique. The properties needed for the material model were obtained from the coupon tests performed using the optical measurement data and classical composite micromechanics techniques. The created computer model predicted strength and stiffness to within 10 percent error for the static tests and predicted a ballistic penetration threshold consistent with data available from impact tests.

Generalizing, the work presented can provide a more fundamental understanding of braided composite materials. The nature of the resin matrix testing allows for insight into the main rate-dependent behavior of the composite materials, while also giving preliminary predictions about strength and stiffness in the finished composite material system. Secondly, by using both the constituent and composite test data acquired, a greater understanding of the role of the resin, interface, and fiber properties can be gained. Finally, by collecting all of the data from the composite and resin matrix, computer models can ultimately be developed that can give a more accurate prediction on static and impact strength by including the rate dependence of the resin while also using some of the microscopic failure parameters seen in the finished composites.

Even though the scope of this work is limited to one material for the constitutive testing and four material systems for the composite testing, the methods described can be used on any type of fiber or matrix for use in other triaxial braided composite material systems. The methods developed can be used on a wide range of material systems to determine the composite constituent properties, the composite macroscopic response material response, and also microscopic failure properties that affect the macroscopic response.

Finally, the computer model and method for implementation of the composite properties can be generalized to include any number of fiber layers, any fiber angle, and thicknesses with relative ease without changing the methodology developed.

7.2 Future Work

The methods and data presented in this work provide a fundamental basis for understanding the behavior of triaxial braided carbon fiber composites. However, this work is not a conclusive end to an understanding in these materials. The reader is reminded that work is ongoing and must still be done to fully understand the complex nature of these materials.

7.2.1 Constituent Testing

The test method described in Section 3.0 describes an efficient method for testing the composite matrix constituent under a variety of loading rates and temperatures. Example results have been presented on one example matrix material, Epon 862 resin (Momentive Specialty Chemicals, Inc.). However, for composite materials made with other matrix materials, other materials must be tested as well. There is work in progress as of this writing to use the test method on a second composite matrix material of interest, Hexcel's 3502.

7.2.2 Composite Testing

Although the work presented in Section 4.0 gives insights into the nature of composite material response, future work can expand on these issues. For example, only rectangular ASTM 3039 specimens were used for the testing in this report. The results in Section 4.4.2.2 showed that areas of low strain occurred on the edges of the transverse specimens, indicating that these edge areas did not contribute significantly to the overall composite material response. Alternative specimen designs should be investigated to remedy this problem. One idea would be to use a notched specimen in which continuous bias fibers extend throughout the entire gage section. Bowman, et al. (Ref. 63) have briefly investigated this problem by proposing notched "bowtie" specimens and have presented material response curves on similar materials; however, the optical measurement technique to collect the strain data was not used so full-field results were not available. Also, a braided tubular specimen design that has no terminating fibers in its gage section would be an ideal specimen design, although the complexity in the fabrication of this specimen design makes it the most undesirable to manufacture.

Next, the work in this research presents fabricated composite panels having a thickness of 3.18 mm (0.125 in.) and six layers of the braided preform through the thickness. In order to investigate failure mechanisms such as fiber bundle splitting and fiber-resin matrix interaction, tests could also be done on one layer of fabricated braid, such that interactions between the braided preform layers are removed. Also, testing one layer of braid will validate assumptions made in the composite modeling section.

Also, only in-plane testing (tensile, compression, and shear) was done for the materials studied. However, when composite materials undergo impact loading, out-of-plane deformation is generally the main item of interest. Knowing this, out-of-plane testing such as three-point-bending tests (e.g., ASTM D2234 (Ref. 75)) should be examined to see if items such as failure strain and transverse fiber bundle failures can be examined.

Finally, as the test method and analysis technique presented quantifies composites mainly under static loading with limited implementations into the dynamic regime, ballistic impact testing using full-field optical measurement techniques must be performed to gain insight into the nature of items such as transverse fiber bundle failure and other mechanisms occurring in the ballistic range. Once ballistic testing has been completed on a variety of materials under a variety of test conditions, the finite-element models can be modified using the ballistic data to better predict impact response.

7.2.3 Composite Modeling

The analytical approach to composite modeling is a first step in trying to develop a macromechanical composite finite-element model using composite test data. Once some of the above tests have been completed, the finite-element model can be adjusted to incorporate the new test data. Also, although the finite element model uses data such as transverse fiber bundle failures, when looking at the composite material response simulations, the fiber bundle splits do not appear because of the nature of the large mesh size. Also, fiber bundle layer delaminations were examined in both the axial and transverse tensile tests; however, the model cannot predict the delaminations, because shell elements cannot predict items such as transverse shear failures. However, the shell element model can be expanded to include either an explicit interface layer (with its own material properties, which must be found using a combination of the above-mentioned tests) or use some more advanced techniques to determine if integration layers in the model can be adjusted to include delaminations. One potential mechanism that has been investigated by Tabiei (Ref. 76, LS–DYNA Composite Materials Training Course) is to use a *CONTACT_TIEBREAK_... LS-DYNA parameter to simulate the delaminations between layers. However, as of this writing, the *CONTACT_TIEBREAK command in LS–DYNA can only be used between stacked shell elements and not between integration layers.

Finally, investigations must be done to examine the differences between the failure shapes for the impact simulations. While the numbers used in the material model for simulation lead to good correlation between the tests and simulations, they may need to be adjusted to incorporate the impact data. Because

the finished composite material will be rate dependent, as shown with the resin data, some of the numbers gained from the static testing used may be deficient for the implementation into the impact regime.

References

1. Boeing: Boeing 787 Dreamliner Program Fact Sheet, 2008. http://www.boeing.com/commercial/787family/programfacts.html Accessed Mar. 8, 2013.
2. Federal Aviation Administration: Blade Containment and Rotor Unbalance Tests, FAR 33.94, 1984.
3. Roberts, Gary D., et al.: Impact Testing and Analysis of Composites for Aircraft Engine Fan Cases. NASA/TM—2002-211493, 2002. http://ntrs.nasa.gov/
4. Goldberg, Robert K.; Roberts, Gary D.; and Gilat, Amos: Implementation of an Associative Flow Rule Including Hydrostatic Stress Effects Into the High Strain Rate Deformation Analysis of Polymer Matrix Composites. NASA/TM—2003-212382, 2003. http://ntrs.nasa.gov/
5. Ward, I.M.: Mechanical Properties of Solid Polymers. Second ed., John Wiley & Sons, Chichester, 1983.
6. Bordonaro, Christine Marie: Rate Dependent Mechanical Behavior of High Strength Plastics: Experiment and Modeling. Ph.D. Dissertation, Rensselaer Polytechnic Institute, 1995.
7. Goldberg, Robert K.: Strain Rate Dependent Deformation and Strength Modeling of a Polymer Matrix Composite Utilizing a Micromechanics Approach. NASA/TM—1999-209768, 1999. http://ntrs.nasa.gov/
8. Karim, Mohammed R.; and Hoo Fatt, Michelle S.: Rate-Dependent Constitutive Equations for Carbon Fiber-Reinforced Epoxy. Polym. Compos., vol. 27, no. 5, 2006, pp. 513–528.
9. ASTM Standard D638: Standard Test Method for Tensile Properties of Plastics. ASTM International, West Conshohocken, PA, 2004. www.astm.org. Accessed Mar. 8, 2013.
10. ASTM Standard E2207: Standard Practice for Strain-Controlled Axial-Torsional Fatigue Testing With Thin-Walled Tubular Specimens. ASTM International, West Conshohocken, PA, 2002. www.astm.org. Accessed Mar. 8, 2013.
11. Frantz, C.E.; Follansbee, P.S.; and Wright, W.T.: Experimental Techniques with the Split Hopkinson Pressure Bar. Proceedings of the 8th International Conference on High Energy Fabrication. ASME, New York, NY, 1984, pp. 229–236.
12. Gilat, Amos; Goldberg, R.K.; and Roberts, D. Gary: Experimental Study of Strain-Rate-Dependent Behavior of Carbon/Epoxy Composite. Compos. Sci. Technol., vol. 62, nos. 10–11, 2002, pp. 1469–1476.
13. Liang, Y.-M.; and Liechti, K.M.: On the Large Deformation and Localization Behavior of an Epoxy Resin Under Multiaxial Stress States. Int. J. Solids Struct., vol. 33, no. 10, 1996, pp. 1479–1500.
14. Behzadi, S.; and Jones, F.R.: Yielding Behavior of Model Epoxy Matrices for Fiber Reinforced Composites: Effect of Strain Rate and Temperature. J. Macromol. Sci. Phys., pt. B, vol. 44, issue 6, 2005, pp. 993–1005.
15. Kontou, E.: Viscoplastic Deformation of an Epoxy Resin at Elevated Temperatures. J. Appl. Polym. Sci., vol. 101, no. 3, 2006, pp. 2027–2033.
16. Buckley, C.P., et al.: Deformation of Thermosetting Resins at Impact Rates of Strain. Part I: Experimental Study. J. Mech. Phys. Solids, vol. 49, no. 7, 2001, pp. 1517–1538.
17. ASTM Standard D3039: Standard Test Method for Tensile Properties of Polymer Matrix Composite Materials. ASTM International, West Conshohocken, PA, 2000. www.astm.org. Accessed Mar. 8, 2013.
18. ASTM Standard D3410: Standard Test Method for Compressive Properties of Polymer Matrix Composite Materials With Unsupported Gage Section by Shear Loading. ASTM International, West Conshohocken, PA, 2003. www.astm.org. Accessed Mar. 8, 2013.

19. ASTM Standard D6484: Standard Test Method for Open-Hole Compressive Strength of Polymer Matrix Composite Laminates. ASTM International, West Conshohocken, PA, 2004. www.astm.org. Accessed Mar. 8, 2013.
20. ASTM Standard D5379: Standard Test Method for Shear Properties of Composite Materials by the V-Notched Beam Method. ASTM International, West Conshohocken, PA, 2005. www.astm.org. Accessed Mar. 8, 2013.
21. ASTM Standard D3518: Standard Test Method for In-Plane Shear Response of Polymer Matrix Composite Materials by Tensile Test of a ±45° Laminate. ASTM International, West Conshohocken, PA, 1994. www.astm.org. Accessed Mar. 8, 2013.
22. Tsotsis, Thomas K., et al.: Towards Rapid Screening of New Composite Matrix Resins. Compos. Sci. Technol., vol. 66, nos. 11–12, 2006, pp. 1651–1670.
23. The Composite Materials Handbook. MIL−HDBK−17−1F, vol. 1, ASTM International, West Conshohocken, PA, 2002.
24. Tomblin, J., et al.: Material Qualification Methodology for 2X2 Biaxially Braided RTM Composite Material Systems. AGATE–WP3.3–033048–116, 2001.
25. Tomblin, John S.; Ng, Yeow, C.; and Raju, K. Suresh: Material Qualification and Equivalency for Polymer Matrix Composite Material Systems: Updated Procedure. DOT/FAA/AR–03/19, 2003. Available from the National Technical Information Service.
26. Masters, John E., et al.: The Effects of Specimen Width on Tensile Properties of Triaxially Braided Textile Composites. NASA CP–3178, vol. I, pt. 2, 1992, pp. 523–536. http://ntrs.nasa.gov/
27. Masters, John E., et al.: Mechanical Properties of Triaxially Braided Composites: Experimental and Analytical Results. J. Compos. Technol. Res., vol. 15, no. 2, 1993.
28. Masters, John E.: Strain Gage Selection Criteria for Textile Composite Materials. NASA CR–198286, 1996. http://ntrs.nasa.gov/
29. Masters, John E.; and Portanova, Marc A.: Standard Test Methods for Textile Composites. NASA CR–4751, 1996. http://ntrs.nasa.gov/
30. Masters, John E.; and Ifju, Peter G.: Phenomenological Study of Triaxially Braided Textile Composites Loaded in Tension. Compos. Sci. Technol., vol. 56, no. 3, 1996, pp. 347–358.
31. Grediac, Michel: The Use of Full-Field Measurement Methods in Composite Material Characterization: Interest and Limitations. Compos. Part A Appl. Sci. Manuf., vol. 35, nos. 7–8, 2004, pp. 751–761.
32. Gliesche, Konrad; Hubner, Tamara; and Orawetz, Holger: Investigations of In-Plane Shear Properties of ±45°-Carbon/Epoxy Composites Using Tensile Testing and Optical Deformation Analysis. Compos. Sci. Technol., vol. 65, no. 2, 2005, pp. 163–171.
33. Hale, R.D.: An Experimental Investigation Into Strain Distribution in 2D and 3D Textile Composites. Compos. Sci. Technol., vol. 63, no. 15, 2003, pp. 2171–2185.
34. Fergusson, A.D., et al.: Flexural Testing of Composite Sandwich Structures With Digital Speckle Photogrammetry. Appl. Mech. Mater., vols. 5–6, 2006, pp. 135–144.
35. Drzal, L.T.; Herrera-Franco, P.J.; and Ho, H.: Fiber-Matrix Interface Tests. Comprehensive Composite Materials, A. Kelley and C. Zweben, eds., vol. 5, Elsevier, Amsterdam, 2000, pp. 71–112.
36. Madhukar, Madhu S.; and Drzal, Lawrence T.: Fiber-Matrix Adhesion and Its Effect on Composite Mechanical Properties. II. Longitudinal (0°) and Transverse (90°) Tensile and Flexure Behavior of Graphite/Epoxy Composites. J. Compos. Mater., vol. 25, no. 8, 1991, pp. 958–991.
37. Madhukar, Madhu S.; and Drzal, Lawrence T.: Fiber-Matrix Adhesion and Its Effect on Composite Mechanical Properties. III. Longitudinal (0°) Compressive Properties of Graphite/Epoxy Composites. J. Compos. Mater., vol. 26, no. 3, 1992, pp. 310–333.
38. Haselbach, W.; and Lauke, B.: Acoustic Emission of Debonding Between Fibre and Matrix to Evaluate Local Adhesion. Compos. Sci. Technol., vol. 63, no. 15, 2003, pp. 2155–2162.

39. Todoroki, Akira; and Tanaka, Yuuki: Delamination Identification of Cross-Ply Graphite/Epoxy Composite Beams Using Electric Resistance Change Method. Compos. Sci. Technol., vol. 62, no. 5, 2002, pp. 629–639.
40. Hoecker, F., et al.: Effects of Fiber/Matrix Adhesion on Off-Axis Mechanical Response in Carbon-Fiber/Epoxy-Resin Composites. Compos. Sci. Technol., vol. 54, no. 3, 1995, pp. 317–327.
41. Christensen, R.M.: Mechanics of Composite Materials. John Wiley & Sons, New York, NY, 1979.
42. Tan, P.; Tong, L.; and Steven, G.P.: Modelling for Predicting the Mechanical Properties of Textile Composites—A Review. Compos. Part A: Appl. Sci. Manuf., vol. 28, no. 11, 1997, pp. 903–922.
43. Raju, I.S.; and Wang, J.T.: Classical Laminate Theory Models for Woven Fabric Composites. J. Compos. Technol. Res., vol. 16, no. 4, 1994, pp. 289–303.
44. Byun, Joon-Hyung: Analytical Characterization of 2–D Braided Textile Composites. Compos. Sci. Technol., vol. 60, no. 5, 2000, pp. 705–716.
45. Tanov, R.; and Tabiei, A.: Computationally Efficient Micromechanical Models for Woven Fabric Composite Elastic Moduli. J. Appl. Mech., vol. 68, issue 4, 2001, pp. 553–561.
46. Donadon, Mauricio V., et al.: A 3–D Micromechanical Model for Predicting the Elastic Behaviour of Woven Laminates. Compos. Sci. Technol., vol. 67, nos. 11–12, 2007, pp. 2467–2477.
47. Huang, Zheng Ming: Unified Micromechanical Model for the Mechanical Properties of Two Constituent Composite Materials. Part I: Elastic Behavior. J. Thermoplast. Compos. Mater., vol. 13, no. 4, 2000, pp. 252–271.
48. Ishikawa, Takashi; and Chou, Tsu-Wei: Elastic Behavior of Woven Hybrid Composites. J. Compos. Mater., vol. 16, 1982, pp. 2–19.
49. Dano, Marie-Laure; Gendron, Guy; and Picard, Andre: Mechanical Behavior of Triaxial Woven Fabric Composite. Mech. Compos. Mater. Struct., vol. 7, no. 2, 2000, pp. 207–224.
50. Pastore, Christopher M.; and Gowayed, Yasser A.: Self-Consistent Fabric Geometry Model: Modification and Application of a Fabric Geometry Model to Predict the Elastic Properties of Textile Composites. J. Compos. Technol. Res., vol. 16, no. 1, 1994, pp. 32–36.
51. Subramanian, Suresh; Reifsnider, Kenneth L.; and Stinchcomb, Wayne, W.: Tensile Strength of Unidirectional Composites: The Role of Efficiency and Strength of Fiber-Matrix Interface. J. Compos. Technol. Res., vol. 17, no 4, 1995, pp. 289–300.
52. Sun, Huiyu; and Pan, Ning: Mechanical Characterization of the Interfaces in Laminated Composites. Compos. Struct., vol. 74, no. 1, 2006, pp. 25–29.
53. Xie, De, et al.: Discrete Cohesive Zone Model to Simulate Static Fracture in 2D Triaxially Braided Carbon Fiber Composites. J. Compos. Mater., vol. 40, no. 22, 2006, pp. 2025–2046.
54. Tsai, J.H.; Patra, A.; and Wetherhold, R.: Finite Element Simulation of Shaped Ductile Fiber Pullout Using a Mixed Cohesive Zone/Friction Interface Model. Compos. Part A Appl. Sci. Manuf., vol. 36, no. 6, 2005, pp. 827–838.
55. Chen, C.M.; and Kam, T.Y.: Elastic Constants Identification of Symmetric Angle-Ply Laminates Via a Two-Level Optimization Approach. Compos. Sci. Technol., vol. 67, nos. 3–4, 2007, pp. 698–706.
56. Ng, Yeow-Cheong: Deriving Composite Lamina Properties From Laminate Properties Using Classical Lamination Theory and Failure Criteria. J. Compos. Mater., vol. 39, no. 14, 2005, pp. 1295–1306.
57. Goldberg, Robert K., et al.: Approximation of Nonlinear Unloading Effects in the Strain Rate Dependent Deformation Analysis of Polymer Matrix Materials Utilizing a State Variable Approach. J. Aerosp. Engrg., vol. 21, 2008, pp. 119–131.
58. GOM: Optical Measuring Techniques. 2008. www.gom.com Accessed Nov. 18, 2008.
59. GOM: ARAMIS Users Manual v 6., 2007.
60. Baer, E.; Hiltner, A.; and Keith, H.D.: Hierarchical Structure in Polymeric Materials. Science, vol. 235, no. 4792, 1987, pp. 1015–1022.

61. ASTM Standard D3171: Standard Test Methods for Constituent Content of Composite Materials. ASTM International, West Conshohocken, PA, 2006. www.astm.org. Accessed Nov. 14, 2008.
62. Lee, J.; and Soutis, C.: A Study on the Compressive Strength of Thick Carbon Fibre-Epoxy Laminates. Compos., Sci. Technol., vol. 67, no. 10, 2007, pp. 2015–2026.
63. Bowman, C.L, et al.: Mechanical Properties of Triaxial Braided Carbon/Epoxy Composites. NASA Document ID 20040112004, 2003. http://ntrs.nasa.gov/
64. Foley, Gary E.; Roylance, Margaret; and Houghton, William W.: Use of Torsion Tubes to Measure In-Plane Shear Properties of Filament-Wound Composites. Test Methods and Design Allowables for Fibrous Composites, vol. 2, ASTM STP–1003, C.C. Chamis, ed., American Society for Testing and Materials, Philadelphia, PA, 1989, pp. 208–223.
65. Melis, Matthew, et al.: Reinforced Carbon-Carbon Subcomponent Flat Plate Impact Testing for Space Shuttle Orbiter Return to Flight. NASA/TM—2007-214384, 2007. http://ntrs.nasa.gov/
66. LSTC: LS–DYNA Keyword Manual. Vol. 971, 2007. http://lstc.com/pdf/ls-dyna_971_manual_k.pdf Accessed May 29, 2013.
67. Cheng, Jingyun: Material Modeling of Strain Rate Dependent Polymer and 2D Tri-Axially Braided Composites. Ph.D. Dissertation, University of Akron, 2006.
68. Matzenmiller, A.; Lubliner, J.; and Taylor, R.L.: Constitutive Model for Anisotropic Damage in Fiber-Composites. Mech. Mater., vol. 20, no. 2, 1995, pp. 125–152.
69. Schweizerhof, K., et al.: Crashworthiness Analysis With Enhanced Composite Material Models in LS–DYNA—Merits and Limits. 5th International LS–DYNA Users Conference, 1998. http://www.dynasupport.com/howtos/material/composite-models Accessed May 29, 2013.
70. Goldberg, Robert K.: Implementation of Fiber Substructuring Into Strain Rate Dependent Micromechanics Analysis of Polymer Matrix Composites. NASA/TM—2001-210822, 2001. http://ntrs.nasa.gov/
71. Robertson, D.D.; and Mall, S.: Micromechanical Relations for Fiber-Reinforced Composites Using the Free Transverse Shear Approach. J. Compos. Technol. Res., vol. 15, no. 3, 1993, pp. 181–192.
72. Hashin, Z.: Failure Criteria for Unidirectional Fiber Composites. J. Appl. Mech. Trans. ASME, vol. 47, no. 2, 1980, pp. 329–334.
73. Zheng, Xiahua: Nonlinear Strain Rate Dependent Composite Model for Explicit Finite Element Analysis. Ph.D. Dissertation, University of Akron, 2006.
74. Wilbeck, J.S.: Impact Behavior of Low Strength Projectiles. Ph.D. Dissertation, Texas A&M University, 1977.
75. ASTM Standard D2234: Standard Test Method for Short-Beam Strength of Polymer Matrix Composite Materials and Their Laminates. ASTM International, West Conshohocken, PA, 2006. www.astm.org. Accessed Nov. 14, 2008.
76. Tabiei, A.: LS–DYNA Composite Materials Training Course. NASA Langley Research Center, 2007.

REPORT DOCUMENTATION PAGE	Form Approved OMB No. 0704-0188

The public reporting burden for this collection of information is estimated to average 1 hour per response, including the time for reviewing instructions, searching existing data sources, gathering and maintaining the data needed, and completing and reviewing the collection of information. Send comments regarding this burden estimate or any other aspect of this collection of information, including suggestions for reducing this burden, to Department of Defense, Washington Headquarters Services, Directorate for Information Operations and Reports (0704-0188), 1215 Jefferson Davis Highway, Suite 1204, Arlington, VA 22202-4302. Respondents should be aware that notwithstanding any other provision of law, no person shall be subject to any penalty for failing to comply with a collection of information if it does not display a currently valid OMB control number.
PLEASE DO NOT RETURN YOUR FORM TO THE ABOVE ADDRESS.

1. REPORT DATE *(DD-MM-YYYY)*	2. REPORT TYPE	3. DATES COVERED *(From - To)*
01-12-2013	Final Contractor Report	

4. TITLE AND SUBTITLE
Experimental and Analytical Characterization of the Macromechanical Response for Triaxial Braided Composite Materials

5a. CONTRACT NUMBER

5b. GRANT NUMBER
NNX07AK57H

5c. PROGRAM ELEMENT NUMBER

6. AUTHOR(S)
Littell, Justin, D.

5d. PROJECT NUMBER

5e. TASK NUMBER

5f. WORK UNIT NUMBER
WBS 698259.02.07.03.04.01

7. PERFORMING ORGANIZATION NAME(S) AND ADDRESS(ES)
University of Akron
302 E. Buchtel Avenue
Akron, Ohio 44304

8. PERFORMING ORGANIZATION REPORT NUMBER
E-16653

9. SPONSORING/MONITORING AGENCY NAME(S) AND ADDRESS(ES)
National Aeronautics and Space Administration
Washington, DC 20546-0001

10. SPONSORING/MONITOR'S ACRONYM(S)
NASA

11. SPONSORING/MONITORING REPORT NUMBER
NASA/CR-2013-215450

12. DISTRIBUTION/AVAILABILITY STATEMENT
Unclassified-Unlimited
Subject Categories: 39 and 24
Available electronically at http://www.sti.nasa.gov
This publication is available from the NASA Center for AeroSpace Information, 443-757-5802

13. SUPPLEMENTARY NOTES
The author is currently affiliated with National Aeronautics and Space Administration, Langley Research Center, Mail Stop 495, Hampton, Virginia 23681-2199.

14. ABSTRACT
New aircraft engines are being developed that use fan cases made of composite materials instead of metallic materials. Triaxially braided composites are one system under investigation as a possible replacement candidate; however, the impact properties for these materials have not been fully determined, and computationally efficient computer models are not available. The research reported herein attempts to bridge these deficiencies by addressing the mechanical response of triaxial braided composite materials and their constituents. First, new test methods are presented for the polymer resin constituent of the composite, accurately quantifying the resin under a variety of strain rates and temperature for three loading conditions. The tests use novel specimen designs along with a noncontact measuring system capable of identifying and quantifying many of the microscale failure mechanisms present in the materials. These methods are then extended to the composite material test specimens. The results for the composites reveal noticeable differences in strength, failure strain, and stiffness for the different material systems presented. Investigations into the microscale failure mechanisms provide information about the nature of the different material system behaviors. Finally, using the data gathered, a hybrid micro-macromechanical computer model is created to simulate the behavior of these composite material systems under static and ballistic impact loading using the test data acquired. The model predicts composite static strength and stiffness to within 10 percent of the gathered test data and also agrees with composite impact data.

15. SUBJECT TERMS
Photographic measurement; Composite materials; Static tests; Computer simulations

16. SECURITY CLASSIFICATION OF:			17. LIMITATION OF ABSTRACT	18. NUMBER OF PAGES	19a. NAME OF RESPONSIBLE PERSON
a. REPORT	b. ABSTRACT	c. THIS PAGE			STI Help Desk (email:help@sti.nasa.gov)
U	U	U	UU	114	19b. TELEPHONE NUMBER *(include area code)* 443-757-5802